

Fate and Transport of Antibiotics in the Soil-Plant System

Rachel Johnson

MSc (by Research)

University of York

Chemistry

December 2019

Abstract

Antibiotics can enter the environment through the application of biosolids and the use of treated wastewater effluent for irrigation. In the agro-environment, low levels of antibiotics may contribute to an increased risk of selection for antimicrobial resistance in the soil, as well as alter overall microbial biomass and the relative abundance of different microbial groups. Alterations of the soil microbiome is likely to impact plant health as a result of the symbiotic relationship between plants and soil microbes. Furthermore, as a result of common evolutionary ancestry, many of the same receptors and processes that antibiotics target in microbes are conserved in plants. As a result, a direct phytotoxic effect from antibiotic exposure is possible. The aim of the study is to evaluate fate and transport of antibiotics in the soil-plant system.

An environmentally relevant mixture of antibiotic compounds was derived. A synthetic wastewater effluent combined with the antibiotic mixture was used for irrigation in a 14-week mesocosm study with barley (*Hordeum vulgare*) as the model crop. The transport of antibiotics in the soil plant system was monitored *via* targeted analytical measurement of antibiotic concentrations in soil pore water and mesocosm leachate using HPLC-QqQ-MS. Findings show that some of the antibiotics (i.e. tetracycline, oxytetracycline, ciprofloxacin, amoxicillin and penicillin v) are undetectable in both the soil pore water and the leachate. Risk quotients were derived for each antibiotic from the measured concentrations using recently published predicted no effect concentrations (PNECs) for the selection of antimicrobial resistance. Metronidazole was the only antibiotic found to exceed the PNEC at environmental concentrations, suggesting that it could be posing a risk of inducing antimicrobial resistance in the agricultural environment.

Laboratory degradation experiments were used to determine antibiotic stability, with possible degradants being identified using non-targeted high mass accuracy mass spectrometry. It was discovered that oxytetracycline, metronidazole and amoxicillin do not degrade *via* hydrolysis but did *via* photolysis. Further experiments investigated the photolytic degradation products using novel gas-phase UV spectroscopic techniques, with the aim of being used in future work to identify stable degradation products in the soil pore water and leachate. Results from this work seek to provide new insights into the fate and transport of human use antibiotics in the agricultural environment.

Table of Contents

Abstract	2
Table of Contents	3
List of Figures	10
List of Tables	15
Acknowledgements	17
Declaration	18
Chapter 1 Introduction	19
1.1 <i>Aims and Objectives</i>	21
1.2 <i>Mesocosms</i>	21
1.3 <i>Pathways of Antibiotic Entry into the Environment</i>	22
1.4 <i>Instrumentation</i>	24
1.4.1 <i>Techniques Currently Used</i>	24
1.4.2 <i>Liquid Chromatography (LC)</i>	24
1.4.3 <i>Mass Spectrometry</i>	27
1.4.3.1 <i>Electrospray Ionisation (ESI)</i>	27
1.4.3.1.1 <i>Mechanisms for the formation of gas phase ions</i>	29
1.4.3.1.2 <i>Droplet Desolvation</i>	29
1.4.3.2 <i>Tandem Mass Spectrometry</i>	30
1.4.3.2.1 <i>Quadrupoles</i>	31
1.4.3.2.1.1 <i>Description</i>	31

1.4.3.2.1.2	<i>Voltages Applied to Quadrupole Rods</i>	32
1.4.3.2.1.3	<i>Changing charge</i>	34
1.4.3.2.1.4	<i>Movement of ions through the quadrupole</i>	34
1.4.3.2.1.5	<i>Simple Stability Diagram</i>	36
1.4.3.2.1.6	<i>Generalised Stability Diagram</i>	38
1.4.3.2.1.7	<i>The quadrupole as a mass filter</i>	39
1.4.3.2.1.8	<i>Scanning a mass spectrum</i>	40
1.4.3.2.2	<i>Summary of Tandem Mass Spectrometry</i>	40
1.4.3.3	<i>Fourier-Transform Ion Cyclotron Resonance (FT-ICR)</i>	41
1.4.3.3.1	<i>The Penning trap</i>	41
1.4.3.3.2	<i>Excitation of Ions</i>	42
1.4.3.3.3	<i>Detection of Ions</i>	43
1.4.3.3.3.1	<i>Broadband Image Current Detection</i>	43
1.4.3.3.4	<i>Fourier transformation</i>	44
1.4.3.3.5	<i>Summary of FT-ICR</i>	44
1.4.3.4	<i>Orbitrap Mass Analyser</i>	45
1.4.3.4.1	<i>Summary of the Orbitrap Mass Analyser</i>	46
1.4.3.5	<i>Laser Interfaced Mass Spectrometer (LIMS) Ion Trap</i>	47
1.4.3.5.1	<i>Summary of the LIMS</i>	47

Chapter 2 Development of an LC-MRM Method for Detection and Quantification of Antibiotics in Soil Pore Water and Leachate Samples 48

2.1	<i>Introduction</i>	48
-----	---------------------	----

2.2	<i>Materials</i>	48
2.3	<i>Method Development</i>	49
2.3.1	<i>Definition of a Robust Method</i>	49
2.3.1.1	<i>Peak Shape</i>	50
2.3.2	<i>Determining SRM transitions for the 11 Antibiotic Analytes</i>	51
2.3.3	<i>Solvent Selection</i>	53
2.3.3.1	<i>Assessment of 100% Methanol and 0.1% Formic Acid as the Mobile Phases</i>	53
2.3.3.2	<i>Assessment of Acetonitrile and 0.1% Formic Acid as the Mobile Phases</i>	53
2.3.3.3	<i>Preparation of a Calibration Curve</i>	53
2.3.3.4	<i>Assessment of Calibration Signals</i>	54
2.3.3.5	<i>Assessment of Acetonitrile and 25 mM Ammonium Acetate as the Mobile Phases</i>	56
2.3.4	<i>Influence of Column Chemistry</i>	59
2.3.5	<i>Colistin b: Problems and Solution</i>	60
2.4	<i>Method Validation and Limits of Detection</i>	61
2.4.1	<i>Linearity</i>	61
2.4.2	<i>Limits of Detection</i>	61
2.4.3	<i>Accuracy</i>	63
2.4.4	<i>Precision</i>	64
2.5	<i>Summary</i>	65
Chapter 3 Targeted Analysis of Soil-Derived Samples		67
3.1	<i>Introduction</i>	67
3.1.1	<i>Pore Water and Leachate</i>	67

3.2	<i>Method</i>	68
3.2.1	<i>Background</i>	68
3.2.2	<i>Effect of pH</i>	77
3.2.3	<i>HPLC MS/MS analysis</i>	78
3.2.3.1	<i>Preparations of stock solutions</i>	78
3.2.3.2	<i>Internal Standards</i>	79
3.2.4	<i>Leachate Collection and Preparation</i>	79
3.2.5	<i>Pore Water Extractions</i>	80
3.2.6	<i>Analysis of Leachate and Pore Water Samples</i>	80
3.3	<i>Results</i>	81
3.3.1	<i>Leachate</i>	81
3.3.2	<i>Pore Water</i>	84
3.3.3	<i>Comparing concentrations detected to PNEC values</i>	86
3.4	<i>Effect on Plants: Root Density</i>	88
3.4.1	<i>Methods</i>	88
3.4.2	<i>Results</i>	89
3.5	<i>Discussion</i>	90
3.5.1	<i>Comparing Antibiotics in Pore Water and Leachate Samples</i>	90
3.5.1.1	<i>Leachate</i>	90
3.5.1.2	<i>Pore Water</i>	92
3.5.1.3	<i>Comparing concentrations detected in pore water and leachate to PNEC values</i>	93
3.5.2	<i>Partitioning of Antibiotics in the Soil System</i>	94

3.5.3	<i>Effect on Plants</i>	96
3.6	<i>Conclusion</i>	96
Chapter 4 Transformation of Antibiotics via Hydrolysis and Photolysis		97
4.1	<i>Introduction</i>	97
4.1.1	<i>Degradation by UV Photolysis</i>	98
4.1.2	<i>Degradation by Hydrolysis</i>	100
4.1.3	<i>Aims</i>	100
4.2	<i>Method</i>	101
4.2.1	<i>Hydrolysis in the light</i>	101
4.2.2	<i>Hydrolysis in the dark</i>	101
4.2.3	<i>Gas-Phase Photodegradation</i>	102
4.2.4	<i>Energy Dependent Fragmentation Maps</i>	103
4.3	<i>Results and Discussion</i>	103
4.3.1	<i>Hydrolysis with photolysis</i>	104
4.3.1.1	<i>Metronidazole</i>	104
4.3.1.2	<i>Oxytetracycline</i>	108
4.3.1.3	<i>Penicillin v</i>	111
4.3.2	<i>Hydrolysis in the dark (no photolysis)</i>	114
4.3.2.1	<i>Metronidazole</i>	114
4.3.2.2	<i>Oxytetracycline</i>	116
4.3.2.3	<i>Penicillin v</i>	119
4.3.3	<i>Gas phase photodegradation</i>	120

4.3.3.1	<i>Metronidazole</i>	121
4.3.3.2	<i>Penicillin v</i>	124
4.3.3.3	<i>Oxytetracycline</i>	127
4.3.4	<i>Energy Dependent Maps</i>	130
4.3.4.1	<i>Metronidazole</i>	130
4.3.4.2	<i>Penicillin v</i>	131
4.3.4.3	<i>Oxytetracycline</i>	132
4.3.5	<i>Possible Degradation Pathways</i>	133
4.3.5.1	<i>Metronidazole</i>	134
4.3.5.2	<i>Penicillin v</i>	135
4.3.5.3	<i>Oxytetracycline</i>	136
4.4	<i>Conclusions</i>	137
Chapter 5 Conclusions and Further Work		138
5.1	<i>Conclusions</i>	138
5.1.1	<i>Identify methods already used to detect antibiotics and to assess them regarding the 11 antibiotics targeted here (Chapter 2).</i>	138
5.1.2	<i>Develop and validate a LC-MS/MS method to detect and quantify the 11 antibiotics in two soil-derived samples: soil pore water and irrigation leachate (Chapter 2).</i>	138
5.1.3	<i>Measure the levels of antibiotics in the pore water and soil leachates of barley rhizospheres, grown in a mesocosm, following irrigation with spiked wastewater (Chapter 3).</i>	139

5.1.4	<i>Based on the results of objective 3, compounds susceptible to environmental degradation were examined further, using hydrolysis and photolysis experiments to identify degradants, with the use of non-targeted mass spectrometric analysis (Chapter 4).</i>	140
5.2	<i>Future Work</i>	141
5.2.1	<i>Analysis and Quantification of the Soil Samples</i>	141
5.2.2	<i>Identification of Antimicrobial Degradants Using a Non-Targeted and Candidate Degradant Screening Approach</i>	141
5.2.3	<i>Long Term Fate studies</i>	141
	Appendix	142
	References	150

List of Figures

Figure 1.1: pathways of antibiotics into the environment. WWTP = wastewater treatment plant. The red arrow represents the pathway this project is focusing on.	22
Figure 1.2: process of ESI prior to entering the mass spectrometer – 1) charged residue model, 2) ion evaporation model.	28
Figure 1.3: SRM showing the selection of one ion, the breakdown of that ion, the selection of one product ion and the signal obtained via the detector, where the MS is coupled to an LC.	31
Figure 1.4: four charged rods making up the quadrupole, showing the different axes. The z axis is along the axis of the rods. The negative rods are found in the yz plane, and the positive rods are found in the xz plane.	31
Figure 1.5: combining AC and DC voltages applied to quadrupole rod pairs. Top: positive rods; bottom: negative rods.	33
Figure 1.6: the voltage of each pair of rods shown against time.	34
Figure 1.7: pathway taken by ions travelling through the quadrupole. The red arrow at c represents the light ions being lost, and the red arrow at d represents the heavy ions being lost.	35
Figure 1.8: simple stability diagram. At point A, (DC voltage only) the ions are stable on the x axis (repelled by the positive rods) but unstable on the y axis (lost to the negative rods). At point B, the RF voltage is not large enough to offset the DC voltage, and so the ion is again lost to the negative rods. At point C, the ion is stable. At point D, the RF voltage is destabilising, causing the ion to be lost on the x axis.	37
Figure 1.9: generalised stability diagram with dimensionless α and q	39
Figure 1.10: FT-ICR instrument set-up, showing the trapping plates (left), excitation plates (middle) and the detector plates (right). The red arrow shows the magnetic field applied to the Penning Trap.	41

Figure 1.11: orbitrap mass analyser simplified diagram. Red arrow indicates where the ions enter the orbitrap. The blue arrows represent the orbiting motion around the central electrode, and the green arrow represents the oscillations along the central electrode.	45
Figure 2.1: a demonstrative tailing peak, labelled with measurements needed to calculate the tailing factor (Equation 2.1).	50
Figure 2.2: chromatogram of cefalexin, with a mobile phase consisting of acetonitrile and 0.1% aqueous formic acid.	55
Figure 2.3: chromatogram of cefalexin, with mobile phases consisting of acetonitrile and 25 mM ammonium acetate. Top: 1 ng/L, middle: 100 ng/L, bottom: 10,000 ng/L.	57
Figure 2.4: peaks from the LC-MS/MS chromatograms of amoxicillin (left), cefalexin (middle) and penicillin v (right), showing the increase in intensity as the concentration increases. Mobile phases: acetonitrile and 25 mM ammonium acetate.	58
Figure 2.5: MALDI spectrum of colistin b, dissolved in methanol (concentration ~11 mg/L) and using 2,5-dihydroxybenzoic acid as the matrix.	60
Figure 3.1: schematic of plant pot showing the pore water (labelled) and the leachate (labelled).	67
Figure 3.2: calibration standards (and blank) in red boxes. Arrows represent movement of solution from one vial to another, with the quantity to be transferred reported next to them. All light blue boxes were made up to 5 mL of 50: 50 (v:v) organic solvent: HPLC grade water.	78
Figure 3.3: summary of antibiotic concentrations found in the leachate samples. Amoxicillin, penicillin v, tetracycline, oxytetracycline and ciprofloxacin were not detected.	81
Figure 3.4: overview of antibiotic concentrations found in the pore water samples. Tetracycline, oxytetracycline, penicillin v, cefalexin, clarithromycin, amoxicillin and ciprofloxacin were not detected.	84
Figure 3.5: Root density in barley mesocosms from treatments A (control), B (PEC×0.1), C (PEC), D (PEC×10), E (PEC×100). Bars represent standard error.	89

Figure 3.6: scattergraph demonstrating lack of correlation between log P and the average measured concentration detected in the leachate samples collected after 28 irrigations.....	91
Figure 4.1: Conventional molecular orbital energy diagram. Dotted arrows represent the energy transitions electrons do when excited with wavelengths of 200-400 nm.....	98
Figure 4.2: hydrolysis of the β -lactam ring in penicillin v	100
Figure 4.3: Combined peak intensity for m/z 172, 194, 210, 343, 365 and 381 of metronidazole on time course exposure to UV light (wavelength 365 nm).....	104
Figure 4.4: Peak intensity for potential degradants of metronidazole after a time course exposure to UV light (wavelength 365 nm).	105
Figure 4.5: Peak intensity for m/z 172, 210 and 343 of metronidazole after a time course exposure to UV light (wavelength 365 nm). Peak intensities of m/z values experiencing ion suppression have been removed. The red line represents the moving average. Outliers shown in orange.....	107
Figure 4.6: Peak intensity for m/z 461, 483, 499 and 943 of oxytetracycline on time course exposure to UV light (wavelength 365 nm).....	108
Figure 4.7: Peak intensity for potential degradants of oxytetracycline on time course exposure to UV light (wavelength 365 nm).....	109
Figure 4.8: Peak intensity for m/z 374, 389, 723 and 739 of penicillin v on time course exposure to UV light (wavelength 365 nm).....	111
Figure 4.9: Peak intensity for suspected degradants of penicillin v after a time course exposure to UV light (wavelength 365 nm).....	112
Figure 4.10: Peak intensity for m/z 389 and 739 of penicillin v on time course exposure to UV light (wavelength 365 nm). The ions experiencing ion suppression have been excluded from the peak intensity total.	113

Figure 4.11: combined peak intensities of m/z 172 and 210 mapped over a period of 72 hours (4320 minutes). Peak intensities of m/z values experiencing ion suppression have been removed. Outliers shown in orange.	114
Figure 4.12: production of potential hydrolytic degradants of metronidazole with m/z 178, 196 and 249 over a period of 72 hours (4320 minutes).	115
Figure 4.13: combined peak intensities of m/z 461, 483, 499 and 943 mapped over a period of 72 hours (4320 minutes). Outliers shown in orange.....	116
Figure 4.14: production of hydrolytic degradants of oxytetracycline over a period of 72 hours (4320 minutes).....	117
Figure 4.15: UV spectra of oxytetracycline in aqueous solution while kept in the dark. Two spectra are overlaid: T ₀ and T _{6 hours}	118
Figure 4.16: combined peak intensities of m/z 389 and 739 mapped over a period of 72 hours (4320 minutes).....	119
Figure 4.17: UV wavelengths, showing UVA, UVB and UVC in both wavelengths (top x axis) and photon energy (bottom x axis).....	120
Figure 4.18: Structure of metronidazole	121
Figure 4.19: Solution-phase absorption spectra for metronidazole under (a) neutral conditions and (b) protonated conditions. The solid lines are five-point adjacent averages of the data points.	122
Figure 4.20: Structure of penicillin v	124
Figure 4.21: Solution-phase absorption spectra for penicillin v under (a) neutral conditions and (b) protonated conditions. The solid lines are five-point adjacent averages of the data points.....	125
Figure 4.22: Structure of oxytetracycline	127
Figure 4.23: Solution-phase absorption spectra for oxytetracycline under (a) neutral conditions and (b) protonated conditions. The solid lines are five-point adjacent averages of the data points.	128

Figure 4.24: Parent ion dissociation curve of metronidazole [M+H] ⁺ (m/z 172), along with production curves for the primary and secondary fragments formed upon HCD between 0–50% energy.....	130
Figure 4.25: Parent ion dissociation curve of penicillin v [M+H] ⁺ (m/z 351), along with production curves for the primary and secondary fragments formed upon HCD between 0–90% energy setting.....	131
Figure 4.26: Parent ion dissociation curve of oxytetracycline [M+H] ⁺ (m/z 461), along with production curves for the primary, secondary and tertiary fragments formed upon HCD between 0–70% energy setting.....	132
Figure 4.27: Structure of metronidazole. Red lines show suggested primary methods of fragmentation.	134
Figure 4.28: Structure of penicillin v. Red line shows the primary route of fragmentation.....	135
Figure 4.29: structure of oxytetracycline. Red lines show suggested primary routes of fragmentation.	136

List of Tables

Table 1.1: percentages of unchanged excreted antibiotics from the literature.....	23
Table 2.1: Instrument optimisation results for antibiotics dissolved in acetonitrile and water.	52
Table 2.2: limit of detections for the two LC-MS methods, compared to the PNEC for each antibiotic.....	62
Table 2.3: percentage recoveries of samples injected on the LC-MS.....	64
Table 2.4: an overview of the method used for each antibiotic	65
Table 2.5: LC method parameters.....	66
Table 2.6: LC mobile phase gradient	66
Table 3.1: concentrations of 11 antibiotics used to irrigate the barley mesocosms	70
Table 3.2: time of sample collections, showing details of plant treatments.....	71
Table 3.3: chemical properties of each antibiotic	72
Table 3.4: list of pKa values for antibiotics	77
Table 3.5: comparing averaged pore water concentrations to the PNEC values.	86
Table 3.6: comparing averaged leachate concentrations to the PNEC values.	87
Table 3.7: percentage of antibiotics found in the pore water and leachate samples.....	95
Table 4.1: Parameters used for gas-phase photolysis scans on metronidazole, oxytetracycline and penicillin v.....	102
Table 4.2: the ratio of the peak intensities for the ions of metronidazole from two solutions with different concentrations (50 mg/L and 10 mg/L).....	107
Table 4.3: the ratio of the peak intensities for the ions of oxytetracycline from two solutions with different concentrations (50 mg/L and 10 mg/L).....	110
Table 4.4: the ratio of the peak intensities for the ions of penicillin v from two solutions with different concentrations (50 mg/L and 10 mg/L).....	113

Table 4.5: Photon energy absorbances found in the photodepletion and the photofragmentation spectra of metronidazole identified in the gas phase. w = weak, m = medium, s = strong, vs = very strong (relative to each other)	123
Table 4.6: Photon energy absorbances found in the photodepletion and the photofragmentation spectra of penicillin v identified in the gas phase. vw = very weak, w = weak, s = strong, vs = very strong (relative to each other)	126
Table 4.7: Photon energy absorbances found in the photodepletion and the photofragmentation spectra of oxytetracycline identified in the gas phase. w = weak, m = medium, s = strong, vs = very strong, vvs = very very strong (relative to each other).....	129
Table 5.1: summary of the findings from the photolysis and hydrolysis experiments for each antibiotic studied.	140

Acknowledgements

Firstly, I would like to thank my family and friends for all their support throughout the past year.

Secondly, I would like to extend my thanks to Dr Caroline Dessent for the help with the gas phase photolysis work, and for the use of her lab equipment. I would especially like to thank Natalie Wong for all the help she gave me, from experimental work in the lab to data analysis, interpretation and writing up of the results. In addition, I would like to thank Adam Little for his assistance with writing programs that saved me days of data analysis!

Thirdly, to the Department of Chemistry, for their support throughout my time here at University, both in my undergraduate and graduate work, particularly those in the Graduate Office: Rachel Crooks, Alice Duckett and Sharon Stewart. I would like to thank the members of the JTO group for providing help, support, friendship and much laughter: Karl, Bella, Alex, Hannah, John, Lea, Bruna, Jen, Ben, Martha, Simeon, Mark, Angelo and Alice. I would especially like to thank Ed Bergström for all the help he gave with managing, operating and maintaining the instruments in the Centre of Excellence for Mass Spectrometry.

Last but certainly not least, I thank my supervisors, Professor Jane Thomas-Oates and Dr Brett Sallach. Their assistance, guidance and support was invaluable throughout this project, and I am so grateful to the both of them for everything they have done.

Declaration

I declare that this thesis is a presentation of original work and I am the sole author. This work has not previously been presented for an award at this, or any other, University. All sources are acknowledged as References.

Rachel Johnson

Chapter 1 Introduction

For nearly a century, antibiotics have provided substantial benefits to human health. As a result, their use has continually increased and is forecast to continue increasing in the coming decades.¹

Once ingested, the body metabolises a small portion of the compound and the rest of the antibiotic and any metabolites are eliminated in human waste, whereby antibiotics enter the sewage system where they are inefficiently removed by conventional wastewater treatment technologies.^{2,3} Depending upon physicochemical properties, compounds will partition either in the solid or liquid waste streams where they will leave the treatment works either in wastewater effluent or in biosolids (sludge).⁴ The use of biosolids as soil amendments to condition soil and provide nutrients as well as the use of treated wastewater for irrigation in water stressed regions of the world represent two major pathways antibiotics can enter the natural or agricultural environment.⁵⁻⁷ In the past two decades, there has been growing recognition that antibiotics in the environment may pose a serious threat to human health.⁸ This threat is based on knowledge that exposure to sub-inhibitory levels of antibiotics can promote antibiotic resistance in microbial organisms. Increased resistance can cause bacterial infections that are unable to be treated with antibiotics.⁵

Proliferation of antibiotic resistance is not the only way that antibiotics in the environment can threaten human health. Plants and bacteria have a symbiotic relationship⁹, in which the bacteria help facilitate nutrient acquisition by the plant, and in return, plants release exudates that are used by microbes for energy and biomass production. This interaction primarily occurs in the rhizosphere, which can be defined as a narrow region of soil surrounding the roots of the plant.¹⁰ This zone can be influenced by the plant in ways that affect the soil's chemical composition.¹⁰ The rhizosphere is relatively rich in nutrients compared to the surrounding soil, and contains a large range of bacteria, including plant growth promoting rhizobacteria.¹⁰ Once antibiotics enter

this system, they have the potential to greatly disturb the microbial processes that occur naturally, so affecting food crop production.⁶

In addition to disrupting plant-microbe interactions, antibiotics may also result in direct toxicity to plants. Research by Pollock et al suggests that the β -lactam antibiotics are the least toxic to plants.¹¹ Other research suggests that antibiotics have an impact on the growth of plant crops, such as lettuce^{12,13}, as well as impacting aquatic plants.¹⁴

The purpose of the work described in this thesis is to therefore understand how mixtures of antibiotics in wastewater treatment effluent impact soil health and plant productivity, in addition to analysing the impact of the antibiotics on plant growth directly, using spring barley (*Hordeum vulgare*) as the model crop.

1.1 Aims and Objectives

Measuring antibiotics in environmental matrices remains a significant challenge.¹⁵ Therefore, the main aim of the project was to develop an appropriate LC-MS/MS method to detect 11 different target antibiotics (listed in **Table 1.1**), and to determine exactly how the environmental levels of antibiotics in water affect the growth of plants, testing the hypothesis that *“Increased concentrations of antibiotics in the environment have a negative impact on the growth of plants”*.

Several objectives were used to address these aims:

1. Identify methods already used to detect antibiotics and to assess them regarding the 11 antibiotics targeted here (Chapter 2).
2. Develop and validate a LC-MS/MS method to detect and quantify the 11 antibiotics in two soil-derived samples: soil pore water and irrigation leachate (Chapter 3).
3. Measure the levels of antibiotics in pore water and soil leachate of barley rhizospheres, grown in a mesocosm, following irrigation with spiked wastewater (Chapter 3).
4. Based on the results of objective 3, further study of compounds susceptible to environmental degradation, using hydrolysis and photolysis experiments to identify degradants, with the use of non-targeted mass spectrometric analysis (Chapter 4).

1.2 Mesocosms

A mesocosm is an artificially constructed simple model ecosystem used for experimental studies of natural ecosystems.¹⁶ The main advantage of using a mesocosm is having reliable reference conditions, such as controlling environmental parameters, allowing for easy replication of the study.¹⁶

1.3 Pathways of Antibiotic Entry into the Environment

There are many pathways through which antibiotics can enter the environment (**Figure 1.1**).^{5,6}

One such pathway into the environment is *via* human excretion. A large percentage of the antibiotic is excreted, unchanged, in urine and faeces (**Table 1.1**).^{5,17-19} These antibiotics then enter the sewage works where they are often poorly removed by conventional wastewater treatment technologies which have traditionally been designed to control the release of nutrients and human pathogens from the waste stream.²⁰ From here they are released as treated wastewater effluent into receiving waters.²⁰

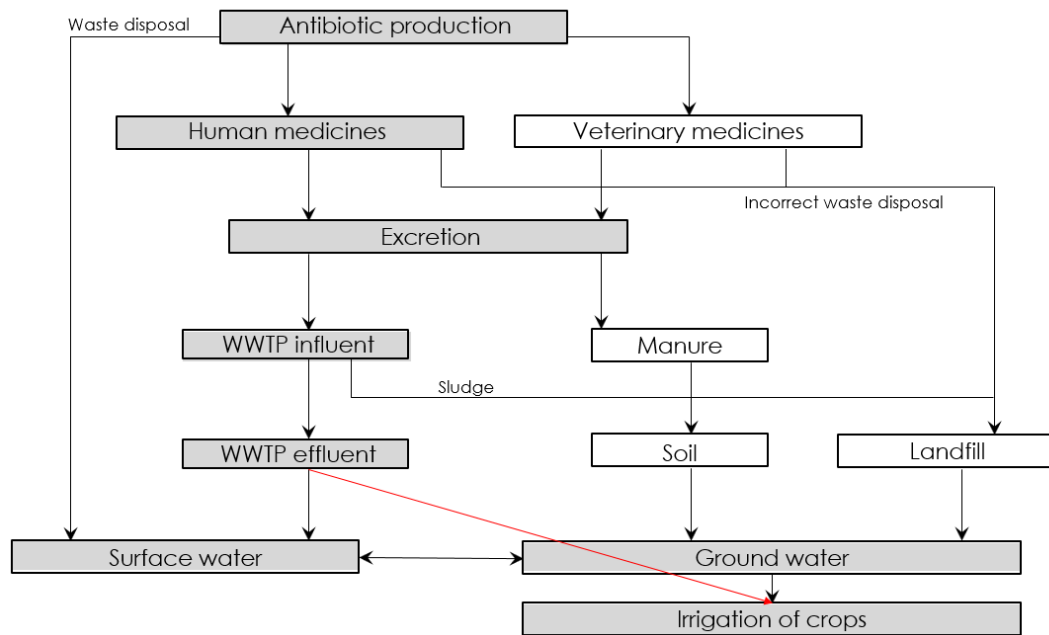


Figure 1.1: pathways of antibiotics into the environment. WWTP = wastewater treatment plant.

The red arrow represents the pathway this project is focusing on.

Table 1.1: percentages of unchanged excreted antibiotics from the literature.

Antibiotics	Excretion of unchanged compound in the urine %
Amoxicillin	80-90 ⁵
Penicillin v	~40 ⁵
Colistin b	~60 ²¹
Cefalexin	~85 ¹⁹
Tetracycline	80-90 ⁵
Oxytetracycline	>80 ⁵
Metronidazole	60-80 ¹⁷
Clarithromycin	>60 ⁵
Erythromycin	>60 ⁵
Trimethoprim	~60 ⁵
Ciprofloxacin	~40-50 ¹⁸

Many human antibiotics are also used for veterinary purposes, and as such, one significant exposure route is through the administration of veterinary antibiotics to livestock to treat disease, or in some cases for growth promotion or prophylaxis. Antibiotics that are not metabolised are excreted through urine and faeces either directly to agricultural soils, *via* pasturing of livestock, or applied as a slurried manure for fertilisation.⁵ When antibiotics enter the soil environment they partition between soil constituents (clays, silicas and organic matter) and the soil pore water. The partitioning is caused by the soil adsorption coefficient (K_d) and the octanol-water partition coefficient (K_{ow}). Antibiotics with a high K_{ow} would not be expected to be present in the pore water, as they are more likely to have sorbed to the soil. Compounds with a high K_{ow} also are expected to have a high K_d values.²² The portion of compounds in the soil pore water remains bioavailable where it can then be taken up by plants.²³ The most mobile

antibiotics are capable of moving through the soil subsurface with the potential to enter the surface and ground water.²⁴

1.4 Instrumentation

This next section covers the instrumentation used for the analysis of the antibiotics in this project.

1.4.1 Techniques Currently Used

Currently, the primary technique used to analyse antibiotics in environmental matrices is targeted HPLC-ESI-MS/MS.^{5,25-28} This is because LC-MS/MS has very good selectivity with favourable limits of detection (LODs - detection limits as low as ng/L), which is useful for selecting and quantifying compounds present in complex environmental mixtures.

1.4.2 Liquid Chromatography (LC)

Liquid chromatography is an important separation technique, particularly with complex environmental mixtures, such as soil pore water or leachate (see section 3.1.1). Before entering the mass spectrometer, the analytes must be ionised which happens in the ionisation source.²⁹⁻³¹ With no separation technique, the analytes are all ionised at the same time, resulting in competition for the available charge. This may result in many analytes not being ionised. To reduce this competition, a separation technique is needed: in this project HPLC (discussed later in this section) was used. LC can separate the compounds based on different physicochemical factors.

LC involves passing a solvent (the mobile phase) through a column packed with particles (the stationary phase). The sample is introduced to the mobile phase prior to entering the column, and as the mobile phase flows through the column the different compounds interact with the particles in the stationary phase. The higher the affinity for the mobile

phase, the less the compound interacts with the stationary phase and the more rapidly it elutes from the column.

The stationary phase can be made from different materials, and the type and particle size of stationary phase material used greatly affects the efficiency of the separation of the components. Efficiency (also known as “plate count”) is a measure of the dispersion of a peak and can be calculated using **Equation 1.1**.³²

Equation 1.1

$$N = 16 \left(\frac{t}{w} \right)^2$$

where t_R = retention time, and w = peak width at the base. The higher the value of N , the more efficient the column is.

The materials used for the stationary phase can have different particle sizes. The smaller the particle size, the greater the efficiency of the column, but the greater the pressure needed to pump the mobile phase through the column. High performance liquid chromatography (sometimes referred to as high pressure liquid chromatography - HPLC) can address this situation, as this reaches greater system pressures than LC.³³ The efficiency can be improved yet again by using UPLC (or UHPLC – ultra(high)-performance liquid chromatography) as even higher pressures are reached³⁴, but as UPLC was unavailable for this project, HPLC was used.

Using a non-polar mobile phase and a polar stationary phase is referred to as normal phase LC. The alternative is called reversed phase, and this is more commonly used. Reversed phase LC uses a polar (aqueous-organic) solvent carrying the analytes over a non-polar (e.g. chemically modified silica with C18 chains attached) stationary phase. The polar compounds elute first, with the non-polar compounds eluting later. In this project the compounds were separated according to their polarity, using reversed phase separations.

To improve the separation efficiency, a mobile phase gradient is often used, in which the ratio of aqueous to organic solvent is altered over time (starting with low organic and ending with high for reversed-phase stationary phases). Incorporating the gradient allows for better peak shapes, with a reduced risk of tailing. Prior to any analysis of the samples, the process is optimised to ensure that the retention times for the compounds were significantly different, with the aim of reducing competition for the charge.

1.4.3 Mass Spectrometry

Mass spectrometry is a powerful tool used to analyse a great variety of compounds, by ionising the compounds and then sorting the ions (either positively charged or negatively charged ions) according to their mass-to-charge (m/z) ratio.^{35,36} It is the key method of detecting the antibiotics used in this project. The main components of the mass spectrometer are the sample inlet, the ionisation source, the mass analyser and the detector.

There were four mass spectrometers used in this project: triple quadrupole (section 1.4.3.2), Fourier-transform ion cyclotron resonance (section 1.4.3.3), orbitrap (section 1.4.3.4) and a laser-interfaced ion trap (section 1.4.3.5).

1.4.3.1 Electrospray Ionisation (ESI)

Once the analytes have eluted from the column, they enter the ionisation source (ESI).³⁶⁻³⁸ ESI is defined as the transfer and ionisation of molecules from solution to the gas phase by electrospray. It is a soft atmospheric pressure ionisation (API) technique, producing intact ions related to the analyte molecule and inducing little to no fragmentation. With ESI, a large variety of chemical substances can be ionised, including large non-covalent protein complexes due its ability to introduce multiple charges (z). A useful and unique feature of ESI is that it can produce multiply charged compounds. Despite much being known about ESI, the mechanism by which gaseous ions are formed is still debated, proposed to proceed by pathways **1** or **2** in **Figure 1.2**.

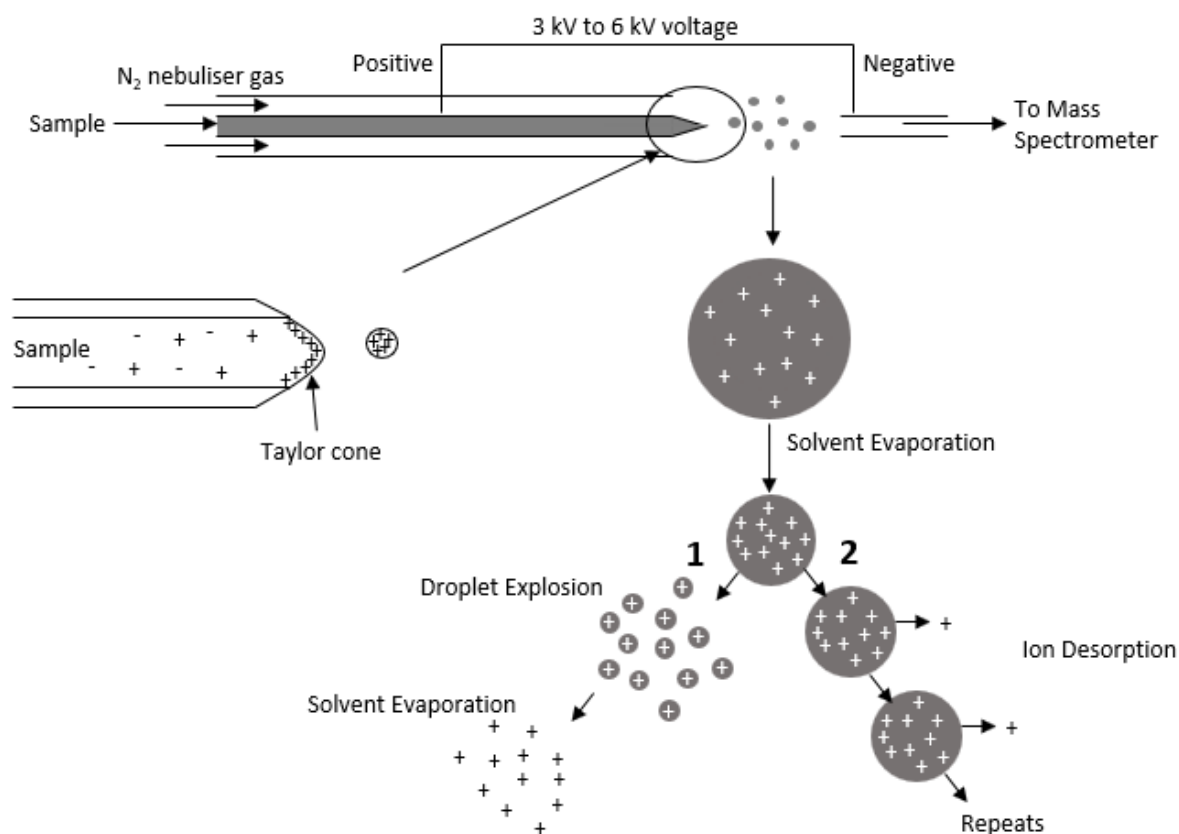
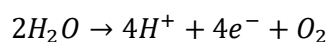


Figure 1.2: process of ESI prior to entering the mass spectrometer – 1) charged residue model, 2) ion evaporation model.

ESI works by dissolving the sample into a solution, which is then pumped through a charged capillary. At the open end of the capillary, the tip is distorted into a cone (called a Taylor cone) in order to create a fine mist of charged nanodroplets with the same polarity as the applied voltage. For example, in positive ion mode, the droplets are charged with an excess of positive ions, such as $M+H^+$, Na^+ , NH_4^+ or K^+ . The main ion considered is H^+ , mostly because protons are generated at the metal/solution interface inside the capillary:



In addition, many solutions are acidic. In the case of this project, the main charge-bearing species likely to be involved are H^+ , Na^+ and K^+ .

1.4.3.1.1 Mechanisms for the formation of gas phase ions

Two mechanisms have been proposed to account for the formation of gas phase ions from the nanodroplets:

1. The charged residue model

When nanodroplets form, some droplets only contain one analyte ion. Once the solvent evaporates from this droplet, the analyte ion is present in the gas phase. This model is generally accepted to be the method by which large globular species are released into the gas phase.^{36–38}

2. The ion evaporation model

This model predicts that when the radii of the droplets shrink to less than 10 nm, direct ion emission from the droplets will occur. This is thought to occur with low MW species that exist as pre-formed ions in solution. The main product created using this model is a “small gas phase cluster”, consisting of the ion and a few residual solvent molecules.

1.4.3.1.2 Droplet Desolvation

Droplets with a high surface-charge density are formed, yielding droplets with a radius of just a few nanometers. Before the ions are mass analysed, the solvent must be removed. The droplets emitted from the Taylor cone undergo rapid solvent evaporation, often heat-assisted with a counter-flow of neutral, heated drying gas (typically N₂).

When the charge density reaches a certain point, direct ion evaporation can occur (see section 1.4.3.1.1). Gaseous analyte ions that are detected by mass spectrometry are then produced from these nanodroplets. This yields naked $[M+H_n]^{n+}$ ions where $n=1, 2$, etc.

1.4.3.2 Tandem Mass Spectrometry

Tandem mass spectrometry can refer to several different experiments, which can be conducted on a variety of instruments. Common MS/MS experiments include product ion scanning, precursor ion scanning, neutral loss scanning, and selected reaction monitoring (SRM). The experiment used in this project for targeted analyses was SRM, conducted on a triple quadrupole LC-MS/MS, shown in **Figure 1.3** (adapted from Figure 4 in “General methods in biomarker research and their applications”, Preedy and Patel³⁹). To carry out SRM, the target analytes must be known, and both an appropriate precursor ion m/z and one of the more diagnostic product ion m/z s must also be known. It is a very useful technique to selectively quantify compounds.

There are three sections to the triple quadrupole: MS1 (the first quadrupole) is fixed to transmit the selected precursor m/z , a collision cell (the second quadrupole) is used to promote fragmentation *via* low energy collision induced dissociation (CID) of the transmitted precursor, and MS2 (the third quadrupole) is fixed to transmit the selected product ion m/z . Since MS1 and MS2 can be set up to target multiple different precursor-product ion pairs or transitions, SRM allows more than one analyte to be targeted in the same run (multiple reaction monitoring (MRM)) and gives good limits of detection because the instrument is recording a limited number of transitions (good duty cycle).

The data recorded show peaks when MS1 transmits an ion with the selected precursor m/z value that then fragments in the collision cell to generate product ions with the selected m/z .

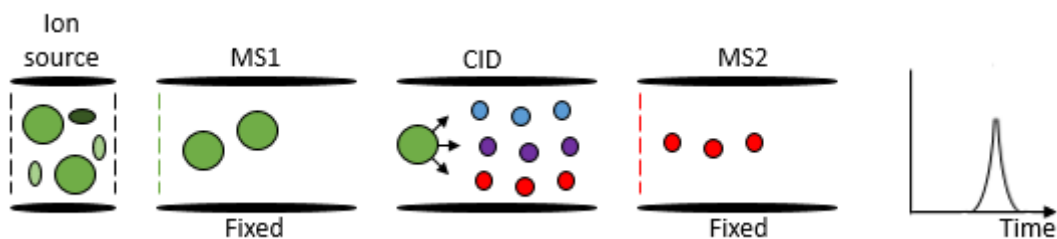


Figure 1.3: SRM showing the selection of one ion, the breakdown of that ion, the selection of one product ion and the signal obtained *via* the detector, where the MS is coupled to an LC.

1.4.3.2.1 Quadrupoles

Quadrupoles are the mass analyser type used as both MS1 and MS2 in a triple quadrupole mass spectrometer such as was being used in this project.

1.4.3.2.1.1 Description

A quadrupole is made up of four rods: a pair of positively charged rods and a pair of negatively charged rods (**Figure 1.4**). It is used as a mass analyser in mass spectrometers and it transmits ions of different m/z values using different combinations of voltages applied to the two pairs of rods. Quadrupoles also act as mass filters with the ability to select specified m/z values and screen out others.

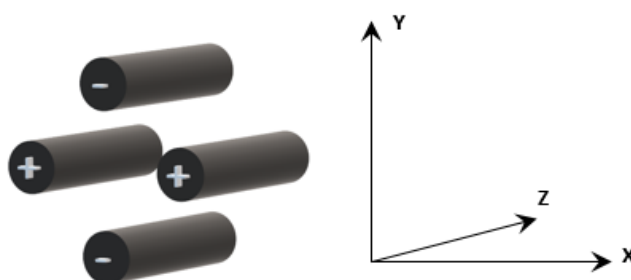


Figure 1.4: four charged rods making up the quadrupole, showing the different axes. The z axis is along the axis of the rods. The negative rods are found in the yz plane, and the positive rods are found in the xz plane.

Prior to entering the quadrupole, ions are created in an ion source (see section 1.4.3.1) and accelerated out of the source into the mass analyser through a hole in a charged metal plate through which they enter the quadrupole. The diameter of the hole defines the diameter of the ion beam entering the quadrupole and results in some slight scattering in the xy planes. This affects how the ions move as some ions are going to be closer to one rod than another. The velocity in the z direction with which the ion travels through the quadrupole is independent of the potentials applied to the rods and can be calculated by a rearrangement of **Equation 1.2**, shown by **Equation 1.3**:

$$\text{Equation 1.2} \quad KE = \frac{1}{2}mv^2 = ze.V$$

$$\text{Equation 1.3} \quad v = \sqrt{2\left(\frac{ze.V}{m}\right)}$$

where KE = kinetic energy; m = mass of ion; z = charge of ion; v = velocity of ion in quadrupole; e = charge of an electron; V = voltage used to accelerate the ion into the mass analyser. The trajectory of the ion in the quadrupole is dependent on the voltages (see section 1.4.3.2.1.2) across the rods, and if the trajectory is stable, the ion will reach the detector and will be measured as a current.

1.4.3.2.1.2 Voltages Applied to Quadrupole Rods

AC and DC voltages are applied to the rods, combining to create alternating electric fields, as shown in **Figure 1.5**. The positive DC is applied to the rods in the xz plane, causing them to be positive for more time than they are negative. The negative DC is applied to the pair of rods in the yz plane, causing them, with the AC voltage, to be negative for more time than positive. To

calculate the exact voltages applied to each rod, **Equation 1.4** (negative rods) and **Equation 1.5** (positive rods) can be used:

Equation 1.4
$$V_1 = V_3 = -(U + V_0 \cos \omega t)$$

Equation 1.5
$$V_2 = V_4 = U + V_0 \cos \omega t$$

where V_x = voltage applied to each rod; U = DC potential; V_0 = AC potential; ω = fixed frequency $\times 2\pi$; t = time.

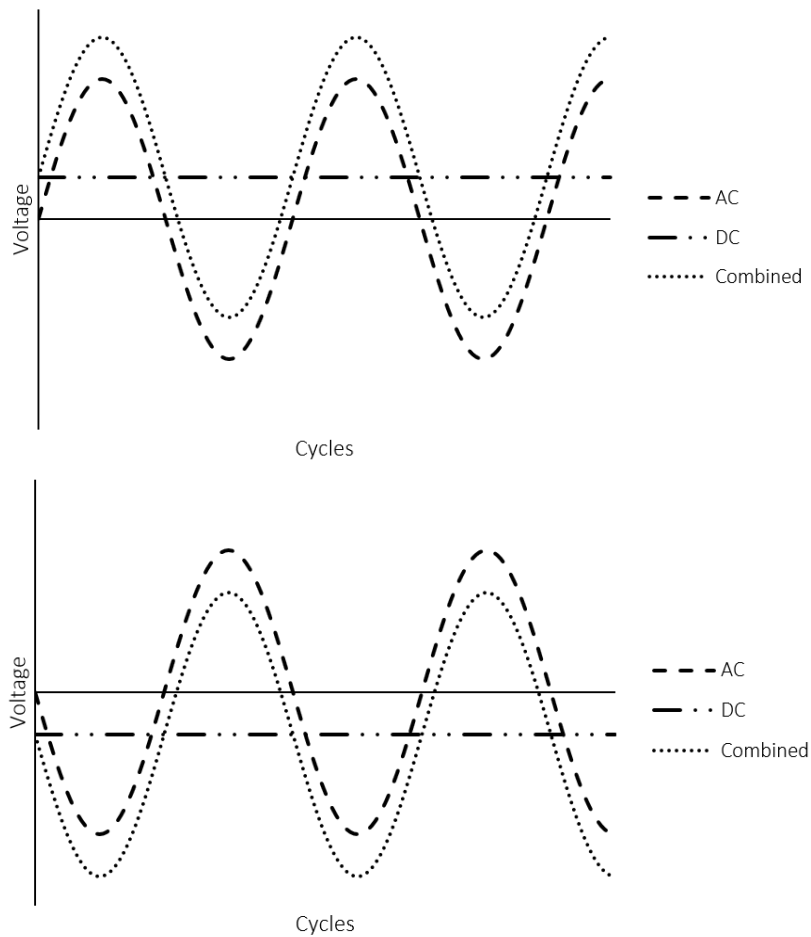


Figure 1.5: combining AC and DC voltages applied to quadrupole rod pairs. Top: positive rods; bottom: negative rods.

1.4.3.2.1.3 Changing charge

Each pair of rods is electrically connected, and so the effect of the combined periodic charges is that the rods change their polarities in pairs. First, the negative rods (1 and 3) become positively charged, then they change back again, while the positive rods (2 and 4) also become negative, so that all four rods are negative at the same time (**Figure 1.6**). The positive rods then become positive again. This alternating of charge occurs up to 50 times throughout the flight of an ion through the quadrupole (length 11 cm).

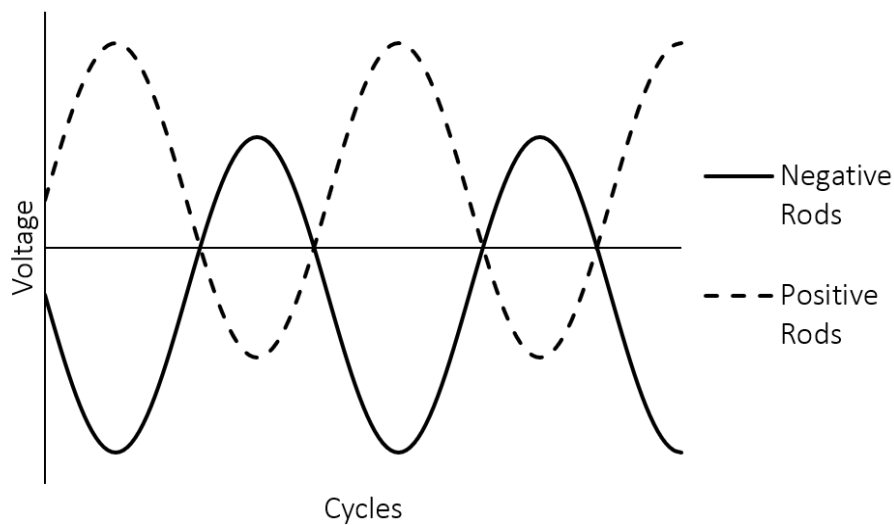


Figure 1.6: the voltage of each pair of rods shown against time.

1.4.3.2.1.4 Movement of ions through the quadrupole

Once the ion packet has entered the quadrupole it is cylindrical in shape, dependent upon the diameter of the entrance hole. The ions are not all exactly on the z axis because the entrance aperture has finite dimensions, which means that some ions will always be closer to one rod than to another. This determines which rod they move to first, as the force from that rod will be greatest and acting most strongly on the ion. The path that ions take as they travel along the quadrupole is shown in **Figure 1.7**.

When the rods are described as “positive” and “negative”, it is not the numeric value of the voltage that is important but the voltage difference between the pairs of rods. The “positive” rods must simply be more positive than the opposite pair of rods, and the “negative” rods must be more negative. Therefore, when a pair of rods is described as “positive”, it is always referring to the rods being more positive than the other pair.

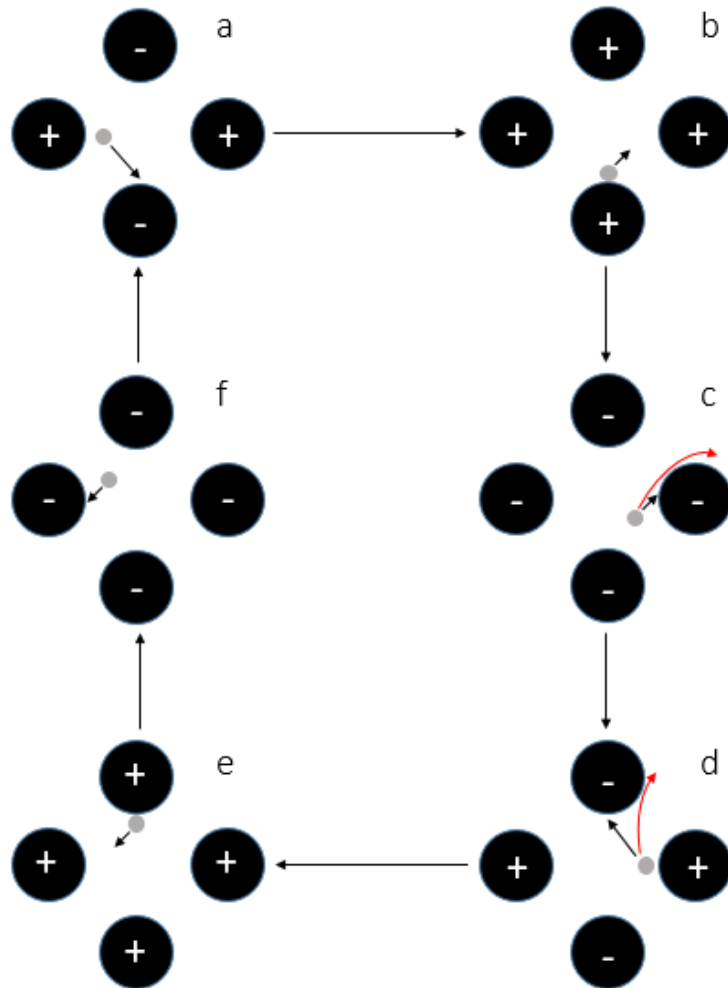


Figure 1.7: pathway taken by ions travelling through the quadrupole. The red arrow at c represents the light ions being lost, and the red arrow at d represents the heavy ions being lost.

Starting at (a), the positively charged ion is attracted to the negatively charged rod. This rod then becomes positively charged, repelling the ion (b). All four rods become negatively charged, and

due to the momentum of the rod carrying the ion forward, the positively charged ion is attracted to the next negatively charged rod (c). At this stage any ions that are lighter than the target ion are lost, because they require much less force to change their trajectory (lost to the positively charged rods – red arrow). Any ions remaining carry on, being repelled by the positive rods (d). This next stage is where any heavier ions are lost, as they require much more force to change the trajectory than the target ion. They are therefore not “saved” by the brief positive charge and collide with the rod (lost to the negatively charged rods – red arrow). This pathway shown will always result in an unstable trajectory, with the circular path continually increasing, and so the ion will never reach the detector. For the ion to have a stable trajectory, it must simply stay in the centre of the quadrupole, and travel in a straight line until it reaches the detector.

1.4.3.2.1.5 Simple Stability Diagram

The simple stability diagram (**Figure 1.8**) shows the region in which an ion with a particular m/z is stable and retained within the quadrupole. The basic concept of the simple stability diagram is that any ion falling within the “triangle” is transmitted, while any outside it is unstable and does not reach the detector. Ions to the left of the triangle are unstable in the y plane (ions with m/z higher than the transmitted m/z), and ions to the right are unstable in the x plane (m/z s lower than the transmitted m/z). Simple stability diagrams are specific for a particular m/z and are based on two main assumptions: first, that low radio frequency (RF) voltages (V_0) are stabilising, and second, that high RF voltages are destabilising. Applied DC voltages are also destabilising.

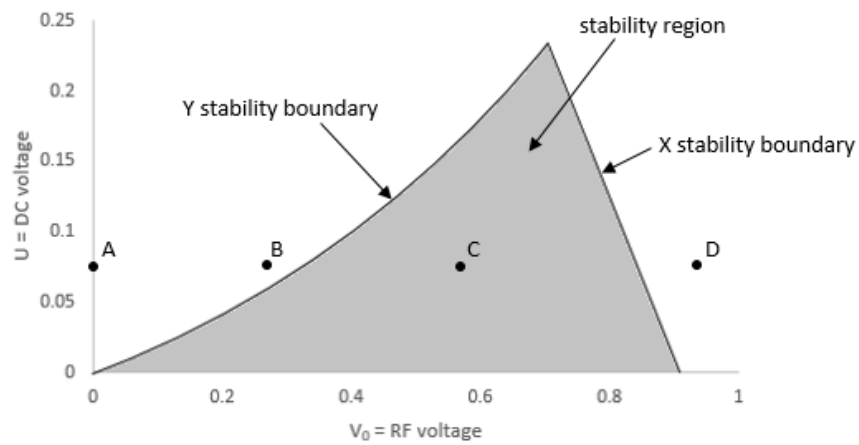


Figure 1.8: simple stability diagram. At point A, (DC voltage only) the ions are stable on the x axis (repelled by the positive rods) but unstable on the y axis (lost to the negative rods). At point B, the RF voltage is not large enough to offset the DC voltage, and so the ion is again lost to the negative rods. At point C, the ion is stable. At point D, the RF voltage is destabilising, causing the ion to be lost on the x axis.

The y stability boundary has a positive slope due to the RF voltage (V_0) needing to offset the effect of the DC voltage (U). As U increases, V_0 must also increase. In contrast, the negative slope of the x stability boundary is due to the ion trajectory being mostly independent of the DC voltage. This is because when the RF voltage is high, the effect of the DC voltage is negligible. The DC voltage does, however, reinforce the RF voltage by a small amount, which means that when U increases, the value of the RF voltage required to make the trajectory unstable decreases.

At point A (**Figure 1.8**), there is no RF voltage and so the positive rods repel the ion equally causing it to oscillate along the x axis (stable). Because there is no RF voltage, the negative DC voltage is not offset, and a positive ion is instantly neutralised on the negative rods (i.e. lost along

the y axis). As the RF voltage increases, it compensates for the effects of the DC voltage. Just before crossing over the y stability boundary, at point B, the RF voltage is not quite strong enough to offset the effect of the DC voltage, which results in the ion being neutralised by the negative rods. In the stable region, at point C, the RF voltage is strong enough to counter the effect of the DC voltage along the y axis and is still low enough to be stabilising along the x axis. This allows the ion to reach the detector. As the RF voltage increases further it will exceed the stability boundary along the x axis (point D). This causes the ion to remain stable on the y axis (although with much more energy, creating much larger oscillations) – the amplitude of the ion path becomes larger than the dimensions of the quadrupole and so the ions are lost. When *only* RF voltage is applied (no DC voltage), the quadrupoles act as ion transmission devices, rather than acting as mass filters.³⁵ A large range of m/z values can pass through when in this mode.³⁵

1.4.3.2.1.6 Generalised Stability Diagram

To make the simple stability diagram applicable to a range of masses, U and V_0 must be adapted, in order to account for mass, shown in **Equation 1.6** and **Equation 1.7**:

Equation 1.6

$$\alpha = \frac{8eU}{mr_0^2\omega^2}$$

Equation 1.7

$$q = \frac{4eV_0}{mr_0^2\omega^2}$$

where e = charge of an electron; U = DC voltage; m = mass; r_0 = distance between z axis and the edge of the rods; ω = fixed frequency $\times 2\pi$.

To account for all different m/z values, the generalised stability diagram was created (**Figure 1.9**).

There are two important applications of this diagram: it reveals how the quadrupole acts as a mass filter, and it reveals how the quadrupole can produce a mass spectrum.

At a certain resolution, the apex is always found at point (0.706, 0.237), and the x stability boundary line always terminates at point (0.91, 0).

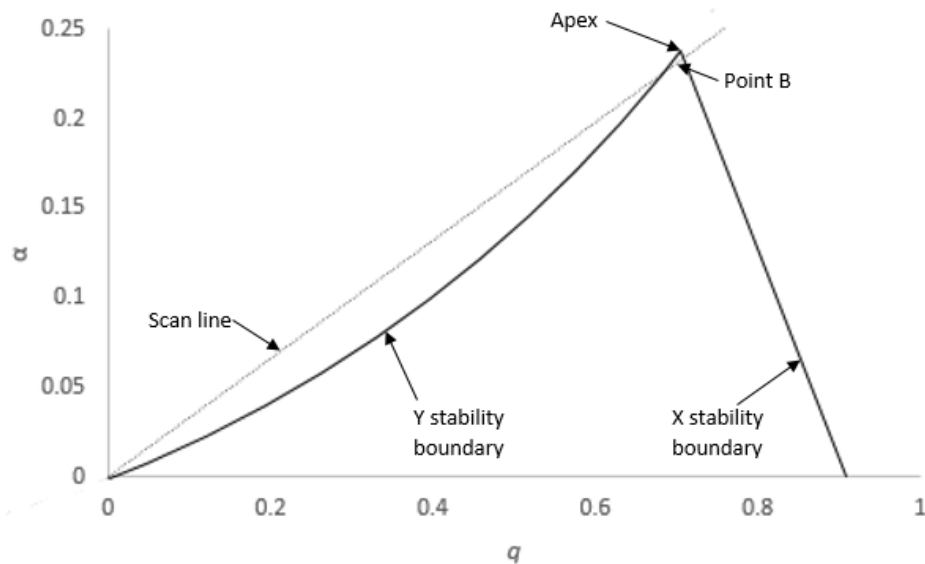


Figure 1.9: generalised stability diagram with dimensionless α and q .

1.4.3.2.1.7 The quadrupole as a mass filter

For the quadrupole to act as a mass filter it must be able to distinguish between m (mass), $m+1$ and $m-1$ for unit resolution. To find a point that allows the target ion to reach the detector, but no other ion, causes some problems. Theoretically, the apex could be used – however, this is practically not possible because any random fluctuations in the voltages will cause the target ion to be lost due to a temporarily unstable trajectory. Point B is therefore chosen, as enough of the surrounding points are outside the stability region but small changes to the voltage do not disrupt the target ion reaching the detector. Point B is always found at point (0.706, 0.233). For specific values of U and V_0 , every m/z value in the mixture will fall somewhere on the scan line, with heavier m/z ions falling closer to the origin and lighter ions falling further away. Provided $m-1$ and $m+1$ lie outside the stability region, the quadrupole is acting as a mass filter.

1.4.3.2.1.8 Scanning a mass spectrum

To successfully obtain a mass spectrum, the quadrupole must first be tuned such that mass m will be found at point B. This fixes the ratio of U to V_0 . Once this has been set, every m/z must be taken through point B, by scanning the voltages in a fixed $U:V_0$ ratio. Point B can be adjusted depending on the resolution needed for the mass spectrum.⁴⁰ The mass spectrum is acquired by starting at a low value of U and V_0 and steadily increasing both. The ratio between them must be kept constant (**Equation 1.8**). These values of U and V_0 map onto the scan line. If the mass spectrometric resolution needs to be increased, the gradient of the scan line can be increased as well to match this. This will then result in point B being in a different place. The computer outputs the voltages needed for each different ion, which can be recorded and input again for the same mass (provided the resolution is the same).

Equation 1.8

$$\frac{U}{V_0} = \frac{1}{2} \left(\frac{0.233}{0.706} \right)$$

1.4.3.2.2 Summary of Tandem Mass Spectrometry

Using triple quadrupole mass spectrometry allows adequate limits of quantification due to improved signal to noise ratios (see section 2.4.2), in addition to having adequate sensitivity (particularly at low concentrations).⁴¹ However, analysis using the triple quadrupole was not appropriate for every experiment conducted as part of this project, and so other mass spectrometers were also used.

1.4.3.3 Fourier-Transform Ion Cyclotron Resonance (FT-ICR)

The FT-ICR has some advantages over triple quadrupoles that are suitable for some of the experiments in this project (see Chapter 4). These can be found in section 1.4.3.3.5.

The FT-ICR is a type of mass spectrometer that works by measuring the cyclotron frequency of the ions trapped in a fixed magnetic field.⁴²

There are four main stages in the process of producing a mass spectrum using an FT-ICR instrument: trapping in the Penning trap, excitation, detection and Fourier transformation.

1.4.3.3.1 The Penning trap

The Penning trap is made up of six plates, arranged as a cuboid (**Figure 1.10**). The two end plates (xy plane) are called the trapping plates, the plates in the xz plane are the excitation plates and the plates in the yz plane are the detector plates.

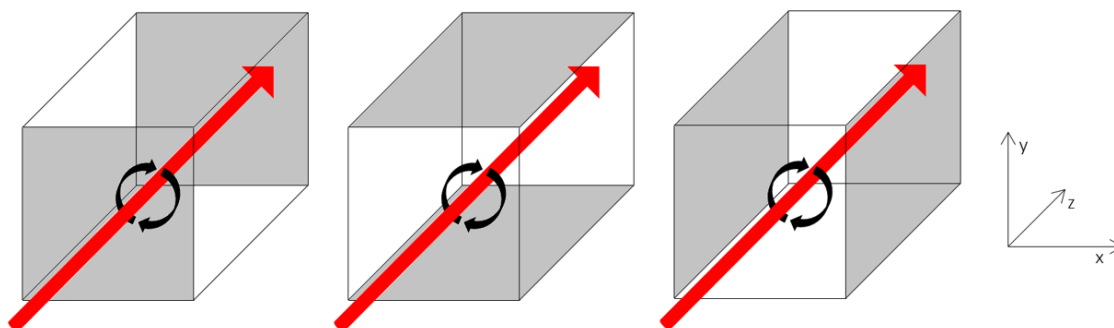


Figure 1.10: FT-ICR instrument set-up, showing the trapping plates (left), excitation plates (middle) and the detector plates (right). The red arrow shows the magnetic field applied to the Penning Trap.

Inside the Penning trap, the ions all move differently, known as the cyclotron frequency (otherwise known as the circular frequency). This can be calculated using **Equation 1.9**.

$$\text{Equation 1.9} \quad v_c = \frac{1.535611 \times 10^7 B}{m/z}$$

where v_c = cyclotron frequency and B = magnetic field strength.

The ICR frequency is independent of velocity. Consequently, ions with the same m/z ratio have the same ICR frequency. This is very important, as this independence is one of the reasons why such high resolution is achievable in an FT-ICR instrument. The high resolution also makes good mass accuracy (with careful calibration) much easier to achieve. It is much easier to find the middle, or “apex”, of a narrow peak compared to a wide peak. In order to maintain good accuracy in the FT-ICR instrument, a very stable magnetic field is required. At a typical magnetic field value, cyclotron frequencies for typical masses range between a few kHz to MHz. The larger the magnetic field, the higher the m/z that can be trapped.

1.4.3.3.2 *Excitation of Ions*

An alternating electrical field is applied across the two excitation plates, exciting the ions trapped inside. As the ions are excited, their frequency increases. The ICR frequency must be reached to bring the ions into phase, allowing them to travel as a coherent packet.

Bringing the ions into phase with each other is a very important stage, as if the ions are not in phase, any ions that are 180° offset from each other would cancel out when they generate their detector currents. Exciting the ions also increases the radius of the ions' path, bring them closer to the detector plates.

The post-excitation orbital radius can be calculated using **Equation 1.10**. It should be noted that the post-excitation orbital radius is independent of m/z .

Equation 1.10

$$r = \frac{V_{p-p} \times t_{excite}}{2B_0}$$

where r = post-excitation orbital radius, V_{p-p} = voltage between plates, T_{excite} = time voltage is applied for, d = distance between plates, and B_0 = static magnetic field.

1.4.3.3.3 *Detection of Ions*

Ions are detected because they induce an alternating current in the detection plates. The alternating current creates an image current (section 1.4.3.3.3.1). The signal recorded is proportional to the induced current and is independent of the magnetic field strength.

1.4.3.3.3.1 *Broadband Image Current Detection*

Broadband image current detection is a non-destructive detection technique.⁴³ It is based on the principle that as an ion approaches a piece of metal, it induces an increasing "image charge" on said metal. This means that as the positive ions approach the outer electrodes, there will be a build-up of negative charges on the surface due to electrostatic attraction. The closer the ions are to the metal surface the more negative charges will be attracted. This is referred to as an "image current". As the positive ions move away from the metal surface, the amount of negative charges will decrease, resulting in an image current in the opposite direction. This allows the motion of ions to be detected, and so the packets of ions moving at different frequencies can be identified.

1.4.3.3.4 Fourier transformation

One of the issues with all the ions being excited as a coherent packet is that all the ions are detected simultaneously. Therefore, a Fourier transformation is required to resolve the different frequencies of the different m/z species in the Penning trap. The Fourier transformation results in a m/z spectrum, showing the m/z against intensity of each ion.

1.4.3.3.5 Summary of FT-ICR

One of the main advantages to FT-ICR is the high mass resolution. The mass resolution increases as the magnetic field strength increases, and so it is possible to reach both very high mass accuracy and very high mass resolution. The FT-ICR was used to mass measure products of the degradation experiments (see Chapter 4), and so in order to interpret the results and identify the potential structures of the unknown ions, high mass accuracy was required. As such, the FT-ICR was more appropriate to use than the triple quadrupole.

Another advantage to the specific instrument used in this project was the ability to use MALDI as the source, instead of ESI, as this allowed a wider variety of experiments for the analysis of compounds with poor ion, as demonstrated in section 2.3.5. This was useful for antibiotics that did not ionise well using ESI.

1.4.3.4 Orbitrap Mass Analyser

Another instrument used in this project was the orbitrap mass analyser – a particular form of ion trap.⁴⁴ It utilises axially symmetric electrodes, which create a combined electrostatic potential. A stable ion trajectory must have both orbiting motion around the central electrode and simultaneous oscillations along the central electrode (shown in **Figure 1.11**).

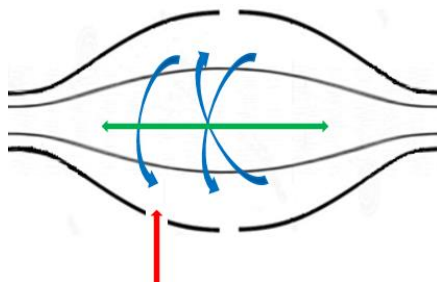


Figure 1.11: orbitrap mass analyser simplified diagram. Red arrow indicates where the ions enter the orbitrap. The blue arrows represent the orbiting motion around the central electrode, and the green arrow represents the oscillations along the central electrode.

The ions enter the Orbitrap from a curved linear trap (c-trap). The c-trap is required to couple the ESI source with the Orbitrap, as the ESI source produces a continuous stream of ions and the orbitrap requires the ions to enter in pulses. The c-trap holds the ions until a certain number have been accumulated, before sending them to the Orbitrap. Once the ions enter the Orbitrap cell, the voltage of the inner electrode increases until the ions have reached their desired orbit (known as “squeezing” the ions). The ion packets then start coherent axial oscillations since the motion along the central electrode is completely independent of the orbiting motion around the central electrode. It is also independent of all initial parameters of the ions, except for the m/z value. The m/z value determines the frequency of ion oscillation along the central electrode. The coherent packets are detected

by broadband image current detection (section 1.4.3.3.3.1), which results in a recorded time-domain signal. This is then transformed into a mass spectrum by Fourier transformation.

1.4.3.4.1 *Summary of the Orbitrap Mass Analyser*

The main advantages to the Orbitrap mass analyser are the high mass resolution and mass accuracy and very favourable limits of detection on the instrument used here (Orbitrap Fusion). The Orbitrap also has two energy regimes for collision induced dissociation, one of which is a higher energy regime. This allows for more structurally useful CID fragmentation than is available at lower collision energies, and as such was used on three of the 11 antibiotics in order to gain a better understanding of how they fragmented (i.e. identifying primary fragments and secondary fragments – see section 4.3.4).

1.4.3.5 *Laser Interfaced Mass Spectrometer (LIMS) Ion Trap*

The final mass spectrometer used in this project was a laser interfaced ion trap. The ion trap was interfaced with two lasers – a visible laser and a UV laser.

The antibiotics were introduced into the ion trap, using ESI as the ionisation source. The solvent is then removed, before the antibiotics enter the ion trap. Here, the ion trap acts in a very similar manner to the orbitrap (see section 1.4.3.4), selecting one m/z window using an electric field. In this project, only the UV laser was used. Once the antibiotics have been isolated, the laser (set to either scan the entire UV spectrum or to irradiate with one specific wavelength) was set to fire, causing the antibiotic to photofragment. The photofragments are then detected and the wavelength at which they were formed (and the intensity at which they were produced) is recorded.

1.4.3.5.1 *Summary of the LIMS*

The LIMS was used as it enabled the analysis of antibiotics in the gas phase and allowed photolysis (see section 4.1.1) to occur without involvement of the solvent i.e. hydrolysis (see section 4.1.2).

Chapter 2 Development of an LC-MRM Method for Detection and Quantification of Antibiotics in Soil Pore Water and Leachate

Samples

2.1 Introduction

The aim of the work described in this chapter was to develop a suitable LC-MS/MS method for the analysis for the 11 antibiotics studied in this project: cefalexin, penicillin v, amoxicillin, tetracycline, oxytetracycline, trimethoprim, clarithromycin, erythromycin, metronidazole, ciprofloxacin and colistin b.

In order to be able to determine the concentrations of these 11 key antibiotics in plant soil leachate, pore water and the rhizosphere (defined in section 3.1.1), an appropriate LC-ESI-SRM method needed to be developed and validated, before being applied to the analysis of the mesocosm-derived samples.

2.2 Materials

All compounds, reagents and solvents were analytical grade, unless otherwise stated. Cefalexin, penicillin v, amoxicillin, tetracycline, trimethoprim, clarithromycin and erythromycin were purchased from Sigma Aldrich (Dorset, United Kingdom). Metronidazole was purchased from Alfa Aesar (Lancashire, United Kingdom). Ciprofloxacin was purchased from Fluka Analytical (Bucharest, Romania). Oxytetracycline was purchased from Acros Organics (New Jersey, United States of America). Stable isotope-labelled internal standards were purchased from Toronto Research Chemicals (Toronto, Canada) (azithromycin-d3 and amoxicillin-d4) and Sigma Aldrich (Dorset, United Kingdom) (ciprofloxacin-d8, trimethoprim-d9, metronidazole-d3 and sulfamethoxazole-d4). Solvents (methanol, acetonitrile and formic acid) were purchased from Sigma Aldrich (Dorset, United Kingdom). Citric acid was purchased from BDH laboratory supplies,

and ammonium acetate was purchased from Fischer Chemicals (Zurich, Switzerland). The HPLC grade water was purchased from Merck, and LCMS grade water was purchased from Fischer Chemicals (Zurich, Switzerland).

2.3 Method Development

A modified version of the standard United States Geological Survey (USGS) LC-SRM method⁴⁵ for detecting pharmaceuticals in water, using a triple quadrupole LC-ESI-MS/MS, provided a good starting point because it targeted a wide range of pharmaceuticals, which included some antibiotics. The approach relied on the use of 100% methanol and 0.1% aqueous formic acid as the two LC mobile phases, and a C18 column.

2.3.1 Definition of a Robust Method

To develop a robust LC-MS/MS method, there are several requirements. First, the precursor ion-product ion transitions must be optimised (section 2.3.2), in order to use the ions with the highest intensity when the antibiotic fragments *via* collision induced dissociation (see section 1.4.3.2.1). Next, the mobile phase needs to be selected (section 2.3.3). This affects the retention time (the length of time it takes the antibiotic to elute from the column – see section 1.4.2) and can suppress/promote the ionisation of the analytes.⁴⁶ Most importantly, it must be capable of dissolving the analytes at the concentration required for analysis.⁴⁶ Finally, the column itself needs to be selected (section 2.3.4).

A good method can be identified by several key data criteria⁴⁷:

1. Peak shape
2. Separation Efficiency (section 1.4.2)
3. Limits of Detection (section 2.4.2)

2.3.1.1 Peak Shape

Having a good peak shape is important for several reasons, including improved resolution and more accurate quantitation. A good peak shape can be defined using these three criteria:

1. tailing factor of 1.0
2. high efficiency (see section 1.4.2)
3. narrow peak width

The tailing factor can be measured by **Equation 2.1**, and doing the calculations shown in **Figure 2.1** (figure modified from “The Secrets of Good Peak Shape in HPLC Choosing Columns and Conditions for the Best Peak Shape”, published by Agilent Technologies).

Equation 2.1

$$T_f = \frac{W_{0.05}}{2f}$$

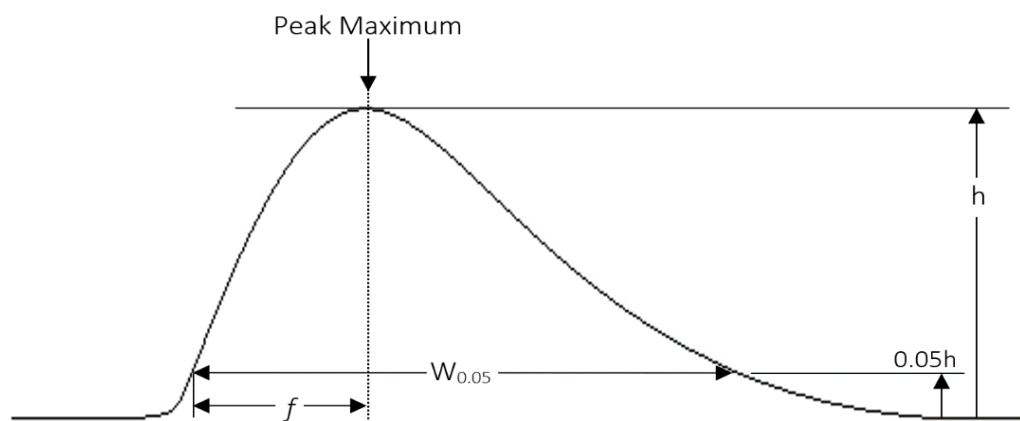


Figure 2.1: a demonstrative tailing peak, labelled with measurements needed to calculate the tailing factor (Equation 2.1).

Peak width is defined as the peak width at half height. It is measured in a similar way to $W_{0.05}$ (Figure 2.1), but instead of using 0.05h, 0.5h would be used. The lower the number, the narrower the peak.

2.3.2 Determining SRM transitions for the 11 Antibiotic Analytes

Identification of appropriate precursor ion-product ion transitions for selectively monitoring the analyte antibiotics began with the acquisition of the product ion spectra of the 11 antibiotics on the instrument to be used for the SRM experiments. A solution containing all 11 antibiotics, dissolved at 1 $\mu\text{g/L}$ in 10% aqueous methanol was thus continuously infused into the ESI source of the Thermo Scientific TSQ Endura™ triple quadrupole mass spectrometer using the positive ion mode. Automated source setting optimisation was carried out (using Thermo's TraceFinder software); it optimises the intensities of the precursor ions, in addition to optimising the collision energy setting and the RF lens voltage. Once appropriate precursor and product ions had been found using an alternative solvent, the sample mixture was then directly infused into the triple quadrupole instrument using the optimised source conditions, and with Q1 set to the m/z value for the precursors observed. An automated range of collision energies and RF lens voltages was scanned to generate complete product ion spectra for each analyte. The software automatically reports the two most intense product ions. The most intense was selected for quantification, while the second was used for confirmation.

The ESI chromatograms of the antibiotics were recorded on the FT-ICR mass spectrometer and inspected to determine whether sodiated or ammoniated species were produced in addition to the protonated species that had previously been monitored. Sodiated species were indeed observed for all the antibiotics at approximately similar relative intensity as the protonated species, colistin being the exception where only the $[\text{M}+2\text{Na}]^{2+}$ peak was observed. For this reason, the source conditions and the transitions for the antibiotics were reoptimized on the triple quadrupole instrument using direct infusion and the method described in section 2.3.2. For

amoxicillin, the sodiated precursor molecule had the highest intensity, for colistin b, the doubly protonated molecule still had the highest intensity, and as expected, the singly protonated precursors had the highest intensity for the remaining nine antibiotics. This highlights the significant impact that electrospray ion source engineering has on ion speciation. Despite this, when analysing a solution of an authentic standard, the peak produced for protonated amoxicillin was had a higher intensity than the peak produced when amoxicillin became sodiated. Therefore, the precursor ions remained the same as before, with the refined product ions. These ions can be found in **Table 2.1**.

Table 2.1: Instrument optimisation results for antibiotics dissolved in acetonitrile and water.

Compound	Quantification			Confirmatory		RF Lens
	Precursor <i>m/z</i>	Product Ion <i>m/z</i>	Collision Energy	Product Ion <i>m/z</i>	Collision Energy	
Metronidazole	172.1	128.0	14.0	82.2	24.7	104.3
Trimethoprim	291.2	260.9	25.5	230.1	24.1	196.6
Ciprofloxacin	332.2	288.0	17.7	291.0	10.3	207.5
Cefalexin	348.1	158.0	10.3	174.0	14.1	126.2
Penicillin v	351.1	160.0	10.3	310.1	10.3	128.9
Amoxicillin	366.1	349.1	10.3	208.0	12.4	131.9
Tetracycline	445.2	410.1	19.3	427.2	12.9	187.4
Oxytetracycline	461.2	426.0	19.4	443.1	12.4	186.2
Colistin b	578.7	529.0	14.9	628.4	21.8	298.5
Erythromycin	734.5	576.4	18.8	558.3	14.7	239.6
Clarithromycin	748.7	590.3	18.0	558.3	21.4	246.0

2.3.3 Solvent Selection

2.3.3.1 Assessment of 100% Methanol and 0.1% Formic Acid as the Mobile Phases

Initially 100% methanol and 0.1% aqueous formic acid were used as the respective organic and aqueous mobile phases. The initial assessment *via* direct infusion to the triple quadrupole of the antibiotics using these mobile phases resulted in a successful attempt to detect seven of the 11 antibiotics. As such, an alternative solvent was looked for to test the remaining four antibiotics that were not detectable in this solvent (colistin b, amoxicillin, cefalexin and penicillin v).^{48,49}

2.3.3.2 Assessment of Acetonitrile and 0.1% Formic Acid as the Mobile Phases

Changing the solvent meant that the precursor-product ion transitions were reoptimized (see section 2.3.2). All 11 antibiotics were dissolved at 1 mg/L (2 mg/L for colistin b) instead of 1 µg/L as in section 2.3.2, to eliminate low concentrations as a possible reason for failure to detect the four missing antibiotics. Acetonitrile was used in place of methanol⁵⁰, and automated source setting optimisations (defined in section 2.3.2) were once again used to identify antibiotic product ions. All 11 analytes generated positive ion molecular species. Colistin b ionised as the $[M+2H]^{2+}$ ion, while the remaining ten antibiotics ionised as $[M+H]^+$, in agreement with other studies identified in the literature.²⁵ Colistin producing a doubly charged species is likely to be due to the larger size of the colistin b molecule, and the presence of five potential protonation sites.

2.3.3.3 Preparation of a Calibration Curve

Having identified appropriate precursor ion-product ion transitions for the analytes, the next step was to implement these settings in an LC-MRM method. Solutions of authentic standards for each antibiotic were made up in 90:10 0.1% aqueous formic acid: acetonitrile, at concentrations of 1, 4, 10, 40, 100, 400, 1,000, 2,000, 4,000 and 10,000 ng/L, in order to test the transitions

determined. Acetonitrile was selected as similar studies being carried out on antibiotics used this solvent (such as Barcelo *et al*)²⁵. This range of calibration concentrations was chosen to capture the predicted environmental level (**Table 3.1**). 0.1% formic acid was included in the aqueous phase in line with the Furlong protocol.⁴⁵

2.3.3.4 Assessment of Calibration Signals

The standard solutions were analysed on a triple quadrupole LC-ESI-MS/MS instrument, based on the LC conditions described by Furlong, but using acetonitrile rather than methanol. Peaks for eight of the 11 antibiotic analytes were generated and decreased in intensity as the concentration of the injected solution dropped. In the case of colistin b, peaks were not observed using the transitions and settings determined as described in section 2.3.2. This was unexpected, since Zhao *et al*⁵¹ have previously published product ion spectra of this analyte using the same transitions as in this project, although not on the same instrument as used here. Subsequent efforts to identify appropriate product ions, by directly infusing colistin b into an FT-ICR instrument at 2 mg/L, followed by CID and product ion analysis, managed to produce a product ion mass spectrum. However, all product ions generated on the FT-ICR instrument failed to generate when directly infused in the triple quadrupole instrument. Consequently, the MRM method for the triple quadrupole was modified to use the $[M+2H]^{2+}$ precursor ion m/z value in place of a product ion transition for colistin b detection (see section 2.3.5 for further experimentation on colistin b). When examining the data from the LC-MRM analysis, the signals for metronidazole, trimethoprim, ciprofloxacin, clarithromycin, erythromycin, tetracycline and oxytetracycline were less intense and reproducible than anticipated on the basis of the literature⁴⁵ and data from colleagues using the Furlong method (i.e. in methanol rather than acetonitrile).

The chromatograms for amoxicillin, colistin and penicillin v showed peaks, but closer examination revealed that these peaks were not derived from species giving both the quantification and

confirmatory ions (**Table 2.1**) for each antibiotic, and therefore the peaks could not be considered to correspond to the analytes. The chromatogram for cefalexin contained two peaks with good signal: noise, one at t_R 3.98 min, and a second at t_R 7.45 min (**Figure 2.2**). The earlier eluting signal derived from a species giving both transitions, while the second peak derived only from the confirmatory ion and not the quantification product ion and so was excluded. Since use of acetonitrile with formic acid failed to generate data for all 11 antibiotics, further solvent options were considered.

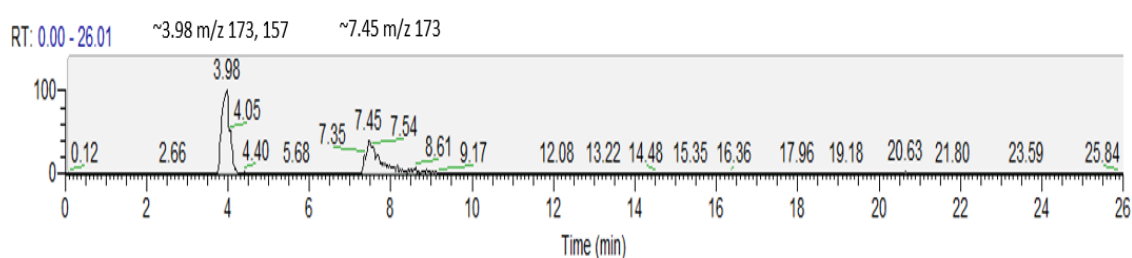


Figure 2.2: chromatogram of cefalexin, with a mobile phase consisting of acetonitrile and 0.1% aqueous formic acid.

Since the seven antibiotics also included in the Furlong method were readily analysed using methanol, an alternative approach for the four remaining analytes was sought (amoxicillin, cefalexin, penicillin v and colistin b), with the additional aim of testing whether an alternative solvent might also prove to be more appropriate for analysis of tetracyclines, which tend to behave rather poorly (i.e. generating peaks that were tailing – see section 2) compared to many of the analytes in the Furlong method; it would be useful if a better approach for tetracyclines could be found. The following method assessed the four remaining antibiotics (amoxicillin, cefalexin, penicillin v and colistin b) plus tetracyclines (tetracycline and oxytetracycline).

2.3.3.5 Assessment of Acetonitrile and 25 mM Ammonium Acetate as the Mobile Phases

Further investigation into the literature, looking for an alternative aqueous solvent, gave the suggestion of using 25 mM ammonium acetate^{52,53} in place of water and so the automated source settings were used to optimise the collision energy and RF lens values for penicillin v, cefalexin, amoxicillin, colistin and the two tetracyclines (TCs). The precursor-product ion transitions were also optimised (section 2.3.2). The four antibiotics plus TC antibiotics were dissolved in 10% 25 mM aqueous ammonium acetate: 90% acetonitrile, identifying the precursor ion-product ion transitions and their respective collision energies and RF lens values. Following the optimisation, three calibration standards (1, 100 and 10,000 ng/L) were analysed on the triple quadrupole LC-ESI-MS, using ammonium acetate and acetonitrile as the mobile phase (example chromatogram for cefalexin shown in **Figure 2.3**). There are three different chromatograms displayed that were obtained from three different concentrations of cefalexin: 1, 100 and 10,000 ng/L. At the higher concentrations (100 and 10,000 ng/L), there was one peak with good signal: noise at t_R 5.45. This peak was not present in the chromatogram of the 1 ng/L solution of cefalexin. The peak at t_R 5.45 derived from a species containing both the confirmation and quantification transitions, and so was confirmed to be cefalexin.

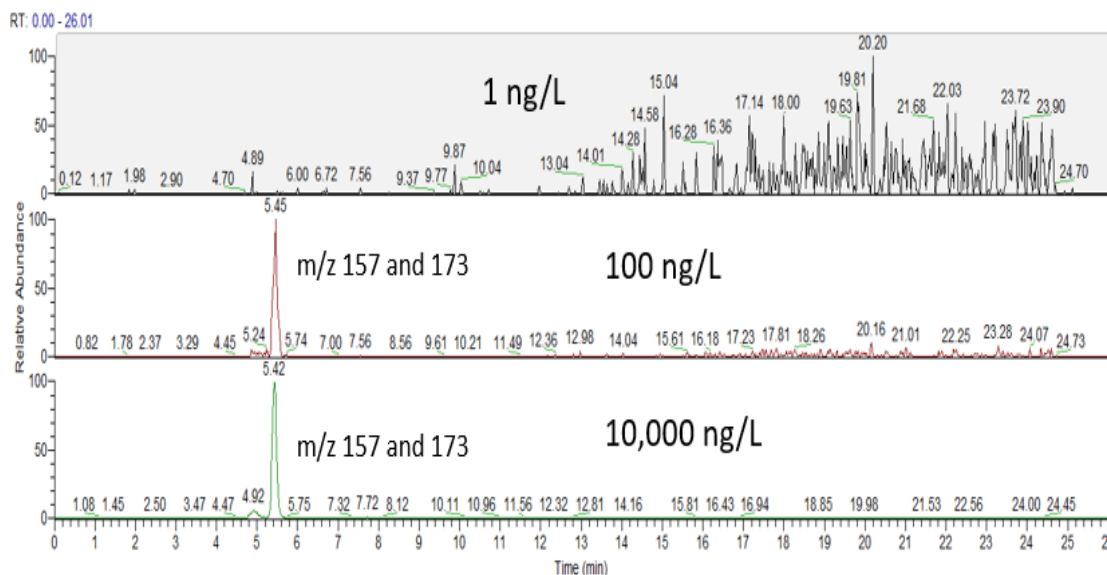


Figure 2.3: chromatogram of cefalexin, with mobile phases consisting of acetonitrile and 25 mM ammonium acetate. Top: 1 ng/L, middle: 100 ng/L, bottom: 10,000 ng/L.

This showed that the mobile phase selected allowed detection of cefalexin, and so further experimentation could take place. Peaks were also observed for amoxicillin and penicillin v.

The retention times observed for each antibiotic in solutions of several different concentrations revealed that the times remained very consistent for each antibiotic (excepting colistin b). The method was thus refined to monitor the relevant transitions only in specific retention time windows, in order to improve the limit of detection by improving the duty cycle, and to reduce the risk of observing interfering impurities. A retention window of 1 min was used for penicillin v, cefalexin and amoxicillin, and a window of 3 min was used for the tetracyclines (due to tailing) and colistin b (due to poor peak shape). The resulting chromatograms gave clearly defined single peaks for penicillin v, cefalexin and amoxicillin that increased in intensity when higher concentrations were injected (**Figure 2.4**).

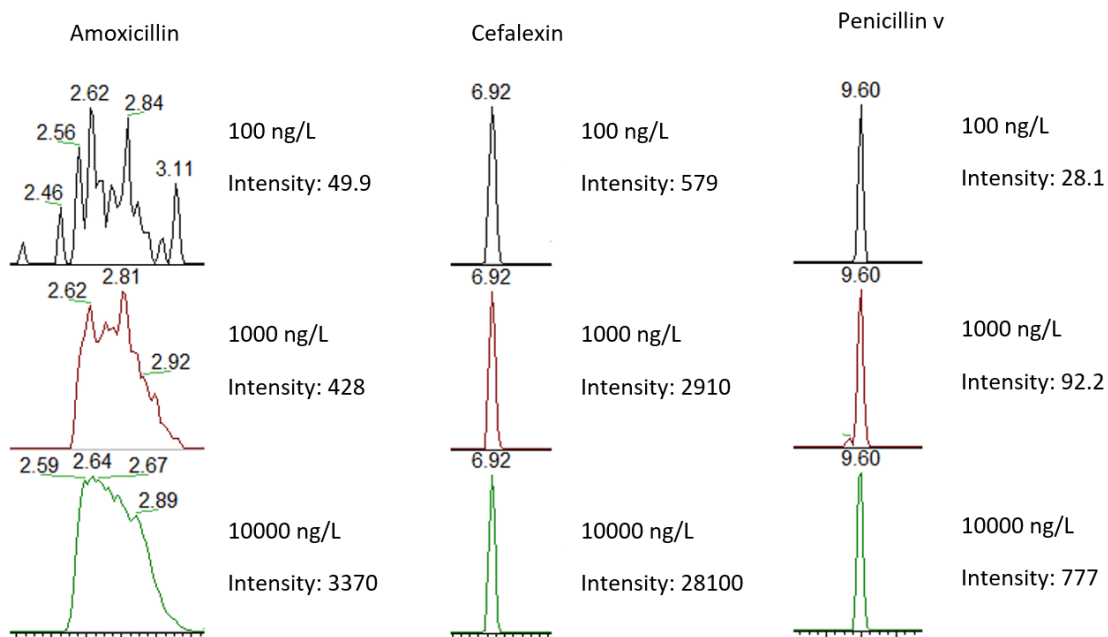


Figure 2.4: peaks from the LC-MS/MS chromatograms of amoxicillin (left), cefalexin (middle) and penicillin v (right), showing the increase in intensity as the concentration increases. Mobile phases: acetonitrile and 25 mM ammonium acetate.

A summary of the mobile phases used for each antibiotic is given in section 2.5, and an example calibration curve is shown in Figure 2.5.

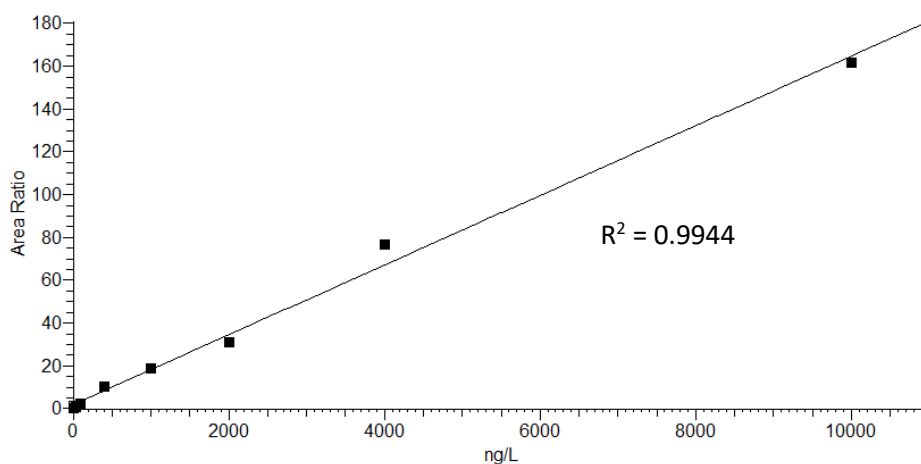


Figure 2.5: calibration curve showing 10 points (1, 4, 10, 40, 100, 400, 1,000, 2,000, 4,000, 10,000 ng/L) for clarithromycin.

2.3.4 Influence of Column Chemistry

Initially, the column used for all analyses was a C18 column (Waters XSelect CSH). However, it was noticed that this caused the peak shapes of the TCs to tail, and so to try and improve the peak shape, a second column (a T3 column (Waters CORTECS)) was tested. Due to the precise chemistry of the two columns being proprietary, it is difficult to compare the chemistries of the T3 column and the C18 column. However, more general information about the T3 column is available, and so certain beneficial features are clear.

The T3 column is based on the same chemistry as the C18 column, with a few additional features designed to improve retention of polar compounds as well as retaining apolar species. These features include optimised pore size (improving function at higher aqueous mobile phases), bonded alkyl functionality (allowing more acidic solutions to be passed through with limited damage to the column) and optimized surface coverage and ligand density (specially treated silica base particles resulting in a uniquely bonded and end-capped sorbent that maximizes polar compound retention).⁵⁴ Another benefit to using the T3 over the C18 could be the use of the solid core particles, which may improve the overall efficiency of the column.⁵⁵

The T3 column proved to provide the best limit of detections and peak shapes for seven out of the eleven compounds, and so the LC-MS/MS method was modified to use the T3 column, using acetonitrile with 0.1% formic acid as the organic mobile phase and 0.1% aqueous formic acid as the aqueous mobile phase. The C18 column was still used with methanol with 0.1% formic acid as the organic mobile phase and 0.1% aqueous formic acid with 0.1% ammonium formate. A summary of which method is used for which antibiotic is given at the end of the chapter, in section 2.5.

2.3.5 Colistin b: Problems and Solution

Separation, ionisation and detection of colistin b proved to be inefficient using LC-MS/MS. This is consistent with literature reports where the only consistent and acceptable peak shapes were obtained through the use of ultra-high pressure liquid chromatography.⁵¹ Even when using UPLC as the separation technique, detection limits were shown to be 25.1 µg/L,⁵¹ well above those necessary to quantify trace levels in the environment (limits of ng/L)⁵⁶. However, in a proof-of-concept experiment to identify that colistin b was present in the solution despite not ionising *via* ESI, matrix-assisted laser desorption /ionisation (MALDI) was conducted. This is shown in **Figure 2.5**, with a high intensity singly charged peak (m/z 1154). This represents a potentially exciting development in the analysis of this biologically important antibiotic compound.

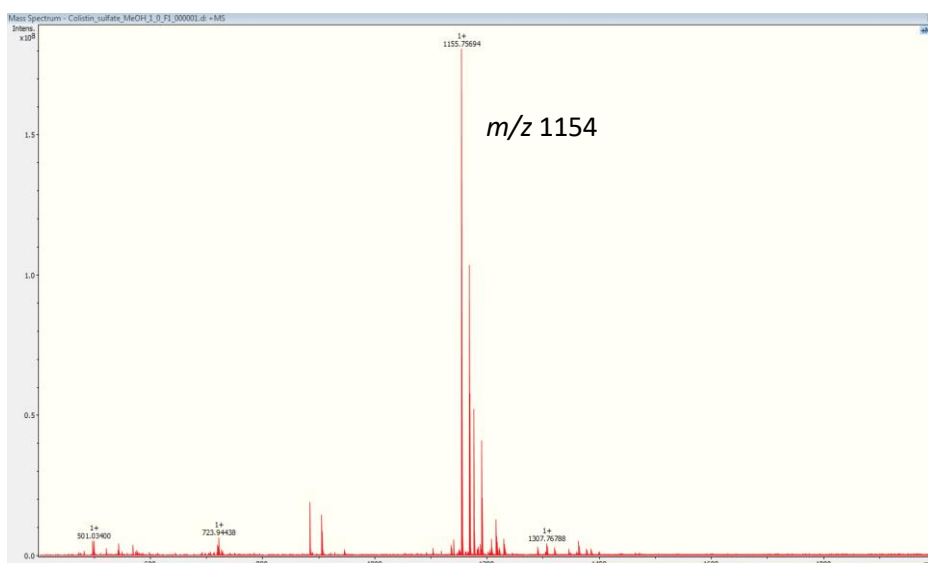


Figure 2.5: MALDI spectrum of colistin b, dissolved in methanol (concentration ~11 mg/L) and using 2,5-dihydroxybenzoic acid as the matrix.

2.4 Method Validation and Limits of Detection

2.4.1 Linearity

The definition of linearity is the measure of the extent to which any response is directly proportional to its cause.⁵⁷ In the case of this project, the area ratio of analyte to internal standard and the concentration of analyte are directly proportional. In some situations, the proportionality between the internal standard and the concentration of analyte may not be direct, and so the calibration may not be linear but a curve.

The calibrations for these analyses were made up of ten concentrations. Every calibration performed has an R^2 value of at least 0.99 (shown in **Table 2.2**) in at least one of the two LC methods used. Running the calibration standards every day a sample was run also ensures high repeatability.

2.4.2 Limits of Detection

To identify the limits of detection (LODs), the ion signals in the chromatograms must have a signal: noise of 3: 1. These LODs were identified from the ten-point calibration curves for each antibiotic. The limits of detection for the two LC-MS/MS methods using the C18 and the T3 columns can be found in **Table 2.2**. As it was important that the LODs were compared to the predicted no effect concentrations (PNEC), as reported by Bengtsson-Palme and Larsson (2016), these are also listed in **Table 2.2**.⁵⁸ The PNEC values show the level at which the antibiotics will have no effect on either the growth of the plant or on the bacterial resistance. The LODs must be below this value to ensure that the analysis can show if the PNEC has been reached.

Inconsistent retention time and qualifying ion detection for penicillin v at low concentrations results in a detection limit above the PNEC value. Additionally, an unexplained shift in retention time for metronidazole in samples analysed using the C18 column meant that the quantification

of this compound was only possible using the T3 method. The methods developed resulted in detection limits lower than the PNEC values for all other compounds.

Table 2.2: limit of detections for the two LC-MS methods, compared to the PNEC for each antibiotic.

Limit of Detection					
Antibiotic	Organic: methanol Aqueous: 0.1% aqueous formic acid with 0.1% ammonium formate		Organic: acetonitrile Aqueous: 0.1% aqueous formic acid		PNEC /ng L ⁻¹
	Column: C18	Linearity	Column: T3	Linearity	
Amoxicillin	-	-	10	>0.99	250
Cefalexin	-	-	10	>0.99	400
Ciprofloxacin	-	>0.87	1	>0.99	64
Clarithromycin	1	>0.99	4	>0.99	250
Erythromycin	4	>0.99	40	>0.99	1000
Metronidazole	4	>0.99	400	>0.99	125
Oxytetracycline	4000	-	40	>0.99	500
Penicillin v	-	-	100	>0.99	64
Tetracycline	2000	>0.98	4	>0.99	1000
Trimethoprim	40	>0.87	10	>0.99	500

2.4.3 Accuracy

Accuracy is defined as closeness to a true or desired value: here, that corresponds to how close the observed concentration is to the known concentration.⁵⁹ To measure accuracy, six different replicates of each sample were analysed, and ten different concentrations were used to construct each calibration curve.

Percentage recoveries of samples analysed on the LC-MS were calculated by analysing known concentrations (400 ng/L). The percentage recoveries are reported in **Table 2.3**. The closer the value is to 100%, the more accurate the analysis. For example, metronidazole has a percentage recovery of 105.1% in the leachate samples.

2.4.4 Precision

Precision refers to how close two or more measurements are to each other, regardless of whether those measurements are accurate or not.⁵⁹ This is demonstrated by the standard errors shown in **Table 2.3**. For example, metronidazole has standard errors of 3% and 4.9% in the pore water and leachate samples, suggesting high precision for detecting metronidazole.

Table 2.3: percentage recoveries of samples injected on the LC-MS

Antibiotics	Pore Water (%)	Leachate (%)
Amoxicillin	147.4 ± 20.9	54.5 ± 10.9
Cefalexin	108.1 ± 20.2	60.5 ± 13.8
Ciprofloxacin	98.1 ± 12.2	96.4 ± 32.3
Clarithromycin	120.8 ± 30.6	91.1 ± 8
Erythromycin	0 ± 0	64.5 ± 3.2
Metronidazole	108.3 ± 3	105.1 ± 4.9
Oxytetracycline	61.2 ± 5.2	66.7 ± 4.9
Penicillin v	90.4 ± 90.4	0 ± 0
Tetracycline	52 ± 4	62.7 ± 7.3
Trimethoprim	64.4 ± 5.6	106.5 ± 5.4

2.5 Summary

The best separation methods for each antibiotic can be found in **Table 2.4**.

Table 2.4: an overview of the method used for each antibiotic

Antibiotic	Mobile Phase A	Mobile Phase B	Column used
Cefalexin	0.1% aqueous formic acid	acetonitrile with 0.1% formic acid	T3
Penicillin v	0.1% aqueous formic acid	acetonitrile with 0.1% formic acid	T3
Amoxicillin	0.1% aqueous formic acid	acetonitrile with 0.1% formic acid	T3
Tetracycline	0.1% aqueous formic acid	acetonitrile with 0.1% formic acid	T3
Oxytetracycline	0.1% aqueous formic acid	acetonitrile with 0.1% formic acid	T3
Ciprofloxacin	0.1% aqueous formic acid	acetonitrile with 0.1% formic acid	T3
Trimethoprim	0.1% aqueous formic acid	acetonitrile with 0.1% formic acid	T3
Metronidazole	0.1% aqueous formic acid with 0.1% ammonium formate	methanol with 0.1% formic acid	C18
Erythromycin	0.1% aqueous formic acid with 0.1% ammonium formate	methanol with 0.1% formic acid	C18
Clarithromycin	0.1% aqueous formic acid with 0.1% ammonium formate	methanol with 0.1% formic acid	C18
Colistin b	-	-	-

A summary of the LC method can be found in **Table 2.5**, and the gradient used in **Table 2.6**.

Table 2.5: LC method parameters

Oven temperature (°C)	40
Spray voltage (V)	3500
Sheath gas	48
Aux gas	14
Sweep gas	2
Ion transfer tube temperature (°C)	346
Vaporiser temperature (°C)	379

Table 2.6: LC mobile phase gradient

Time (minutes)	Organic mobile phase (%)
0	0
3	0
13	100
16	100
16.2	0
21	0

Chapter 3 Targeted Analysis of Soil-Derived Samples

3.1 Introduction

In this chapter, the analysis of the samples collected from the pore water and the leachate are described. The antibiotics were quantified using the respective methods listed in **Table 2.4**, using LC-MS/MS (sections 1.4.2 and 1.4.3.2.1).

3.1.1 Pore Water and Leachate

Pore water is the term used to describe the interstitial water occupying pore spaces in bulk soil.⁶⁰ Chemicals in the pore water are thought to be readily bioavailable with many studies highlighting the fact that pore water concentrations, rather than bulk soil concentrations, correspond to the concentrations taken up by plants.^{13,61} The leachate is defined as the water that is collected from the outlet at the bottom of each mesocosm after it has flowed through the soil column. The leachate represents an important compartment to study as antibiotics measured represent those that with increased mobility may make their way into ground water in the environment. The pore water and leachate are shown in **Figure 3.1**.

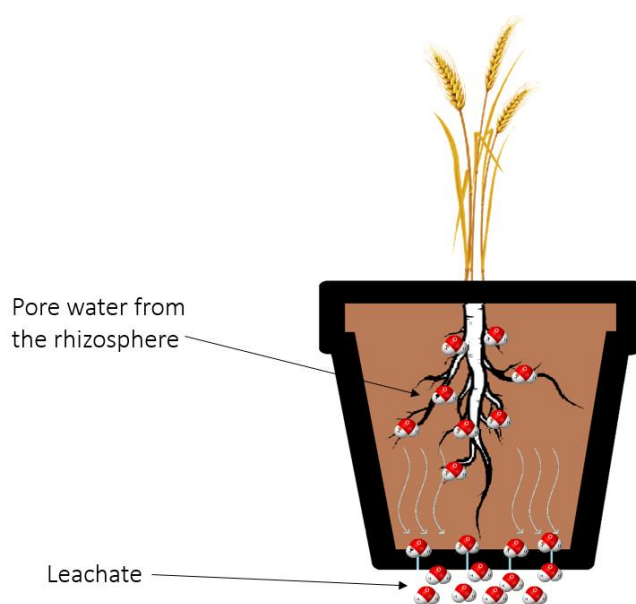


Figure 3.1: schematic of plant pot showing the pore water (labelled) and the leachate (labelled).

3.2 Method

3.2.1 Background

The field work associated with setting up and carrying out the mesocosm study, up to and including the harvesting of the plants, was conducted by J. Brett Sallach and colleagues in the Department of Environment and Geography.

The field experiment consisted of 30 different spring barley mesocosms, each planted with 74 seeds and using the same type of soil, based on recommendations from the UK Agricultural and Horticultural Development Board (Kenilworth, UK). Each mesocosm was irrigated with synthetic (i.e. manufactured) treated wastewater derived from the OECD (Organisation for Economic Co-operation and Development) guidelines for raw wastewater and spiked with a mixture of 11 antibiotics at four different concentrations. These included antibiotics from eight different classes: macrolides (erythromycin, clarithromycin), cephalosporins (cefalexin), penicillins (phenoxymethylpenicillin (penicillin v), amoxicillin), fluoroquinolones (ciprofloxacin), tetracyclines (tetracycline and oxytetracycline), sulphonamides (trimethoprim), nitroimidazoles (metronidazole) and polymyxins (colistin sulfate (colistin b)). Antibiotics are generally classified according to their chemical structure and antibiotics in a particular class have the same mode of action, for example antibiotics classified as tetracyclines act by inhibiting protein synthesis.⁶² The antibiotic compounds and concentrations used were determined using a modelling approach to predict concentrations in wastewater effluent, based upon 2016 UK prescription data made available by the National Health Service. The 11 antibiotics were included based on calculated risk index values⁶³ (calculated by dividing the PECs (**Equation 3.1**) by the PNECs⁵⁸) for the selection of antibiotic resistance. This approach considers both concentration and bioactivity of each compound.

The amount of each antibiotic likely to be found in treated wastewater, known as the predicted environmental concentration (PEC), was calculated by using the following algorithm (**Equation 3.1**) based on the method proposed by the European Medicines Agency for use in the environmental risk assessment of new active pharmaceutical ingredients for humans.⁶⁴

Equation 3.1

$$PEC = \frac{U \times (1 - F_{MET}) \times (1 - F_{REM})}{WW_{PROD}}$$

where U is the total mass prescribed annually in the UK; F_{MET} is the fraction metabolised by the human body; F_{REM} is the fraction removed by wastewater treatment works; and WW_{PROD} is the annual volume of wastewater produced in the UK.

Four antibiotic concentrations, with the same relative ratio of each compound, plus a control consisting of the synthetic wastewater and no antibiotics were used as treatments for each irrigation. The five treatments were control, $PEC \times 0.1$, PEC, $PEC \times 10$ and $PEC \times 100$, and these treatments were each applied to 6 mesocosms (environmental replicates). The concentrations for each antibiotic are shown in **Table 3.1**. During the 12-week growing season, soil samples were collected at five different times (**Table 3.2**), and leachate water samples were collected throughout. At the final sampling, plant material above and below ground was collected to measure physiological endpoints.

Table 3.1: concentrations of 11 antibiotics used to irrigate the barley mesocosms

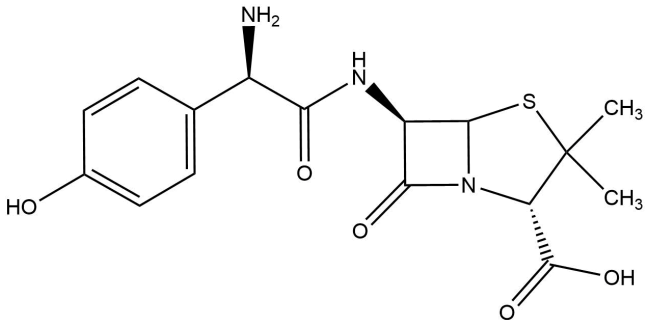
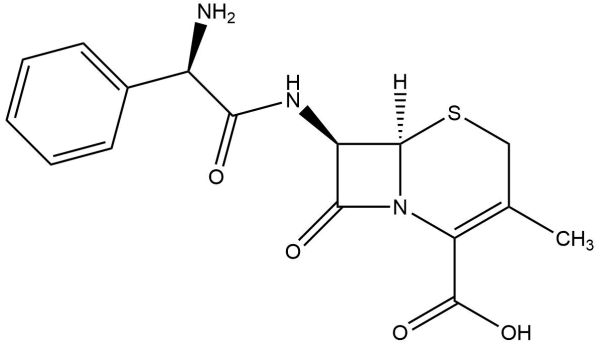
Antibiotics	PEC ($\mu\text{g/L}$)	PEC $\times 0.1$ ($\mu\text{g/L}$)	PEC $\times 10$ ($\mu\text{g/L}$)	PEC $\times 100$ ($\mu\text{g/L}$)
Metronidazole	2.50	0.25	25.04	250.40
Penicillin v	0.84	0.08	8.45	84.49
Ciprofloxacin	0.35	0.03	3.50	34.98
Trimethoprim	2.15	0.21	221.46	214.55
Oxytetracycline	1.68	0.17	16.85	168.49
Clarithromycin	0.59	0.06	5.90	58.96
Cefalexin	4.96	0.50	49.65	496.48
Erythromycin	0.87	0.09	8.74	87.37
Amoxicillin	0.18	0.02	1.81	18.07
Colistin b	0.81	0.08	8.09	80.89
Tetracycline	0.24	0.02	2.37	23.66

Table 3.2: time of sample collections, showing details of plant treatments

Sample Name	Time of growth /weeks	Total number of irrigations	Number of irrigations containing antibiotics
T ₋₁	0	0	0
T ₀	2	4	0
T ₁	2.09 (2 weeks and 16 hours)	5	1
T ₂	8	16	12
T ₃	14	28	24

The chemical properties of each antibiotic can be found in **Table 3.3**.

Table 3.3: chemical properties of each antibiotic

Compound	CAS number	Formula	Average MW	pKa	log P	Structure
Amoxicillin	26787-78-0	C ₁₆ H ₁₉ N ₃ O ₅ S	365.4	3.2 ^{65,66}	0.87	
Cefalexin	15686-71-2	C ₁₆ H ₁₇ N ₃ O ₄ S	347.39	3.45 ⁶⁷	0.65	

Ciprofloxacin

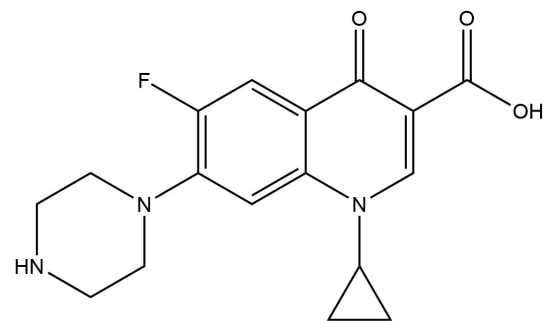
85721-33-1

$C_{17}H_{18}FN_3O_3$

331.34

6.09⁶⁸

0.28



Clarithromycin

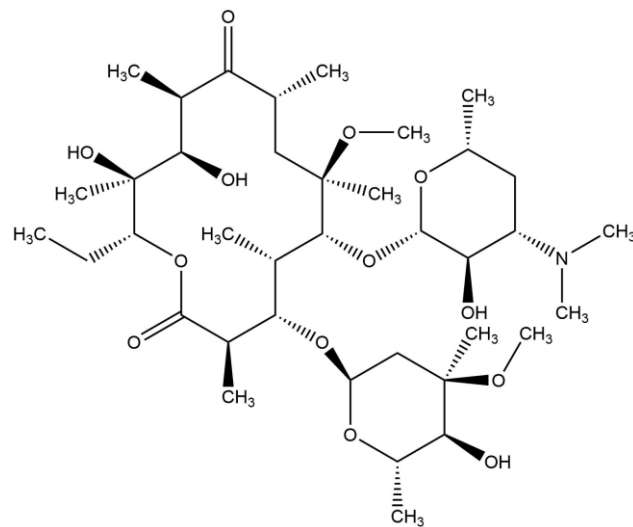
81103-11-9

$C_{38}H_{69}NO_{13}$

747.95

8.99⁶⁹

3.16



Erythromycin

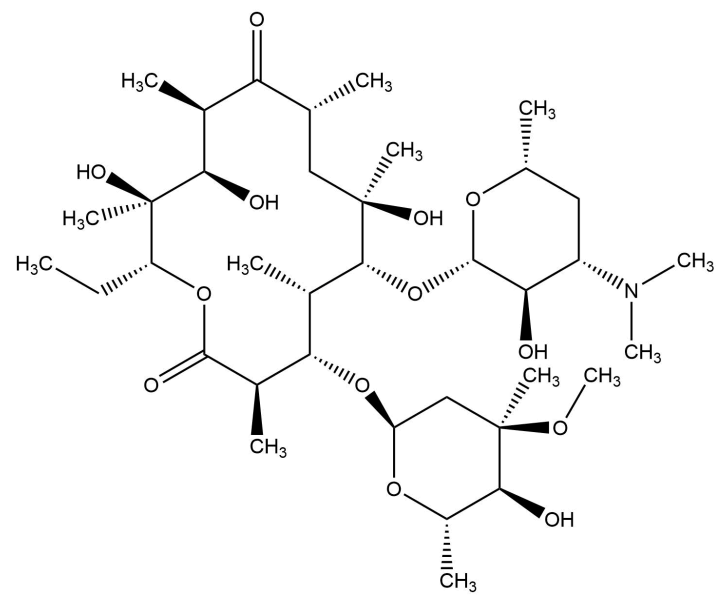
114-07-8

$C_{37}H_{67}NO_{13}$

733.93

8.88⁷⁰

3.06



Metronidazole

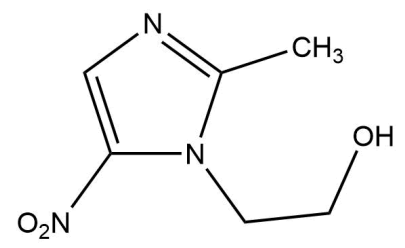
443-48-1

$C_6H_9N_3O_3$

171.15

2.57⁷¹

-0.02



Oxytetracycline

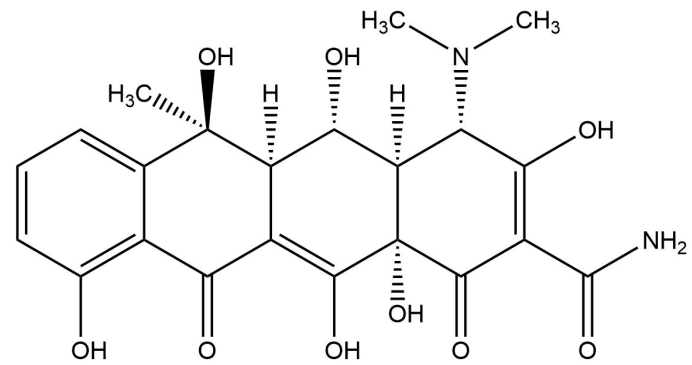
6153-64-6

$C_{22}H_{24}N_2O_9$

496.46

9.5⁷²

-0.9



Penicillin v

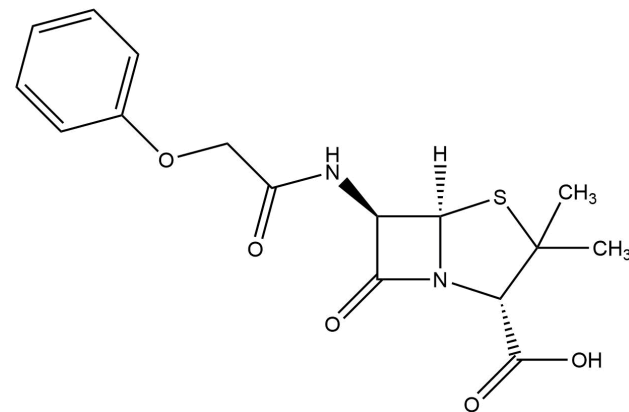
87-08-1

$C_{16}H_{18}N_2O_5S$

350.39

2.79⁷³

2.09



Tetracycline

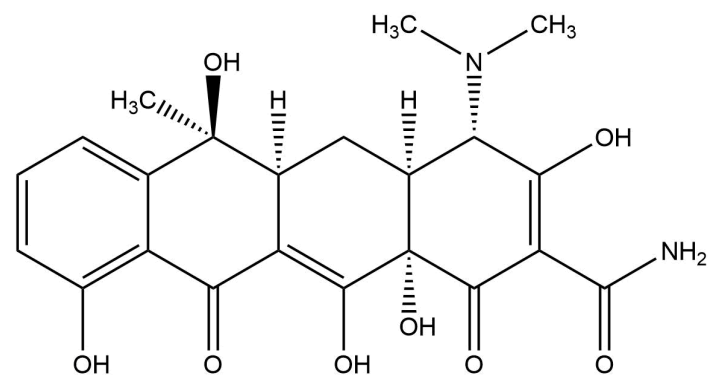
60-54-8

$C_{22}H_{24}N_2O_8$

444.43

3.3⁷⁴

-1.3



Trimethoprim

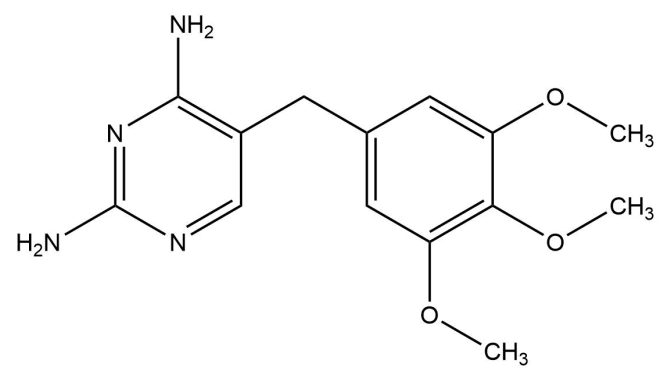
738-70-5

$C_{14}H_{18}N_4O_3$

290.32

7.12⁷⁵

0.91



3.2.2 Effect of pH

The pH of the soil in the mesocosms was measured throughout the study following a calcium chloride extraction, and it was found that throughout the growth period the pH decreased from 6.7 (at the start) to 6.1 (at the final sampling at the time of harvest). This change in pH would affect any antibiotics with a pKa between 6.1 and 6.8. The pKa values can be found in **Table 3.3**, but are summarised below in **Table 3.4**. None of the antibiotics have a pKa value between 6.1 and 6.7, but depending on how accurate the pH measurement is, ciprofloxacin could have been slightly affected (pKa 6.09). Therefore, the change in soil pH is unlikely to have had a major impact on this study.

However, the pH will impact the charge state of the antibiotics when in the soil environment, and as the clay particles have a positively charged surface, this will have an impact on the antibiotic retention. The formal charge of the antibiotic molecule at the pH range 6.1-6.7 is also listed in

Table 3.4.

Table 3.4: list of pKa values for antibiotics

Antibiotic	pKa	Cation/Anion at pH 6.1-6.7
Amoxicillin	3.2	Cation/Neutral ^{65,66}
Cefalexin	4.5	Cation/Neutral ⁶⁷
Ciprofloxacin	6.09	Cation/Zwitterion ⁷⁶
Clarithromycin	8.99	Neutral/Anion ⁶⁹
Erythromycin	8.88	Neutral/Anion ⁷⁰
Metronidazole	2.38	Cation/Neutral ⁷¹
Oxytetracycline	9.5	Neutral/Anion ⁷⁷
Penicillin v	2.79	Cation/Neutral ⁷³
Tetracycline	3.3	Neutral/Anion ⁷⁸
Trimethoprim	7.12	Neutral/Anion ⁷⁹

3.2.3 HPLC MS/MS analysis

The instrument used in this analysis was a Thermo Scientific™ TSQ Endura triple quadrupole tandem mass spectrometer, coupled to a Thermo Scientific Dionex UltiMate 3000 HPLC using ESI as the ionisation source.

3.2.3.1 Preparations of stock solutions

Standard solutions (1 mg/mL, made from the solid compound) of oxytetracycline, tetracycline, cefalexin, penicillin v and amoxicillin in 50: 50 (v:v) water: acetonitrile and stock solutions (1 mg/mL) of oxytetracycline, tetracycline, metronidazole, ciprofloxacin, trimethoprim, erythromycin and clarithromycin in methanol were diluted to a concentration of 5 ng/μL each, in a stock solution containing all ten antibiotics. Ten calibration concentrations (1, 4, 10, 40, 100, 400, 1,000, 2,000, 4,000 and 10,000 ng/L - **Figure 3.2**) at a 90: 10 aqueous: organic ratio were then made from this solution, and were analysed on the triple quadrupole LC-ESI-MS using the corresponding method for each antibiotic (**Table 2.4**).

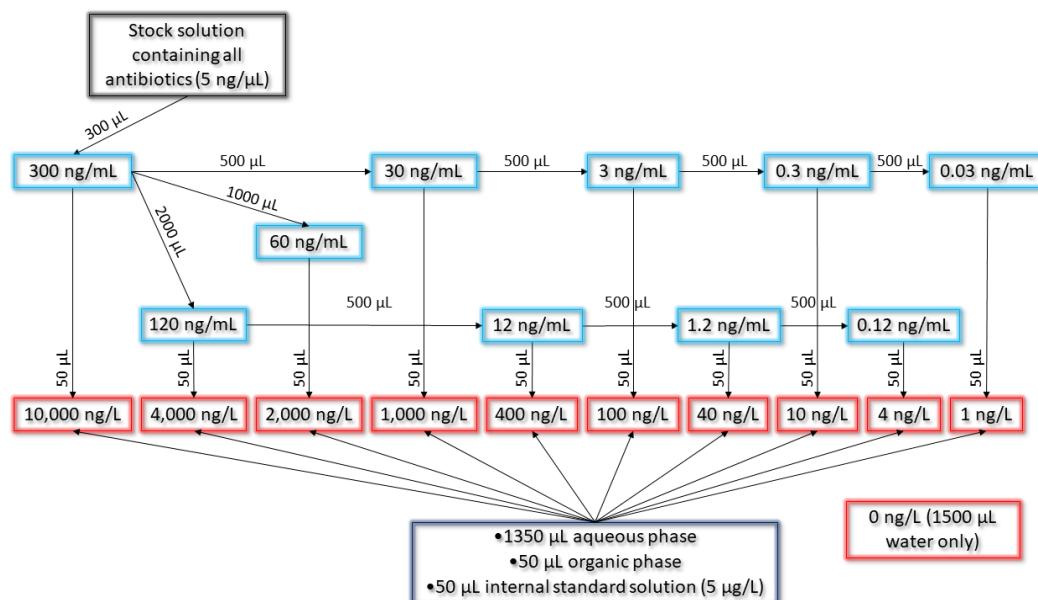


Figure 3.2: calibration standards (and blank) in red boxes. Arrows represent movement of solution from one vial to another, with the quantity to be transferred reported next to them. All light blue boxes were made up to 5 mL of 50: 50 (v:v) organic solvent: HPLC grade water.

3.2.3.2 *Internal Standards*

The internal standards used were ciprofloxacin-d8, trimethoprim-d9, metronidazole-d3, azithromycin-d3, amoxicillin-d4 and sulfamethoxazole-d4. These internal standards were required because of the matrix effects. Matrix effects are interferences with ionisation that can result in either the enhancement or suppression of signal in the mass spectrum. For example, trimethoprim spiked at 100 ng/L in HPLC grade water or spiked into extracted pore water from unexposed soils resulted in a 35% reduction in ion signal. This demonstrates the requirement for internal standards, as the matrix effects of the internal standards would react in the same way and therefore the ratio of analyte signal over internal standard signal would compensate for these reductions.⁸⁰

Two internal standard solutions were made, one for adding to the calibration solutions and one for adding to the samples (concentrations of 15 µg/L and 5 µg/L respectively). 24 µL of a solution containing all six internal standards dissolved in 50: 50 (v:v) acetonitrile: water (concentration 10 mg/L) was diluted into 5 mL 50: 50 acetonitrile: water (concentration 48 µg/L). From this, two solutions were made; the calibration spike was made by diluting 625 µL into 2 mL (concentration 15 µg/L), and the sample spike by diluting 625 µL into 6 mL (concentration 5 µg/L).

3.2.4 *Leachate Collection and Preparation*

Leachate samples were collected from mesocosms (see section 1.2) throughout the study. For each mesocosm, the total volume of leachate was measured and then a 10 mL aliquot was collected *via* syringe and filtered through a syringe filter (Whatman Puradisc, 0.7 µm pore size) into a 20 mL amber vial. They were stored at -20 °C.

3.2.5 Pore Water Extractions

Soil pore water was extracted from bulk soil samples taken at various sampling times throughout the field study following the method described in Carter et al, and stored for subsequent processing and analysis by the author.⁸¹ 20 mL syringes were loaded with compressed glass wool, before 20-40 g of bulk soil sample was added (depending on how wet the soil was). The packed syringe was then placed in a 50 mL centrifuge tube, with a specially modified lid designed to suspend the syringe in the tube during centrifugation. The samples were centrifuged at 1500 rpm for 40 min (2x20) min to collect pore water in the centrifuge tube. Water was removed and weighed after each 20 min cycle and the total pore water extracted was then combined, filtered through a Whatman Puradisc Syringe Filter (13 mm, 0.7 μm pore size) into an 8 mL amber vial, and stored at -20 °C.⁸¹ The volumes of pore water extracted are recorded in **Table A.1** in the appendix.

3.2.6 Analysis of Leachate and Pore Water Samples

In GC vials containing a glass 300 μL insert, 180 μL of each sample and 20 μL of the 5 $\mu\text{g/L}$ internal standard solution (see section 3.2.3.2) was pipetted and vortexed. This gave the same organic-aqueous ratio as the starting mobile phase. 10 μL aliquots of each sample were combined into a separate quality control (QC) vial, which was used to condition the column before the analyses, using 20 consecutive QC injections.⁸² Sample blanks were also used after the calibration, after every 10 samples, and prior to every control samples, in attempt to prevent any carryover. In addition to the blank sample after every 10 samples, a mid-range calibration (400 ng/L) was included to monitor performance throughout the analysis.

3.3 Results

The concentrations of antibiotics in the leachate and pore water samples were measured and are reported below. Each concentration shown is the averaged concentration from six experimental replicates for each treatment. The “control” subset represents the samples collected from mesocosms where the plants were only irrigated with synthetic wastewater (no antibiotics).

3.3.1 Leachate

The concentrations of the antibiotics detected in the leachate samples are reported in **Figure 3.3**.

Amoxicillin, penicillin v, tetracycline, oxytetracycline and ciprofloxacin were not detected.

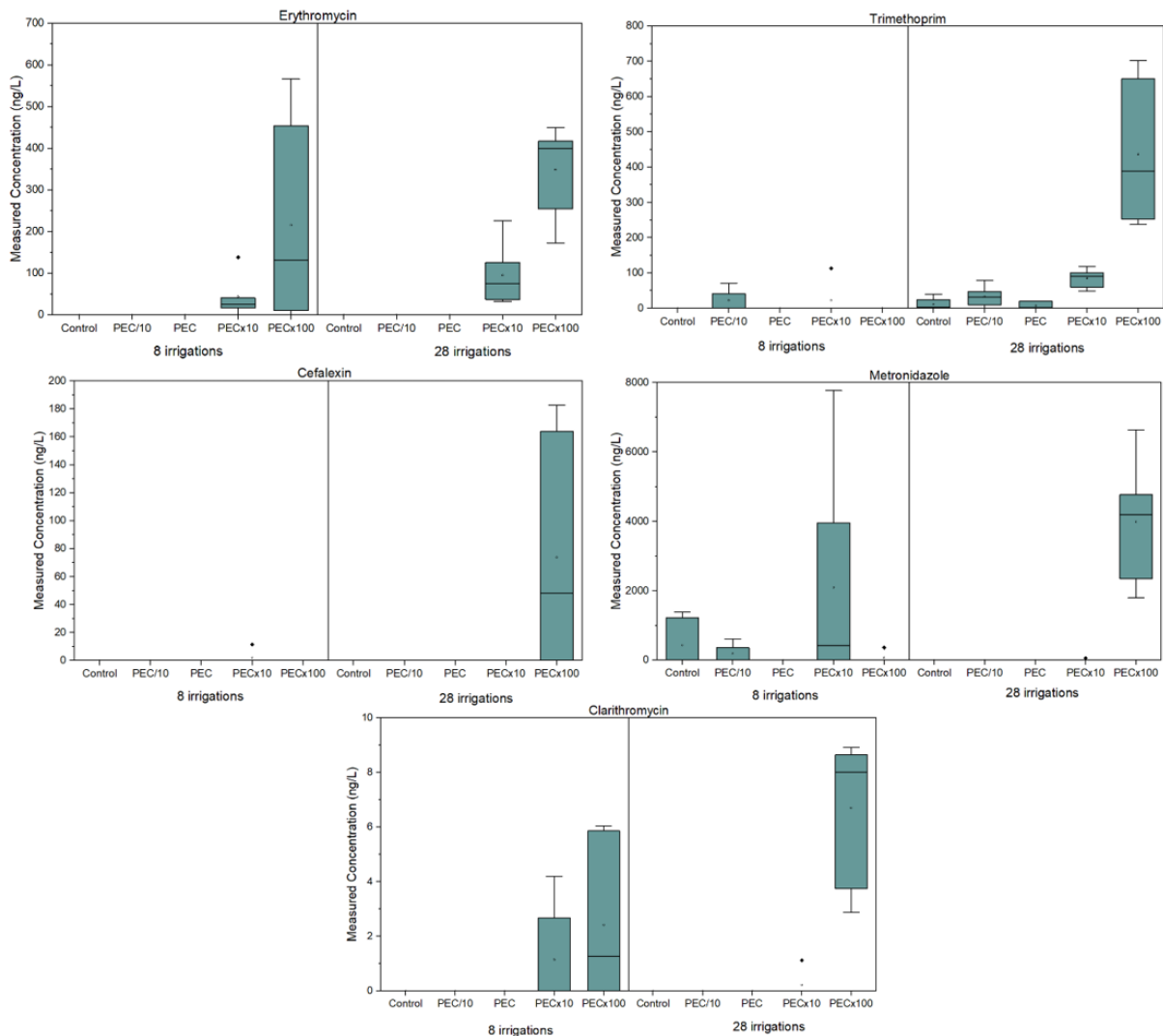


Figure 3.3: summary of antibiotic concentrations found in the leachate samples. Amoxicillin, penicillin v, tetracycline, oxytetracycline and ciprofloxacin were not detected.

Cefalexin was only detected in the PEC×100 samples after 28 irrigations, and not in any of the others.

Clarithromycin and erythromycin were both detected in the PEC×10 and the PEC×100 samples, in the samples taken after 8 irrigations and 28 irrigations. The concentration of both clarithromycin and erythromycin in the PEC×100 samples was greater than that in the PEC×10 samples. There was no increase in concentration observed when comparing the samples after 28 irrigations to the samples after only 8 irrigations.

Trimethoprim was detected in all the samples, including the control samples (the samples collected from plants with no exposure to any antibiotics). The detection of trimethoprim in the control samples is likely to be due to carryover, as it was also detected in the blanks. Comparing the peak areas of the trimethoprim detected in the blanks to those in the calibration curve, would suggest that the concentration of the carryover is between 10-40 ng/L (peak areas can be found in **Figures A.1** and **A.2** in the appendix, while the peak areas of trimethoprim in the control samples are listed in **Table A.2**, again in appendix). However, there was an increase in concentration observed in the samples taken after 28 irrigations compared to the samples taken after 8 irrigations, and a general increase was seen across the different concentrations used to irrigate the plants. This increase in concentration exceeds what can be seen in the control samples, and it is therefore likely that the concentration of trimethoprim is indeed increasing. The exceptions to this are where the trimethoprim in the PEC×100 samples was not detected after 8 irrigations, and the concentration of the trimethoprim in the PEC×0.1 samples was of a greater concentration than that in the PEC samples. There was also no trimethoprim detected in the PEC sample after 28 irrigations.

Metronidazole was detected in the PEC×100 and the PEC×10 samples collected after 28 irrigations. It was also detected in the PEC×100, PEC×10 and the PEC×0.1 samples collected after 8 irrigations. There was no increase in the concentration of metronidazole detected in the samples collected after 28 irrigations compared to the samples collected after 8 irrigations, with the exception of

PEC×100. Instead, the concentration is higher in the samples collected after 8 irrigations for PEC×10 and PEC×0.1.

There is no trend found in the concentration of the samples collected after 8 irrigations: in fact, the concentration detected in the PEC×100 samples was of a lower value than that in the PEC×10 samples, and metronidazole was not detected in the PEC samples but was detected in the PEC×0.1 samples.

3.3.2 Pore Water

The concentrations of antibiotics found in the pore water samples are reported in **Figure 3.4**.

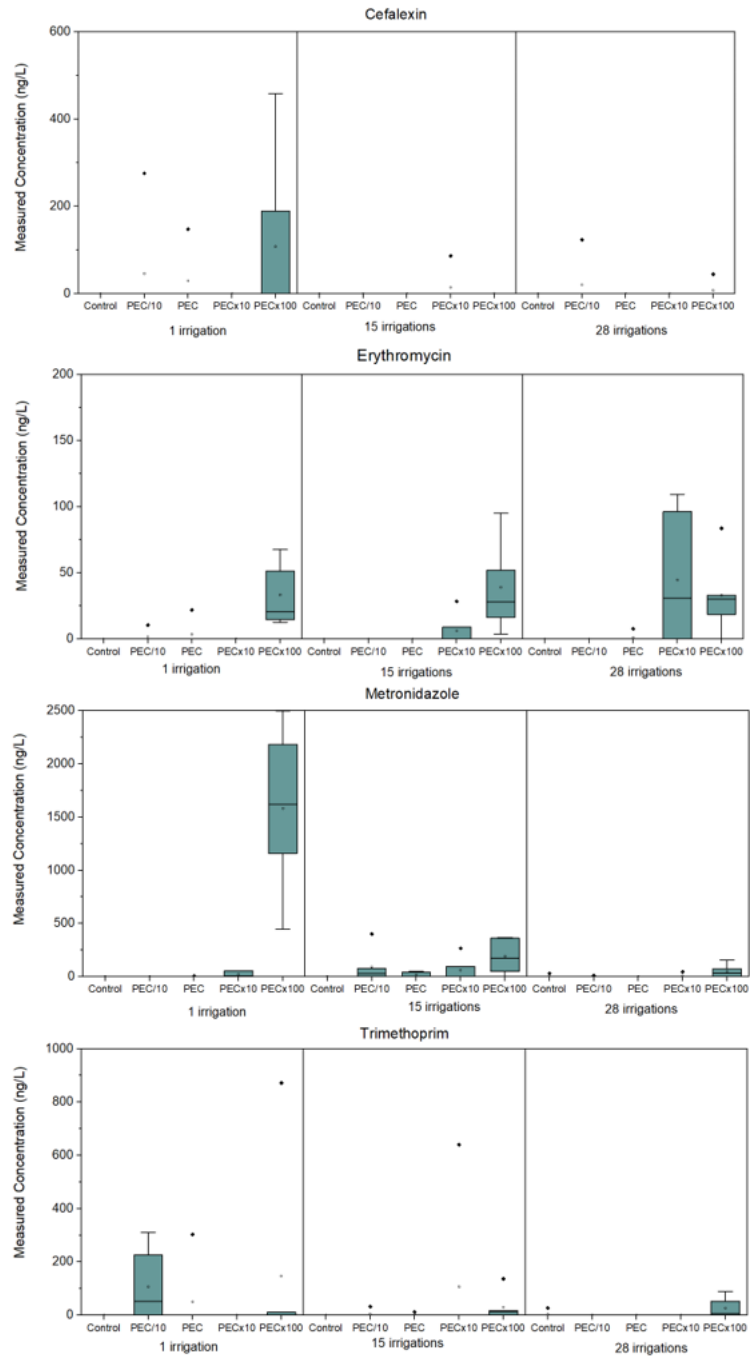


Figure 3.4: overview of antibiotic concentrations found in the pore water samples.

Tetracycline, oxytetracycline, penicillin v, cefalexin, clarithromycin, amoxicillin and ciprofloxacin were not detected.

The samples collected after 1 irrigation were collected after only 16 hours, in comparison to the samples collected after 15 and 28 irrigations which were collected after 48 hours.

Cefalexin was detected in the PEC and the PEC×100 samples collected after only 1 irrigation and was not detected in any of the other samples.

Trimethoprim was detected in the PEC×100 samples taken after 1, 15 and 28 irrigations with the concentration detected increasing as the number of irrigations increased. Trimethoprim was also detected in the PEC×0.1 sample taken after 1 irrigation, and the concentration here was greater than any of the PEC×100 samples.

Metronidazole was detected in the PEC×100 samples, the PEC×10 samples, the PEC×0.1 and the control samples that were collected after 28 irrigations. In the samples collected after 15 irrigations, metronidazole was detected in all samples excluding the controls, and in the samples collected after 1 irrigation it was only detected in the PEC samples, the PEC×10 samples and the PEC×100 samples. Metronidazole appeared to have the least linearity across the samples, as when metronidazole was detected in the PEC×0.1 samples the concentration was greater than the concentration detected in the PEC samples. In addition to this, there was a lower concentration of metronidazole detected in the PEC×100 samples than the PEC×10 samples in those collected after 28 irrigations, as well as being detected in greater concentrations in the PEC samples taken after only 1 irrigation compared to the PEC×10 samples. There was a decrease in concentration of metronidazole as the number of irrigations increased.

Erythromycin was detected in the PEC×10 and PEC×100 samples taken after 15 irrigations and 28 irrigations. It was also detected in the PEC samples taken after 28 irrigations. In the samples collected after only 1 irrigation, erythromycin was detected in the PEC×0.1, PEC and PEC×100 samples. There is no general increase in the concentration detected as the number of irrigations increased. In most cases (the samples after 1 irrigation being the exception where erythromycin was not detected in the PEC×10 samples) the concentration increased as the exposure to the

antibiotics increased (for example, PECx100 samples contained more erythromycin than the PECx10 samples).

3.3.3 Comparing concentrations detected to PNEC values

The pore water and leachate antibiotic concentrations were then compared to the PNEC values, shown in **Table 3.5** and **Table 3.6** respectively. The PNEC values are those at which the antibiotics can select for antimicrobial resistance in the environment and are therefore important to identify if an antibiotic is a potential threat.⁵⁸

Table 3.5: comparing averaged pore water concentrations to the PNEC values.

Treatment:	PECx0.1 (ng/L)			PEC (ng/L)			PECx10 (ng/L)			PECx100 (ng/L)			PNEC
	1	15	28	1	15	28	1	15	28	1	15	28	(ng/L)
Metronidazole	0	89	1	1805	18	0	20	60	70	4681	254	48	125
Trimethoprim	107	0	0	0	0	0	0	0	0	2	8	26	500
Cefalexin	0	0	0	29	0	0	0	0	0	38	0	0	400
Erythromycin	2	0	0	4	0	1	0	6	45	156	70	64	1000

Table 3.6: comparing averaged leachate concentrations to the PNEC values.

Treatment:	PEC×0.1		PEC		PEC×10		PEC×100		PNEC
	(ng/L)		(ng/L)		(ng/L)		(ng/L)		
Number of irrigations:	8	28	8	28	8	28	8	28	
Cefalexin	0	0	0	0	0	0	0	74	400
Clarithromycin	0	0	0	0	1	0	2	7	250
Erythromycin	0	0	0	0	44	95	216	349	1000
Trimethoprim	22	33	0	7	23	85	0	436	500
Metronidazole	193	0	0	0	2097	13	72	3986	125

The only antibiotic found to exceed the PNEC value at all was metronidazole. The concentration of metronidazole detected in the PEC×0.1 and the PEC×10 leachate samples taken after 8 irrigations and the PEC×100 samples taken after 28 irrigations were both greater than the PNEC value. In the pore water results, the concentration of metronidazole exceeds the PNEC value in both the PEC and the PEC×100 samples taken after 1 irrigation.

3.4 *Effect on Plants: Root Density*

All calculations performed and conclusions drawn in this section were the work of Dr J Brett Sallach and are included in order to provide contextual information in which to view the data generated by the candidate.

3.4.1 *Methods*

At the final harvest, two 5.8 cm diameter sediment cores were collected from each mesocosm for the separation of root material and determination of root density. The two cores from each mesocosm were combined, weighed, and the roots were separated by passing the bulk soil through a 1 mm sieve. Root material captured on the sieve was separated from other large particles and rhizosphere soil was removed by washing. Root tissues were stored in brown paper bags and dried in a conventional oven at 60°C for 72 hours. Root bulk density was calculated as the dry mass of root material (g) divided by the mass of bulk soil collected in each mesocosm.

3.4.2 Results

Once the roots had been dried and weighed, the root density of the plant was calculated. As the concentration of antibiotics used to irrigate the mesocosms increased, the density of roots also increased (**Figure 3.5**). Germination of the barley plants was shown to be impacted by antibiotic exposure with lower germination rates associated with increasing antibiotic concentrations (data from J. Brett Sallach not shown).

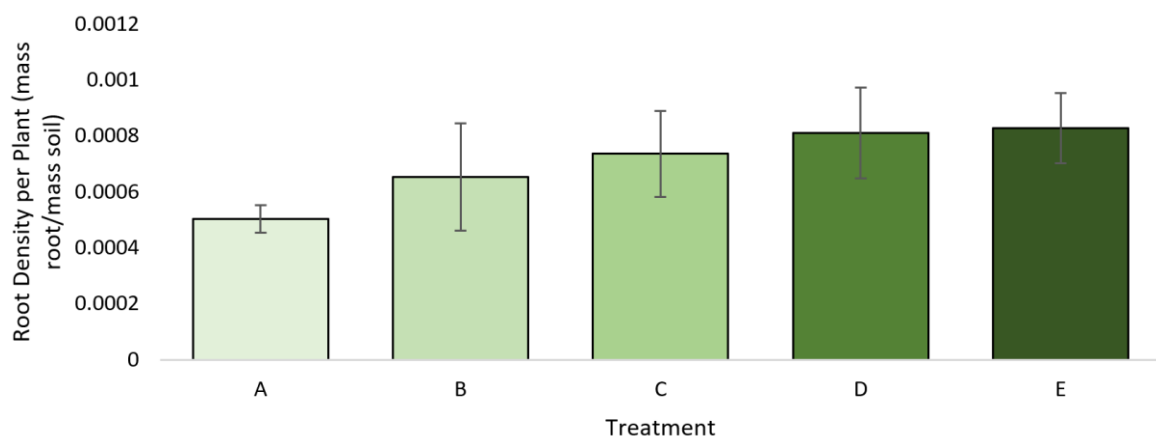


Figure 3.5: Root density in barley mesocosms from treatments A (control), B (PEC×0.1), C (PEC), D (PEC×10), E (PEC×100). Bars represent standard error.

3.5 Discussion

3.5.1 Comparing Antibiotics in Pore Water and Leachate Samples

The antibiotics belonging to the classes tetracyclines (tetracycline and oxytetracycline), β -lactams (cefalexin, amoxicillin and penicillin v) and quinolones (ciprofloxacin) were not detected (or detected in very low quantities) in either the pore water or leachate samples. This would suggest that the structure of the antibiotic has a large effect on the transport of the antibiotic throughout the soil-plant system: for instance, it was already known that the tetracyclines have a large soil adsorption coefficient (due to chelating to metal ions in the soil)⁸³ and are susceptible to photolysis resulting in the antibiotics degrading.⁸⁴ Both these factors could account for the inability to detect tetracyclines in the pore water and leachate samples. Antibiotics in the β -lactam class all contain a β -lactam ring, which is susceptible to hydrolysis and therefore could lead to degradation in the pore water and leachate. This could explain the inability to detect these antibiotics. The reasons for the inability to detect ciprofloxacin could be due to either soil adsorption, microbial degradation or abiotic degradation. Despite the remaining antibiotics all being detected to some extent, the total mass of the antibiotics used to irrigate the mesocosms has not been fully accounted for and rationalised. Therefore, the reasons listed above also apply to the remaining antibiotics. This idea has been further explored in **Chapter 4**.

3.5.1.1 Leachate

One major assumption that was made in this study was that the soil was homogeneous and that the flow of water is consistently permeating through the mesocosm. However, there can be several exceptions to this. If pores exist, or develop over time, a preferential flow-path with less soil-antibiotic interactions would develop and cause the concentrations detected in the leachate to be higher.

Given that the leachate samples were collected throughout the study, the concentrations in those samples were only expected to increase over time was if all of the sorption sites in the soil were taken. This was not expected to happen, as the concentrations used in the field study were low. The antibiotics detected in the leachate might also be linked to the log P (also known as log K_{ow}) values. These can be found listed in **Table 3.3**. The lower the value of log P, the more likely the antibiotic is to be found in the leachate. However, this does not appear to be the case, as for example, erythromycin and clarithromycin have log P values of 3.06 and 3.16 respectively, and these two are found in the leachate samples. The values of log P were plotted against the average concentrations measured for each antibiotic found in the leachate samples collected after 28 irrigations (**Figure 3.6**).

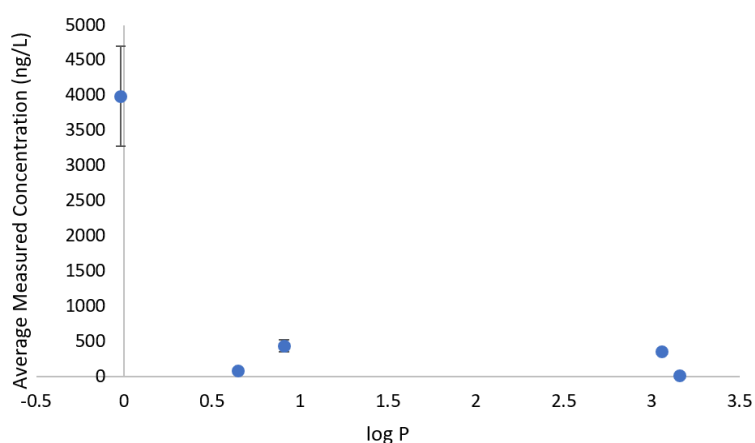


Figure 3.6: scattergraph demonstrating lack of correlation between log P and the average measured concentration detected in the leachate samples collected after 28 irrigations.

Cefalexin was only detected in the PEC \times 100 samples taken after 28 irrigations. This could be explained by the cefalexin only appearing in the leachate after the samples for 8 irrigations were collected, possibly due to the cefalexin moving more slowly through the soil-plant system and taking longer than other components to reach the leachate.

Trimethoprim also showed an increase in the concentration after 28 irrigations. This could be for similar reasons to those mentioned for cefalexin; however, during the analysis of trimethoprim it

was noticed that there was carryover of trimethoprim between injections (e.g. trimethoprim was detected in the control samples when these had never been exposed to any concentration of antibiotics). The trimethoprim increases in concentration in leachate as the exposure of the system to the antibiotics increases, excepting the concentrations detected in the samples collected after 8 irrigations.

Neither the clarithromycin, erythromycin nor metronidazole showed an increase in concentration after 28 irrigations. Clarithromycin and erythromycin showed similar trends, only being detected in the PECx10 and PECx100 samples, with the concentration detected in the PECx100 samples being greater than that in the PECx10 samples. This is due to the increased exposure to antibiotics in the PECx100 samples. The lack of detection in the other samples is likely due to the limit of detection not being low enough. This same trend is observed with metronidazole after 28 irrigations.

For both metronidazole and trimethoprim, the measured concentrations detected in the samples collected after 8 irrigations demonstrate no trend (no increase across the four different exposures).

3.5.1.2 Pore Water

Over time, there appears to be no build up in the pore water of any of the antibiotics detected but trimethoprim. In contrast, the concentrations appear to be decreasing. This was unexpected and might suggest that the antibiotics either move into the leachate or are degraded within the mesocosms at a greater rate than they were added *via* irrigation. Alternatively, the antibiotics could be sorbed irreversibly to the soil over time. Analysis of the bulk soil is necessary to determine this.

As cefalexin was only detected after 1 irrigation, it is likely that it has either degraded or moved out of the pore water. Given that it was detected in the leachate after 28 irrigations, this may suggest that it is mobile in the soil system and perhaps more readily degraded in the sample pore water environment.

Trimethoprim appears to build up in the pore water as the number of irrigations increased, although it is only detected in the PEC×100 samples. The concentration of trimethoprim detected in the PEC×0.1 samples after 1 irrigation appears to be anomalous, due to the lack of trimethoprim detected in the other samples. One potential cause for this anomalous result could be due to non-homogeneity in the environmental samples.

The concentrations of metronidazole detected after 1 irrigation appears to be random: there is no correlation with antibiotic exposure. This is also the case after 15 irrigations and 28 irrigations, and so there is no conclusive result. It could be that metronidazole is either being degraded, moving into the leachate, or binding irreversibly to the soil over time. Another possibility is an analytical error, such as carryover. However, carryover was not an issue for metronidazole prior to the analysis of the samples and so this is unlikely.

The inconsistency observed in the erythromycin concentrations detected in the pore water could be due to non-homogeneous flow. This will have the greatest impact after only 1 irrigation event, and there would be much less time for any sorption equilibrium to occur.

3.5.1.3 Comparing concentrations detected in pore water and leachate to PNEC values

The only antibiotic that exceeded the PNEC value in the leachate or pore water was metronidazole. This would suggest that metronidazole is the antibiotic presenting the most risk to the environment. The samples in which the PNEC value was exceeded in were the PEC, PEC×10 and the PEC×100 samples. This indicates that at environmentally relevant concentrations (PEC), as well as the treatments that exceed PEC, the bioavailable concentration of metronidazole may exceed those required to provide selective pressure for the proliferation of antibiotic resistance.

3.5.2 Partitioning of Antibiotics in the Soil System

Partitioning of the antibiotics between the leachate and pore water samples can be found in **Table 3.7**. This is only calculated for the highest treatment. The table shows the ratio of the antibiotics detected in the samples compared to the total amount of antibiotics applied to each mesocosm. The ratios of each individual replicate (numbered 1-6) are reported, as well as the average of these replicates. These were calculated using the following equations (**Equation 3.2, Equation 3.3, Equation 3.4 and Equation 3.5**):

$$\text{Equation 3.2} \quad \text{concentration}_{\text{sample}} \times \text{volume}_{\text{sample}} = \text{mass}_{\text{sample}}$$

$$\text{Equation 3.3} \quad \text{mass}_{\text{sample}} \times \frac{\text{volume}_{\text{sample}}}{\text{volume}_{\text{total}}} = \text{mass}_{\text{detected}}$$

$$\text{Equation 3.4} \quad \text{no. irrigations} \times \text{mass}_{\text{applied}} = \text{mass}_{\text{total applied}}$$

$$\text{Equation 3.5} \quad \text{Ratio (\%)} \text{ of antibiotics} = \frac{\text{mass}_{\text{detected}}}{\text{mass}_{\text{applied}}} \times 100\%$$

Table 3.7: percentage of antibiotics found in the pore water and leachate samples.

		Percentage detected relative to mass applied to mesocosms (%)				
		Metronidazole	Clarithromycin	Erythromycin	Trimethoprim	Cefalexin
Pore Water	1	0.15	0.00	-	0.13	0.00
	2	0.09	0.00	0.14	0.00	0.00
	3	0.24	0.00	0.38	0.03	0.00
	4	0.00	0.00	0.07	0.00	0.00
	5	0.00	0.00	0.13	0.16	-
	6	0.00	0.00	0.00	0.00	0.00
Leachate	1	11.51	0.00	3.18	0.00	0.04
	2	13.41	3.85	2.61	1.78	0.19
	3	22.27	8.89	6.03	0.00	0.00
	4	26.11	9.68	6.56	0.04	0.45
	5	0.00	0.00	3.20	8.31	0.00
	6	0.00	0.00	0.00	1.24	0.00
Total	1	11.67	0.00	3.18	0.13	0.04
	2	13.50	3.85	2.75	1.78	0.19
	3	22.51	8.89	6.40	0.03	0.00
	4	26.11	9.68	6.64	0.04	0.45
	5	0.00	0.00	3.33	8.47	0.00
	6	0.00	0.00	0.00	1.24	0.00
Pore Water (Averaged)		0.08	0.00	0.14	0.05	0.00
Leachate (Averaged)		12.22	3.74	3.60	1.89	0.11
Total of Averaged		12.30	3.74	3.72	1.94	0.11

The highest percentages were found in the leachate samples, with only very low percentages (<0.2%) of applied antibiotics found in the pore water. Even in the leachate samples, the highest averaged percentage of antibiotics able to be accounted for is 12.2%. This suggests that the antibiotics are likely to be located elsewhere in the plant-soil system or have been either biotically/abiotically degraded. **Chapter 4** explores the possibility of abiotic degradation (*via* either hydrolysis or photolysis) of the antibiotics.

3.5.3 *Effect on Plants*

The reason for the increase in root density as the antibiotic exposure increases is unclear. It is difficult to determine if the increase in root density is a plant response to antibiotic exposure or if increases in root density per plant might simply be due to the increase in space available for each plant (increased space due to the impact of the antibiotics on seed germination, resulting in fewer plants in each mesocosm).^{85,86}

3.6 *Conclusion*

One major conclusion to draw from these results is that the risk of bioavailable antibiotic concentrations exceeding those required for selection of antimicrobial resistance in the agricultural environment is, for all but one of the antibiotics, very low. For metronidazole, however, the concentrations detected in the PEC and PEC×100 pore water samples was found to be greater than the PNEC value. In the leachate, the concentration only exceeded the PNEC value in the PEC×10 and PEC×100 samples. This suggests that the level of metronidazole currently expected in the treated wastewater effluent in the UK could already be selecting for antimicrobial resistance if used for irrigation.

Chapter 4 Transformation of Antibiotics *via* Hydrolysis and

Photolysis

4.1 Introduction

In **Chapter 3**, the amounts of antibiotics in soil pore water and mesocosm leachate were measured. The results showed that only a small portion of the applied antibiotic could be accounted for in these fractions. This also suggests that degradation, either biotic or abiotic, plays a significant role in the fate of antibiotics in the soil-plant system. This is important since the effects of the degradants of the antibiotics on the environment are largely unknown.⁸⁷

While a significant amount of research has been conducted to determine the effect of antibiotics on the environment most of this has focused on study of the parent compounds. However, for some antibiotics, they may degrade prior to reaching the agricultural system, which would then be exposed to their degradants. Little is known about the fate and bioactivity of antibiotics⁸⁸, but other pharmaceuticals, such as fentanyl, have been shown to degrade into significantly more toxic degradants,⁸⁹ which would suggest that studying the fate of the antibiotics would be worth looking into. Other research suggests that photodegradation of pharmaceuticals could be a major part of the natural elimination process of those pharmaceuticals.⁹⁰

4.1.1 Degradation by UV Photolysis

UV photolysis (as demonstrated in this study) involves organic compounds absorbing photons emitted by UV light, resulting in bonds being broken.^{91,92} UV light encompasses many different wavelengths (100-400 nm) and as a result the photons that are emitted have different amounts of energy that are inversely proportional to the wavelength. Photon energy is given by using **Equation 4.1**.

$$\text{Equation 4.1} \quad \text{Photon Energy} = \frac{hc}{\lambda}$$

where h = Planck's constant (6.63×10^{-34} Js) c = speed of light in a vacuum (3×10^8 m/s), and λ = wavelength (m).

To understand how bonds are broken apart *via* photolysis, molecular orbitals (MOs) must be taken into consideration. **Figure 4.1** shows a general molecular orbital diagram, illustrating a series of MOs for a prototype molecule.

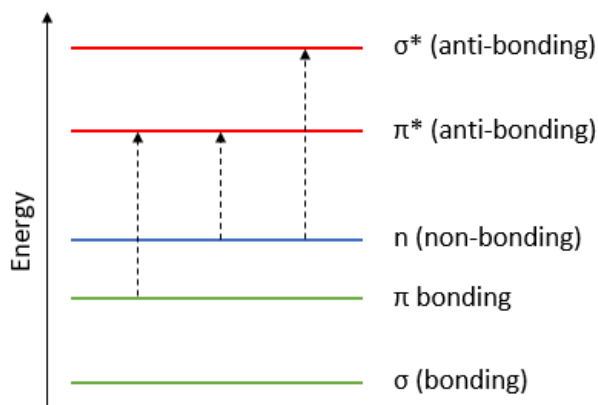


Figure 4.1: Conventional molecular orbital energy diagram. Dotted arrows represent the energy transitions electrons do when excited with wavelengths of 200-400 nm.

When a compound is exposed to UV radiation, light energy is absorbed by the various MOs. The energy is used to excite an electron from a lower energy orbital (bonding/non-bonding orbitals) to a higher energy orbital (anti-bonding orbitals). Each excitation takes energy; the larger the jump (e.g. σ bonding orbital \rightarrow σ anti-bonding orbital), the more energy required. Every wavelength of light corresponds to a different amount of energy (**Equation 4.1**). Thus, different wavelengths can cause different electrons to be excited. The electron excitations that are caused by wavelengths greater than 200 nm are typically from π bonding orbitals to π anti-bonding orbitals; non-bonding orbitals to π anti-bonding orbitals; and non-bonding orbitals to σ anti-bonding orbitals (**Figure 4.1**). Therefore, to be able to absorb UV light, a compound must contain either π bonds or atoms with non-bonding orbitals (i.e. a lone pair on an atom such as oxygen). Such compounds are referred to as chromophores.

When the electrons have been excited to the anti-bonding orbitals, bond rupture can occur. As different wavelengths can cause different bonds to break, when examining the photolysis of a compound it is best to consider a wide range of wavelengths. Using laser-interfaced mass spectrometry, the detection of photofragments at different photon energies can be monitored, allowing for the direct observation of possible degradation pathways a molecule can follow when subjected to UV light. For example, the photofragments of oxybenzone absorb in the UVA and UVB ranges (discussed further in section 4.3.3).⁹³

4.1.2 Degradation by Hydrolysis

Hydrolysis is any chemical reaction where a chemical bond is ruptured by a water molecule.

Typically, the water molecule acts as the nucleophile (electron donor in this reaction).⁹⁴ An example of hydrolysis is shown in **Figure 4.2**, demonstrating hydrolysis of a β -lactam ring^{95,96} (the key structural component of penicillin v).

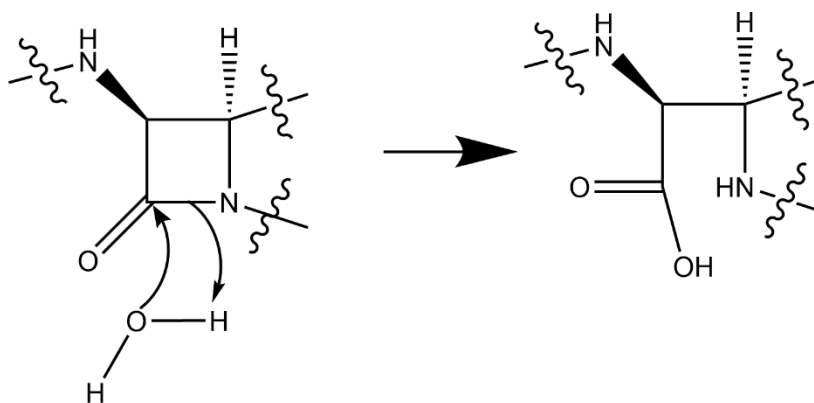


Figure 4.2: hydrolysis of the β -lactam ring in penicillin v

4.1.3 Aims

The purpose of the experiments presented in this chapter was to determine how rapidly the antibiotics degrade in sunlight in water (photolysis and hydrolysis, solution phase), in the dark in water (hydrolysis only), and by photofragmentation (photolysis only, gas phase) and to identify major degradation products. Three antibiotics were selected from the 11 studied in this project: penicillin v, metronidazole and oxytetracycline. These three were selected to offer a general cross section of antibiotic structures. The analytical methods used to analyse the antibiotics in this chapter were FT-ICR, the Orbitrap Fusion and laser interfaced mass spectrometry (described in detail in sections 1.4.3.3, 1.4.3.4 and 1.4.3.5).

4.2 Method

The instrument used in the untargeted analysis was a Bruker Daltonics solariX XR FTMS, a very high-performance hybrid Qh-FT-ICR instrument. Due to this being a very time intensive study, only three antibiotics were analysed: penicillin v, oxytetracycline and metronidazole. These three antibiotics are all from different classes, and so were chosen as a representative cross section of the antibiotics studied in this project.

4.2.1 Hydrolysis in the light

Solutions of 50 mg/L were prepared of penicillin v, metronidazole and oxytetracycline, in LCMS grade water. 3 mL was pipetted into a quartz cuvette and placed into a photolysis cell in which the cuvette is surrounded by four LEDs all transmitting light of the wavelength 365 nm (UV-A).

Aliquots of the solution were taken over the course of eight hours exposure to UV light, and untargeted analysis of the components carried out by direct infusion on an FT-ICR mass spectrometer. Eight hours was chosen as this experiment required constant monitoring, and as such could not run overnight. Due to time constraints of this project, no repeats were conducted.

4.2.2 Hydrolysis in the dark

Solutions of 50 mg/L were prepared of penicillin v, metronidazole and oxytetracycline, using LCMS grade water. These were placed in glass amber vials and kept in a dark box, with aliquots taken over the course of 72 hours. Untargeted analysis was carried out by direct infusion on an FT-ICR mass spectrometer. Three days was chosen as the longest period of time the experiments could run within the time constraints of this project. Also due to the time constraints, no repeats were conducted.

4.2.3 Gas-Phase Photodegradation

Gas-phase photodegradation was carried out using a laser-interfaced mass spectrometer, an AmaZon SL dual funnel electrospray ionization quadrupole ion-trap (ESI-QIT) mass spectrometer (Bruker Daltonics Inc., Billerica, MA, USA). The laser parameters can be found in **Table 4.1**.

Table 4.1: Parameters used for gas-phase photolysis scans on metronidazole, oxytetracycline and penicillin v.

	Metronidazole	Oxytetracycline	Penicillin v
Capillary (V)	4500	4500	4500
Nebuliser (psi)	14.0	14.0	14.0
Dry Gas (L/min)	10.0	10.0	4.0
Dry Temperature (°C)	160	160	200
Accumulation (ms)	2	5	5
Laser Power (mJ)	0.2	0.2	0.2

The laser-interfaced mass spectrometer was set to scan the range 214-400 nm (UVC to UVA), with laser step sizes of 2 nm. Solution-phase UV spectra of the three compounds in their protonated and neutral forms were also recorded for comparison to the gas-phase UV spectra (solution-phase UV spectra shown in “Results”, section 4.3.3). Graphical gas-phase UV spectra are not included as the interpretation of the data is too preliminary, and much more interpretation and work is needed. The spectra are however described in (section 4.3.3).

Solutions of penicillin v were prepared in acetone (3.51 mg/L). TFA (0.1%) was used to aid protonation. Solutions of oxytetracycline and metronidazole were dissolved in acetonitrile (4.61 and 1.72 mg/L respectively). Each solution was analysed three times and then averaged.

4.2.4 *Energy Dependent Fragmentation Maps*

Energy-dependent fragmentation maps (also known as HCD plots - higher-energy collisionally activated dissociation plots) were created using a Thermo Scientific Orbitrap Fusion™ Tribrid™ mass spectrometer. Metronidazole was analysed over the collision energy range 0-50%, penicillin v was analysed over the range 0-90% and oxytetracycline was analysed over the range 0-70%. The antibiotic solutions detailed in section 4.2.3 were used. All plots shown are averaged from three analyses (there was little to no variability between the three). These plots were obtained to aid in the deduction of the fragment structures.

4.3 *Results and Discussion*

To study the degradation of the three antibiotics, both the parent ion signal intensities and the degradant ion signal intensities were extracted from the mass spectra. Parent compound intensities in the mass spectra were expected to decrease over time if they were being degraded, and degradant ion intensities were expected to increase over time.

In order to determine whether signal intensities were increasing or decreasing, the twenty most intense ions in each spectrum were examined for each of the three antibiotics for every mass spectrum representing each time point for the hydrolysis only and hydrolysis and photolysis degradation treatments. For convenience, rather than plotting absolute ion intensities, intensities relative to the intensity at time zero were used for mapping the peak intensities of the parent ions. As the photolysis only results were obtained on a different instrument (the laser-interfaced mass spectrometer), the results are reported separately for clarity.

4.3.1 Hydrolysis with photolysis

4.3.1.1 Metronidazole

Metronidazole ionised as its $[M+H]^+$, $[M+Na]^+$ and $[M+K]^+$ molecules (m/z 172, 194 and 210), in addition to forming charge sharing dimers, again with hydrogen, sodium and potassium (m/z 343, 365 and 381). The combined intensity of these signals is plotted against time in **Figure 4.3**. Over the eight-hour period, the combined peak intensities did not decrease.

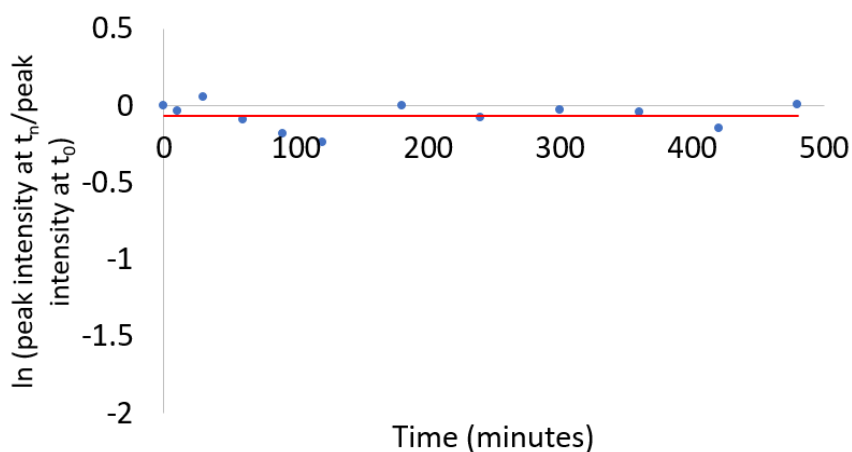


Figure 4.3: Combined peak intensity for m/z 172, 194, 210, 343, 365 and 381 of metronidazole on time course exposure to UV light (wavelength 365 nm).

Metronidazole does not appear to degrade, as the peak intensity remains constant throughout the entire time course exposure. However, despite this, there were still several candidates for metronidazole degradants, identified as signals increasing in intensity over the time course of the experiment; three m/z values increased in peak intensity in this way. The peak intensities for these candidate degradants (m/z 213, 387 and 409) are plotted in **Figure 4.4**. However, none of the suspected degradants increases in intensity in correspondence with the peak intensity of the metronidazole parent molecule, since this does not decrease in intensity. The three fragments signals reached similar intensities. As the m/z values are larger than that of metronidazole, it is

probable that these are degradants of the metronidazole charge sharing dimers. In future work, this can be tested by analysing these degradants using MS/MS.

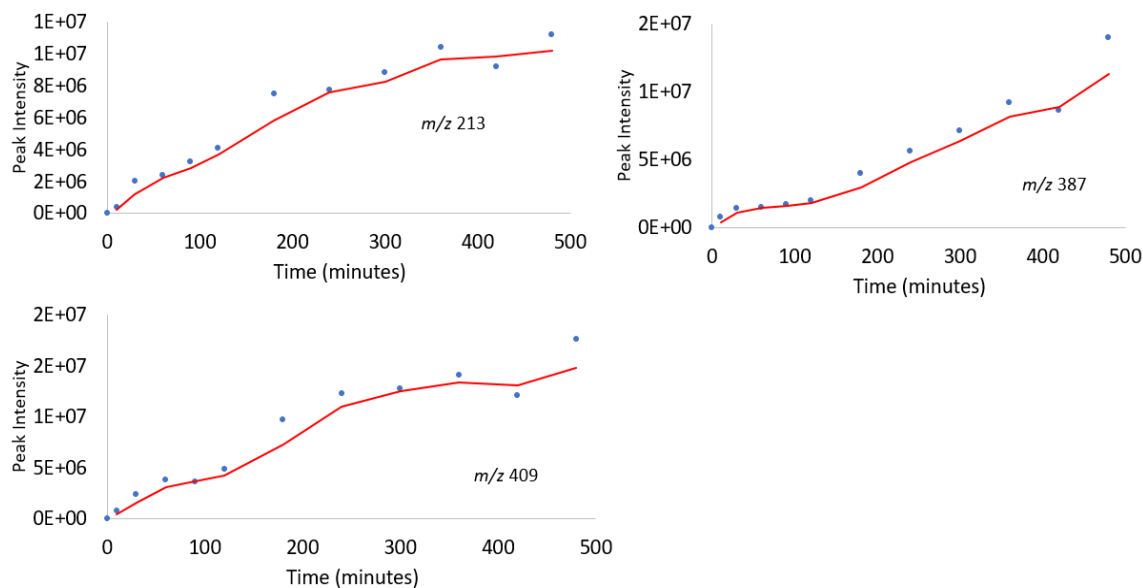


Figure 4.4: Peak intensity for potential degradants of metronidazole after a time course exposure to UV light (wavelength 365 nm).

Another couple of fragments that were of interest were the fragments with m/z 57 and 128. They were present in the solution, but they do not increase in intensity over the time course exposure. Instead, they remain at a constant intensity throughout. These fragments also appear later in the gas phase photolysis section (section 4.3.3.1).

The main reason that these three potential degradant signals are increasing in intensity, while metronidazole appears not to degrade is likely to be due to signal suppression of the parent ions (m/z 172, 194, 210, 343, 365 and 381). A high concentration of the antibiotic solution was used (10^{-5} M) to ensure being able to see any degradants that were produced. If signal suppression is occurring, even if a small amount of metronidazole was degrading this would not be shown as the peak intensities would remain the same.

Signal suppression can happen in several ways.⁹⁷ The reason for it in this case is likely to be due to the high concentration of the solution that was used for the analysis. ESI, while normally a very efficient method for ionising polar molecules, loses the approximate linearity of the response when concentrations reach around 10^{-5} M.⁹⁷ This could be due to the limited amount of excess charge available to the ESI droplets, resulting in competition for the charges. The other reason could be that the ESI droplet surfaces become fully saturated with the analyte, which prevents the ejection of the ions trapped inside the droplets. This results in competition for the available droplet surface. Either of these situations would result in suppression of the signal observed.⁹⁷

Signal suppression was tested by analysing two different solutions of metronidazole using the FT-ICR: 10 mg/L and 50 mg/L (the actual concentration used in degradation experiment). The intensities of each of the ions in the spectra from the 50 mg/L solution would be expected to be 5x those of the same signals in the spectra from the 10 mg/L solution. The results obtained are shown in **Table 4.2**, with the signal intensities expressed as a ratio (more concentrated solution: less concentrated solution). The ratios are either well above five (ions at m/z 172, 210 and 343) or well below five (m/z 194, 365 and 381), suggesting there is an effect of ion suppression or enhancement.

Table 4.2: the ratio of the peak intensities for the ions of metronidazole from two solutions with different concentrations (50 mg/L and 10 mg/L).

m/z value	Ratio of signal intensities in 50: 10 mg/L solution spectra
172.0716	7.25
194.0535	1.32
210.0274	10.44
343.2957	8.79
365.1176	0.10
381.2526	3.93

The signal intensities for the m/z values that have been suppressed have thus been removed, and the new combined peak intensities of m/z 172, 210 and 343 ($[M+H]^+$, $[M+K]^+$ and $[2M+H]^+$) replotted in Figure 4.5.

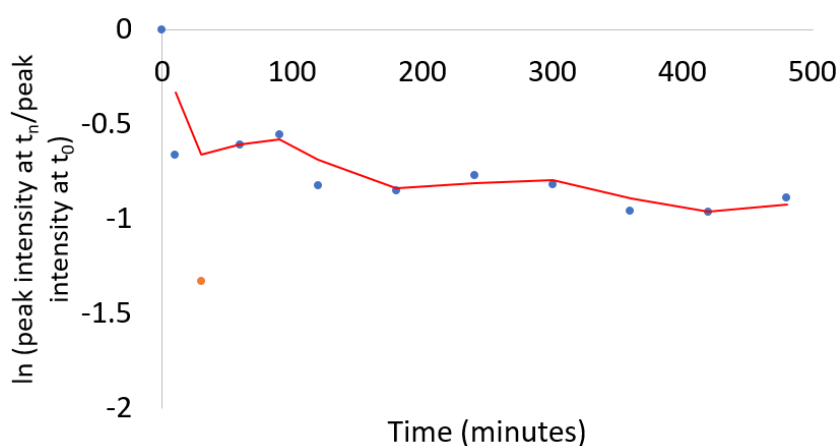


Figure 4.5: Peak intensity for m/z 172, 210 and 343 of metronidazole after a time course exposure to UV light (wavelength 365 nm). Peak intensities of m/z values experiencing ion suppression have been removed. The red line represents the moving average. Outliers shown in orange.

The result would suggest that metronidazole does degrade *via* either hydrolysis or photolysis (or both), as the combined peak intensity over the time course exposure of UV decreases.

4.3.1.2 Oxytetracycline

Oxytetracycline ionised as its $[M+H]^+$, $[M+Na]^+$ and $[M+K]^+$ molecules (m/z 461, 483 and 499) as well as forming one charge sharing dimer, $[2M+Na]^+$ (m/z 943). The combined peak intensities of these signals were plotted against time in **Figure 4.6**. Over the time course of this experiment, the combined peak intensities for oxytetracycline decreased (R^2 value of greater than 0.9).

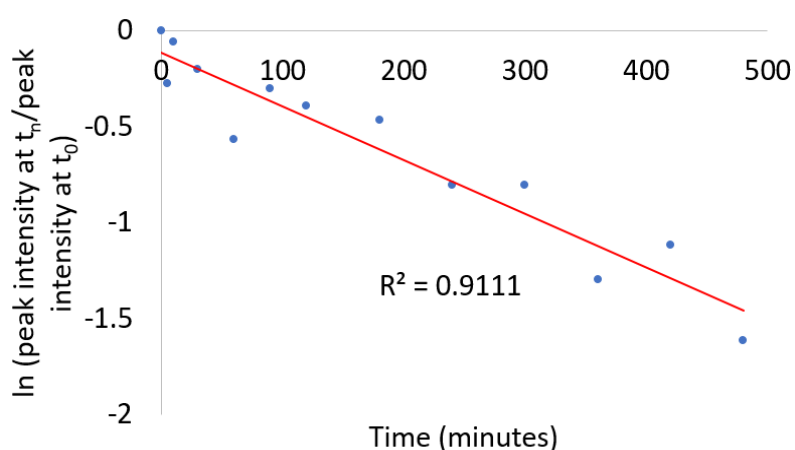


Figure 4.6: Peak intensity for m/z 461, 483, 499 and 943 of oxytetracycline on time course exposure to UV light (wavelength 365 nm).

This decrease in intensity would suggest that oxytetracycline degrades, either *via* hydrolysis or photolysis or a combination of the two.

After plotting the peak intensities of the highest intensity m/z s that appeared as the time increased, only four m/z values (m/z 480, 497, 498 and 519 – shown in **Figure 4.7**) were identified as increasing in intensity in correspondence with the decreasing peak intensity of the oxytetracycline parent molecule. Three of these (m/z 480, 497 and 498) all increase in peak

intensity up until around 180 minutes, before then decreasing in peak intensity again. m/z 519 increases in peak intensity until around 200 minutes where the intensity then remains consistent for the remainder of the experiment. m/z 519 gave a much weaker signal than the other three signals, with the intensity being a tenth of the intensities for other three potential degradants.

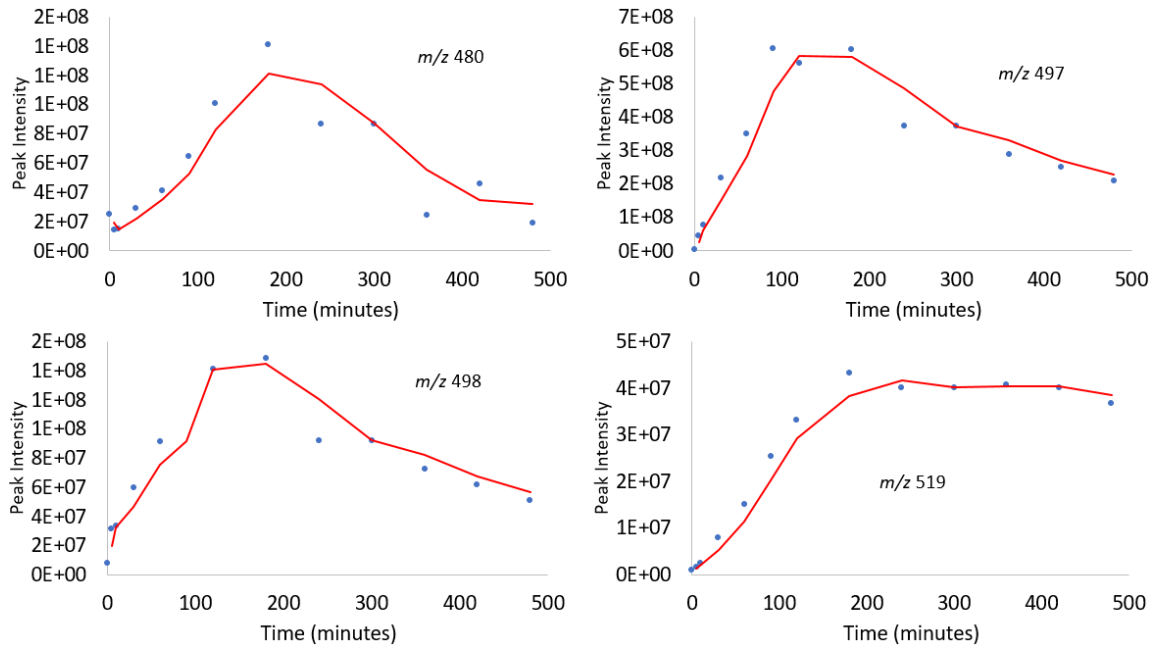


Figure 4.7: Peak intensity for potential degradants of oxytetracycline on time course exposure to UV light (wavelength 365 nm).

As ionised metronidazole experienced ion suppression, oxytetracycline and penicillin v were both tested as well. The results from the oxytetracycline ion suppression test can be found in **Table 4.3**, and the results from penicillin v can be found in **Table 4.4**.

Table 4.3: the ratio of the peak intensities for the ions of oxytetracycline from two solutions with different concentrations (50 mg/L and 10 mg/L).

<i>m/z</i> value	Ratio of signal intensities in 50: 10 mg/L solution spectra
461.1550	4.42
483.1368	7.41
499.1116	19.86
943.2843	6.22

None of the ions appear to be experiencing ion suppression, although *m/z* 499 appears to be undergoing signal enhancement, and so the time course exposure of the parent compound does not need to be replotted.

4.3.1.3 Penicillin v

Penicillin v ionised as its $[M+Na]^+$ and $[M+K]^+$ molecules (m/z 374 and 389) as well as forming two charge sharing dimers, $[2M+Na]^+$ and $[2M+K]^+$ (m/z 723 and 739). The combined peak intensities of these m/z values are plotted against time in **Figure 4.8**. The peak intensity of penicillin v decreases steadily over the time course exposure to UV light (R^2 value greater than 0.9, suggesting constant degradation throughout the experiment).

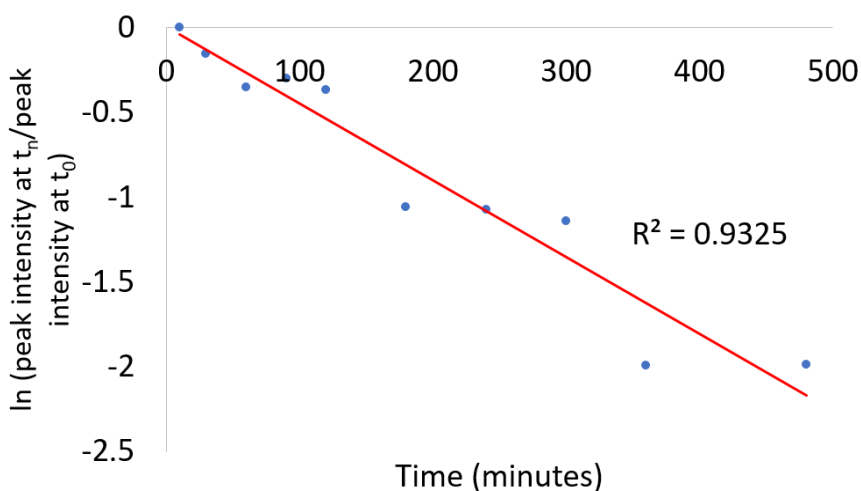


Figure 4.8: Peak intensity for m/z 374, 389, 723 and 739 of penicillin v on time course exposure to UV light (wavelength 365 nm).

Once again, after plotting the m/z values with the highest intensities, eight potential degradant candidates were identified (**Figure 4.9**). The most intense fragments that were formed were m/z 174 and 190, reaching intensities up to 10x as large as the other fragments. Fragments with m/z values of 248 and 250 increase in intensity until around 350 minutes, and then remain constant for the remaining time.

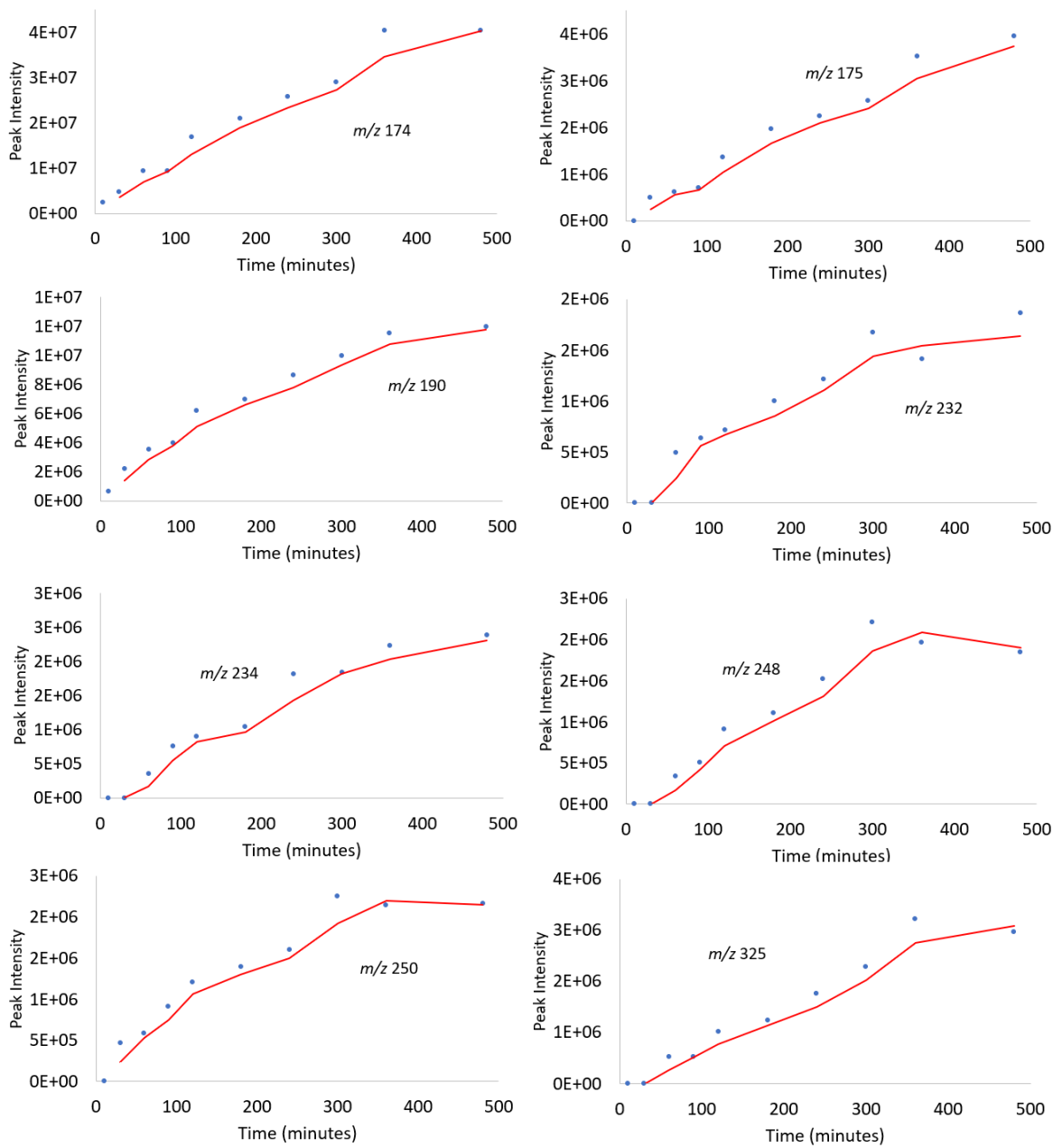


Figure 4.9: Peak intensity for suspected degradants of penicillin v after a time course exposure to UV light (wavelength 365 nm).

Table 4.4: the ratio of the peak intensities for the ions of penicillin v from two solutions with different concentrations (50 mg/L and 10 mg/L).

<i>m/z</i> value	Ratio of signal intensities in 50: 10 mg/L solution spectra
373.0826	0.89
389.0565	4.08
723.1757	1.80
739.1493	5.73

The ions with *m/z* 373 and 723 appear to be experiencing ion suppression, and so their intensities were removed. However, replotting the graph without the ions experiencing ion suppression only changed the R^2 value from 0.9325 (Figure 4.8) to 0.933 (Figure 4.10), showing that exclusion of the peak intensities for *m/z* 373 and 723 did not change how penicillin v appeared to degrade.

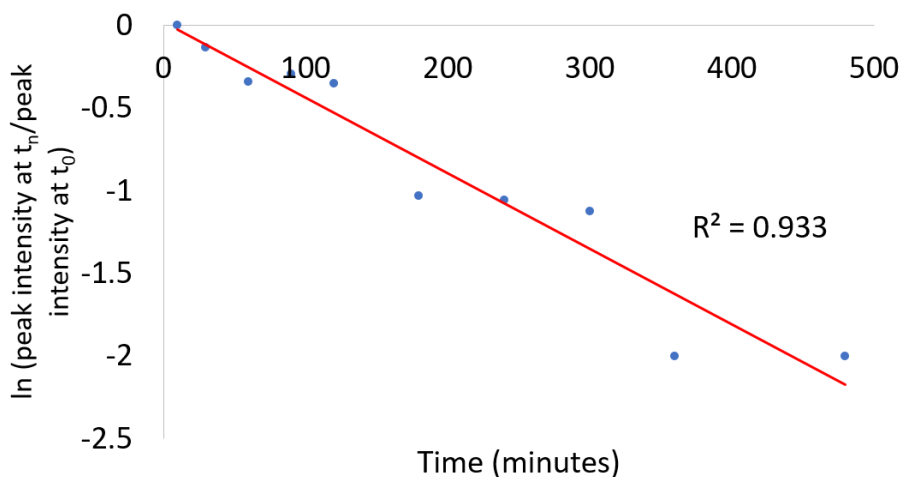


Figure 4.10: Peak intensity for *m/z* 389 and 739 of penicillin v on time course exposure to UV light (wavelength 365 nm). The ions experiencing ion suppression have been excluded from the peak intensity total.

4.3.2 Hydrolysis in the dark (no photolysis)

In this experiment, the individual antibiotic solutions were kept in the dark to ensure any degradation taking place was due to hydrolysis.

4.3.2.1 Metronidazole

Similarly to the hydrolysis in the light experiment, metronidazole ionised as the $[M+H]^+$, $[M+Na]^+$ and $[M+K]^+$ molecules (m/z 172, 194 and 210), as well as the charge sharing dimers with sodium and potassium (m/z 365 and 381). The combined peak intensities of these signals can be found plotted in **Figure 4.11** (excluding the m/z s experiencing ion suppression – m/z s 194, 368 and 381).

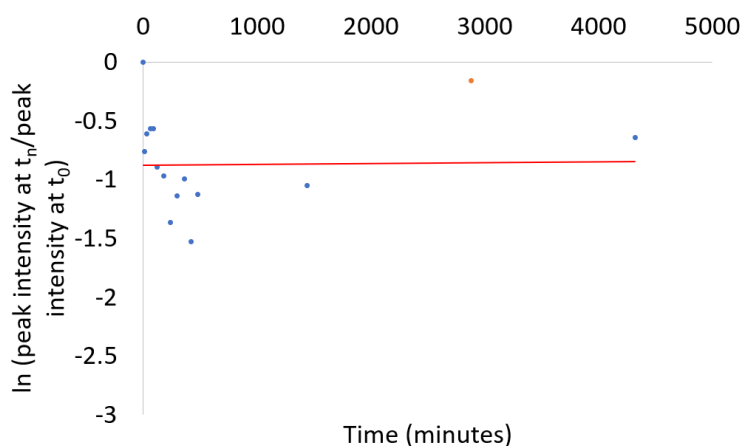


Figure 4.11: combined peak intensities of m/z 172 and 210 mapped over a period of 72 hours (4320 minutes). Peak intensities of m/z values experiencing ion suppression have been removed.

Outliers shown in orange.

The graph shows that the combined peak intensities of metronidazole ions do not decrease as the experiment progresses. This would suggest that metronidazole does not degrade *via* hydrolysis alone.

Moving on to potential degradants, there were three identified (shown in **Figure 4.12**). These three graphs all show an increase in peak intensity (up to around 500 minutes for m/z 178 and 196, up to around 3000 minutes for m/z 249) which is then followed by a decrease in peak intensity.

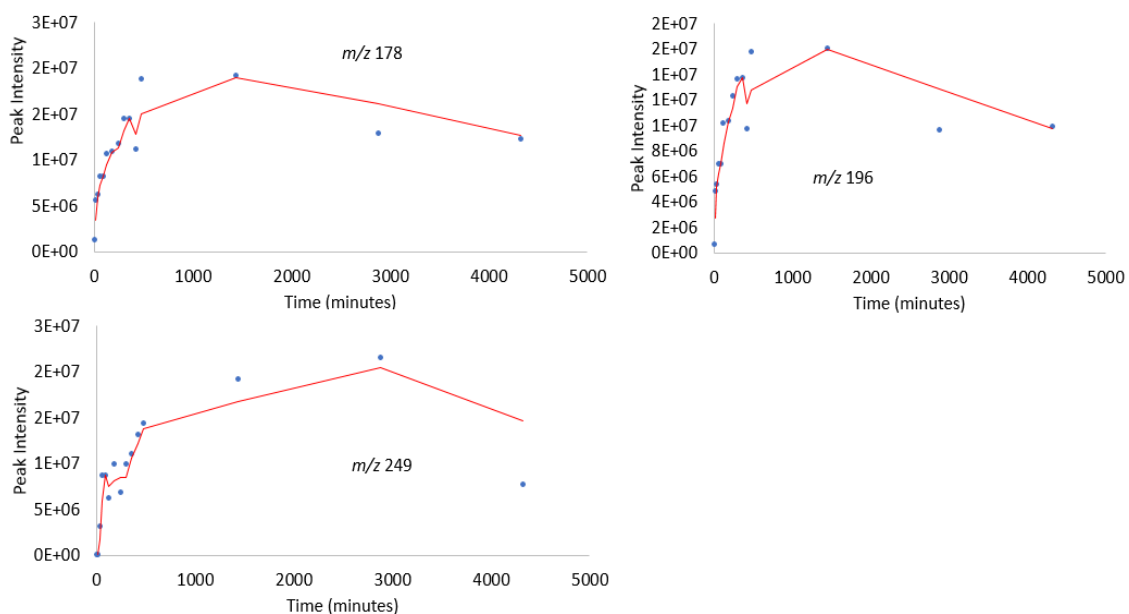


Figure 4.12: production of potential hydrolytic degradants of metronidazole with m/z 178, 196 and 249 over a period of 72 hours (4320 minutes).

This suggests that the potential degradants are created, and then degrade themselves. The masses of the ions suggest that they are degradants of charge sharing dimers of metronidazole, as they all have larger m/z s than the parent compound (m/z 172). The difference between m/z 196 and 178 is 18, which would suggest the loss of a water molecule. The production of these ions could involve the hydrolysis of the parent compound, followed by further degradation into ions with a low intensity (too low to be detected in this experiment). The appearance of these “degradants” is somewhat suspicious, as the parent ion does not decrease in intensity. Therefore, it could be presumed that these “degradants” are analytical artifacts. Further experimentation (possibly using a lower concentration of metronidazole) would give greater insight into this.

Comparing this result to the result found when metronidazole in water is irradiated with UV light (Figure 4.5), it appears that metronidazole undergoes photolysis, but does not hydrolyse within 72 hours of being dissolved at room temperature in an aqueous solution.

4.3.2.2 Oxytetracycline

Again, similarly to the hydrolysis in the light experiment, oxytetracycline ionised as its $[M+H]^+$, $[M+Na]^+$ and $[M+K]^+$ molecules (m/z 461, 483 and 499) as well as forming one charge sharing dimer, $[2M+Na]^+$ (m/z 943). The combined peak intensities show no decreasing trend across the 72 hours, with an R^2 value of 0.0002 shown in **Figure 4.13**.

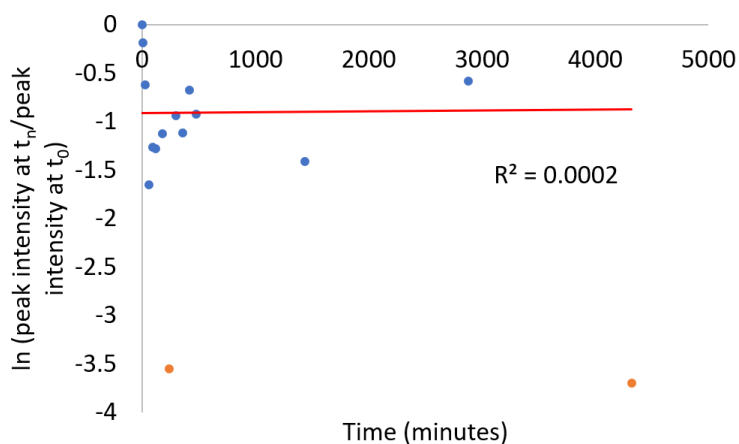


Figure 4.13: combined peak intensities of m/z 461, 483, 499 and 943 mapped over a period of 72 hours (4320 minutes). Outliers shown in orange.

Oxytetracycline was the only antibiotic that did not demonstrate any ion suppression, and so no m/z s were excluded from the graph. Despite showing no decrease in intensity over time, several potential degradants were identified (signals showing an increase in intensity over the time course) (**Figure 4.14**). m/z 241 showed an initial increase in peak intensity, up to around 2000 minutes, when the peak intensity then decreased again. m/z 500 shows a similar trend to m/z 241. The other potential degradants all increase in peak intensity with a near-linear correlation to the time.

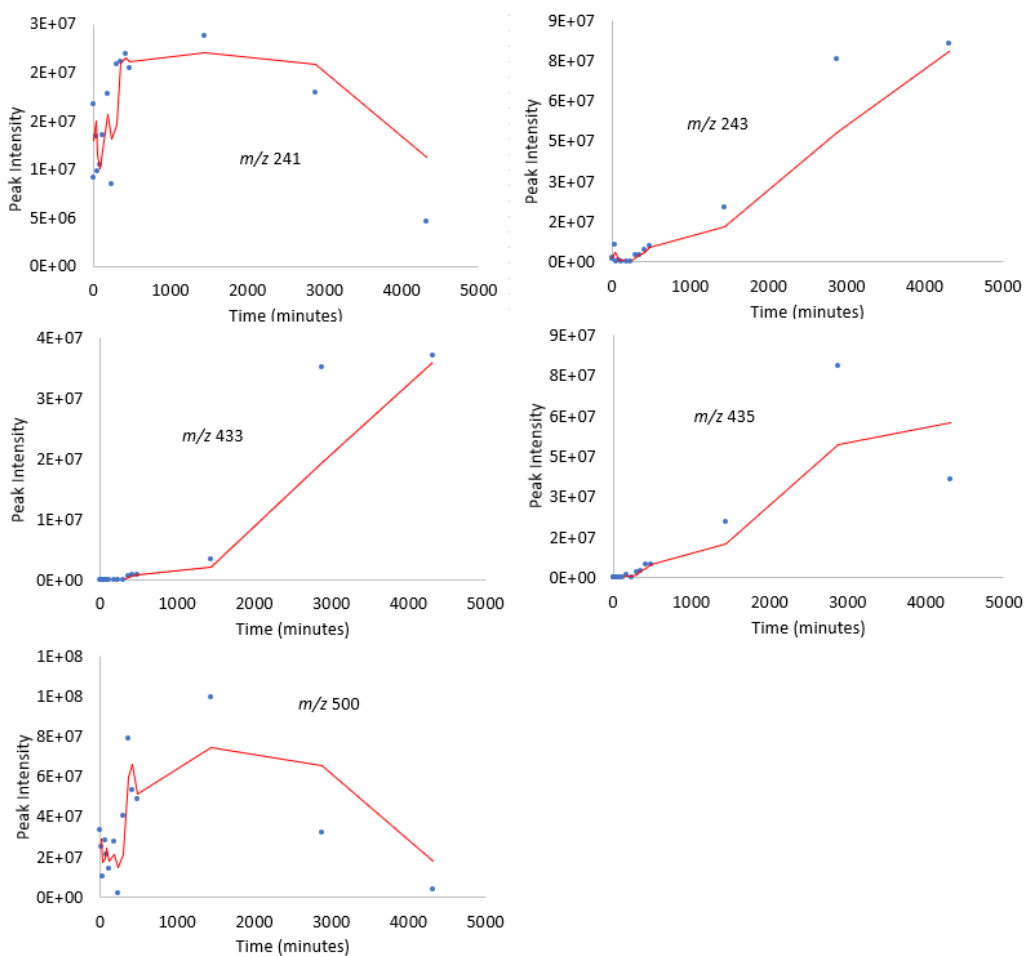


Figure 4.14: production of hydrolytic degradants of oxytetracycline over a period of 72 hours (4320 minutes).

Due to the significant difference between the results of the two experiments (hydrolysis with photolysis and hydrolysis in the dark) for oxytetracycline, an additional experiment was conducted to investigate further whether oxytetracycline was degrading over the time course of the experiment.

UV spectra were taken of oxytetracycline in an aqueous solution kept in the dark over a period of 6 hours. Comparing the spectrum taken at the start with that taken after 6 hours reveals that the UV absorbance has not changed at all (Figure 4.15). This is consistent with the result of the hydrolysis in the dark experiment (Figure 4.13) in which oxytetracycline does not hydrolyse, but rather only photolyses (over 6 hours).

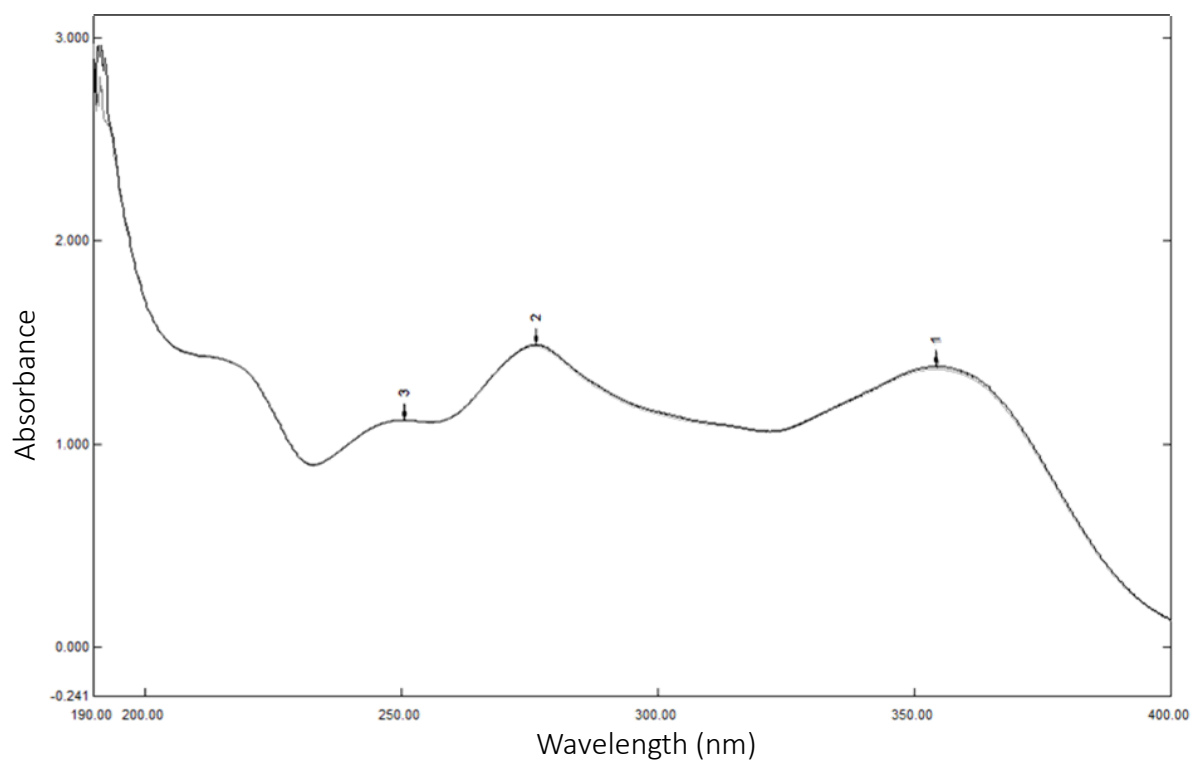


Figure 4.15: UV spectra of oxytetracycline in aqueous solution while kept in the dark. Two spectra are overlaid: T_0 and T_6 hours.

4.3.2.3 Penicillin v

Penicillin v also showed a similar response to the hydrolysis in the dark experiment as the metronidazole and oxytetracycline. It again ionised as its $[M+Na]^+$ and $[M+K]^+$ molecules (m/z 373 and 389) as well as forming two charge sharing dimers, $[2M+Na]^+$ and $[2M+K]^+$ (m/z 723 and 739). As for the photolysis and hydrolysis experiment, penicillin v had some ions that experienced ion suppression (m/z 373 and 723) and so the graph was plotted using the combined intensities of just m/z 389 and 739 against time (Figure 4.16). Unexpectedly, the peak intensities do not decrease over time but in fact appears to increase. This increase in intensity could be due to true variance, a variance in ionisation that is inherent in the nature of the compounds, and not due to measurement error, imprecision of the model used, or other factors.⁹⁸

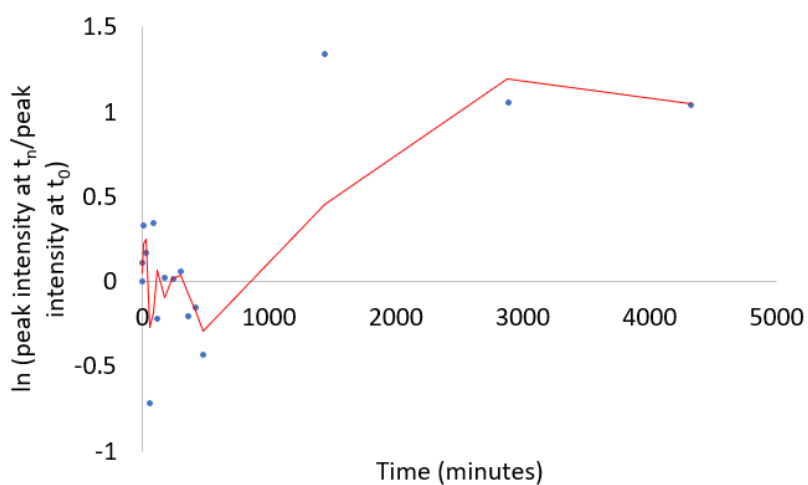


Figure 4.16: combined peak intensities of m/z 389 and 739 mapped over a period of 72 hours (4320 minutes).

There were no potential degradants detected from penicillin v when kept in an aqueous solution in the dark, which is further evidence that penicillin v does not degrade *via* hydrolysis within 72 hours.

4.3.3 Gas phase photodegradation

The photon energies scanned for the gas phase photodegradation correspond to the wavelength range 214 – 400 nm. This range can be broken down into UVA (photon energies 3.10-3.87 eV), UVB (3.87-4.28 eV) and UVC (4.28-12.40 eV), as depicted in **Figure 4.17**. The only wavelengths that reach Earth's surface are the longer wavelengths, 290 – 400 nm (UVA and UVB as highlighted in yellow in **Figure 4.17**).⁹⁹

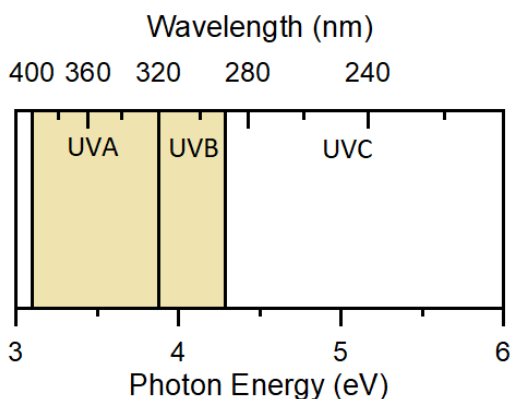


Figure 4.17: UV wavelengths, showing UVA, UVB and UVC in both wavelengths (top x axis) and photon energy (bottom x axis).

The solution-phase UV absorption spectra of each individual antibiotic were obtained under both neutral conditions and acidic conditions. This was in order to show if there was any shift (blue shift or red shift) in the bands observed in order to see the relevance of pH on the transitions of the molecule. Observing the blue shift/red shift also allows you to see if the molecule is likely to degrade in either the UVA or the UVB. As the UV spectrum obtained in the gas phase was under acidic conditions, it is expected to look like the UV spectrum obtained under acidic conditions in the solution phase.

4.3.3.1 Metronidazole

The structure of metronidazole is shown in **Figure 4.18**.

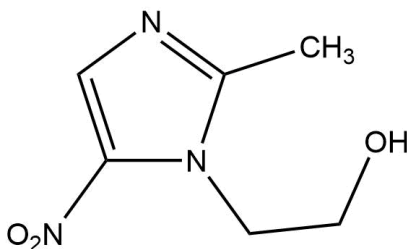


Figure 4.18: Structure of metronidazole

Figure 4.19a shows the solution-phase UV absorption spectrum of metronidazole (previously published by El-Ghobashy *et al*¹⁰⁰) obtained under neutral conditions. In the neutral solution-phase spectrum there is one major band ($\lambda_{\text{max}} = 3.88$ eV), with another major band beginning to appear around 5.64 eV. **Figure 4.19b** shows the solution-phase UV absorption spectrum of protonated metronidazole, recorded at pH 2. This shows one major band that starts appearing around 5 eV and looks as if it could be the same as the band beginning to appear in the neutral UV spectra around 4.5 eV. There is also a major band in the protonated spectrum ($\lambda_{\text{max}} = 3.94$ eV), with a molar absorption coefficient of around $10 \text{ dm}^3 \text{ mol}^{-1} \text{ cm}^{-1}$. This is of similar intensity to the major band in the neutral spectrum. The major band has a $\lambda_{\text{max}} = 3.94$ eV in the protonated spectrum, compared to the $\lambda_{\text{max}} = 3.88$ eV, suggesting a slight blue shift.

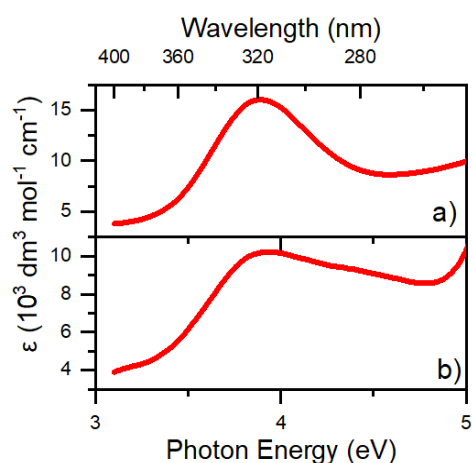


Figure 4.19: Solution-phase absorption spectra for metronidazole under (a) neutral conditions and (b) protonated conditions. The solid lines are five-point adjacent averages of the data points.

The gas-phase photodepletion spectrum (gas-phase absorption spectrum) and the photofragment production spectra were obtained over the 400–214 nm range. Metronidazole produced 10 photofragments, indeed many more fragments than were expected based on previous research, where a very similar experiment identified only five photofragments of oxybenzone.⁹³ The photofragments with the highest intensities are shown in **Table 4.5**, along with the major bands observed in the gas-phase spectra and the potential neutral lost to obtain that m/z . The table presents the results from the photodepletion spectrum, i.e. for the precursor ion (metronidazole $[M+H]^+$ (***bold italics***)), and the results from the photofragmentation spectra, i.e. for the two most intense fragments. The major feature observed in these spectra is the band found with $\lambda_{\text{max}} = 5.3$ eV, with a more minor band with $\lambda_{\text{max}} = 4.2$ eV.

Table 4.5: Photon energy absorbances found in the photodepletion and the photofragmentation spectra of metronidazole identified in the gas phase. w = weak, m = medium, s = strong, vs = very strong (relative to each other)

<i>m/z</i>	$\lambda = 4.2$ eV	$\lambda = 5.3$ eV	Potential neutral loss from <i>m/z</i> 172
172	✓(w)	✓(s)	N/A
128	✓(w)	✓(vs)	-CH ₂ CH ₂ O
82		✓(m)	-CH ₂ CH ₂ O, -NO ₂

The gas-phase UV absorption spectrum has a similar shape to the protonated solution-phase UV spectra (**Figure 4.19**), although there appears to be a slight blue shift upon transition from the solution to the gas phase. This shows that the species giving rise to the solution-phase UV spectrum is metronidazole [M+H]⁺.

4.3.3.2 Penicillin v

The structure of penicillin v is shown in **Figure 4.20**.

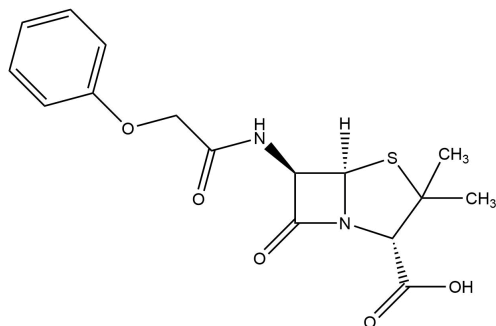


Figure 4.20: Structure of penicillin v

Figure 4.21a reports the solution-phase absorption spectrum for penicillin v under neutral conditions, previously published by Oprea *et al*¹⁰¹, showing a minor band with a $\lambda_{\text{max}} = 4.73$ eV and a molar absorption coefficient of $16 \text{ dm}^3 \text{ mol}^{-1} \text{ cm}^{-1}$. **Figure 4.21b** displays the solution-phase absorption spectrum for protonated penicillin v. The absorption spectrum for protonated penicillin v only shows one major band at $\lambda_{\text{max}} = 4.62$ eV and increasing absorption intensity to higher photon energies.

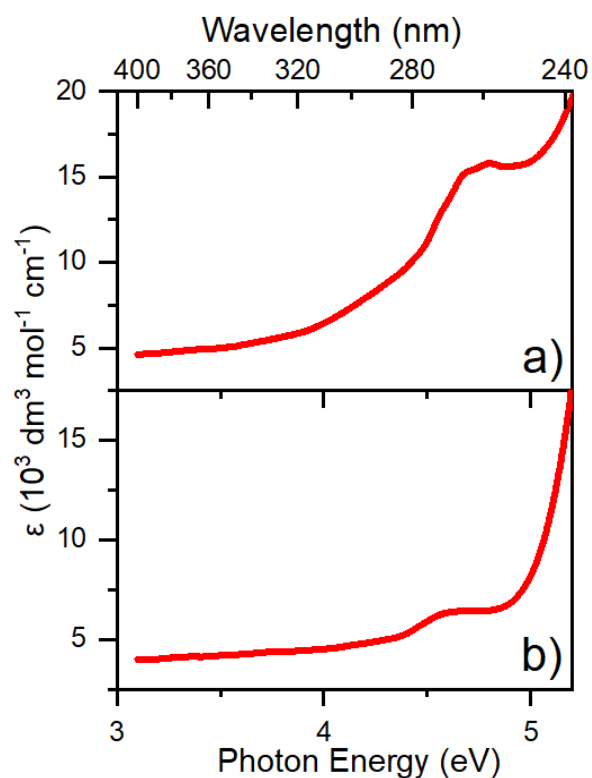


Figure 4.21: Solution-phase absorption spectra for penicillin v under (a) neutral conditions and (b) protonated conditions. The solid lines are five-point adjacent averages of the data points.

The photodepletion spectrum and the photofragment production spectra were obtained, scanned over the 400-214 nm range. There was one major feature evident in these spectra, observed with $\lambda_{\max} = 4.0$ eV. In total, there were 25 photofragments detected.

Table 4.6 reports the features observed in the photodepletion spectrum of protonated penicillin v (***bold italics***), and the bands observed in the gas phase UV photofragment production spectra of the three most intense photofragments.

Table 4.6: Photon energy absorbances found in the photodepletion and the photofragmentation spectra of penicillin v identified in the gas phase. vw = very weak, w = weak, s = strong, vs = very strong (relative to each other).

<i>m/z</i>	$\lambda = 4.0 \text{ eV}$	$\lambda = 5.5 \text{ eV}$	Potential neutral loss from <i>m/z</i> 351
351	✓(vw)	✓(w)	-
213	✓(w)	✓(vs)	-C ₆ H ₅ OH, -CO ₂
175		✓(s)	-C ₁₀ H ₁₀ NO ₂
174		✓(w)	

An initial, tentative assignment of the structures of the neutral fragments lost following photofragmentation are also reported in this table, and from this a very basic understanding of how penicillin v degrades *via* gas-phase photolysis is achieved (discussed further in section 4.3.5.2). However, more analysis is required to fully understand the fragmentation pathways.

Comparing the protonated solution-phase UV spectrum to the gas-phase UV spectrum shows that the two spectra have a similar profile, with the major bands appearing at the same photon energy. This shows that the species giving rise to the solution-phase UV spectrum is penicillin v [M+H]⁺.

4.3.3.3 Oxytetracycline

The structure of oxytetracycline is shown in **Figure 4.22**.

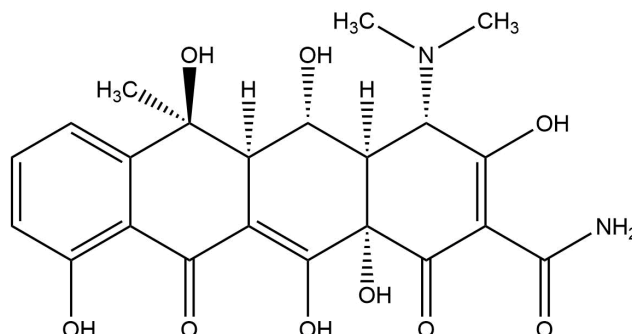


Figure 4.22: Structure of oxytetracycline

Figure 4.23a shows the solution-phase absorption spectrum for oxytetracycline in neutral conditions. This UV spectrum has previously been published by Marina *et al.*¹⁰² The solution-phase absorption spectrum shows two bands, and the onset of a third. There are two bands at $\lambda_{\text{max}} = 3.35$ eV and 4.59 eV, and the third appears above 5.08 eV.¹⁰³ **Figure 4.23b** shows the solution-phase absorption spectrum for oxytetracycline in its protonated form. This spectrum shows two less intense bands around $\lambda_{\text{max}} = 3.54$ eV and $\lambda_{\text{max}} = 4.59$ eV. The absorption intensity starts to increase steeply as the photon energy reaches 5.21 eV. Comparing this to the neutral solution-phase spectrum, there would appear to be a blue shift in the absorbance regions; the minor band seen in the neutral UV spectrum at $\lambda_{\text{max}} = 3.35$ eV has shifted to $\lambda_{\text{max}} = 3.54$ eV in the protonated spectrum, the band at $\lambda_{\text{max}} = 4.59$ eV has stayed at $\lambda_{\text{max}} = 4.59$ eV, and the energy at which the intensity starts to increase dramatically has changed from $\lambda_{\text{max}} = 5.08$ eV to $\lambda_{\text{max}} = 5.21$ eV.

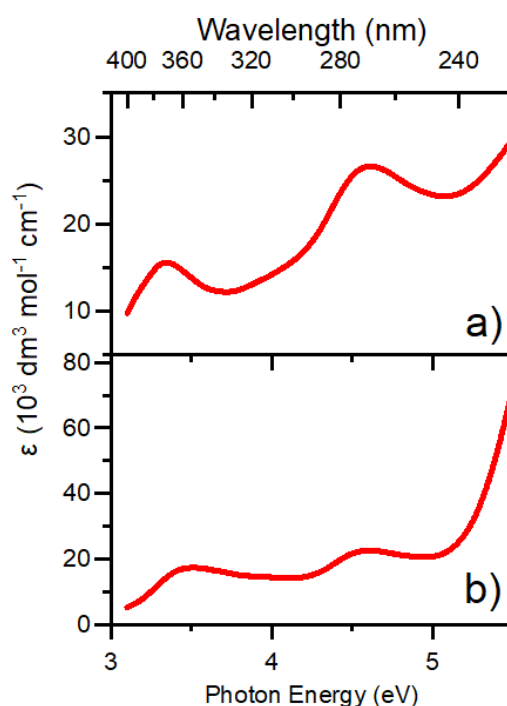


Figure 4.23: Solution-phase absorption spectra for oxytetracycline under (a) neutral conditions and (b) protonated conditions. The solid lines are five-point adjacent averages of the data points.

The photodepletion spectrum and the photofragment production spectra were recorded across the 400-214 nm range. In total, oxytetracycline photodegraded to produce 64 fragments. The features observed in the photodepletion spectrum are listed in **Table 4.7 (*bold italics*)**, along with the 12 most intense fragments. The major feature of these spectra is the band observed with $\lambda_{\text{max}} = 4.8$ eV, with two more minor features seen at $\lambda_{\text{max}} = 3.3$ eV and $\lambda_{\text{max}} = 4.0$ eV.

An initial, tentative assignment of the structures of the neutral fragments lost following photofragmentation are also shown in **Table 4.7**. These can be used to start to identify a potential pathway by which oxytetracycline photofragments.

Table 4.7: Photon energy absorbances found in the photodepletion and the photofragmentation spectra of oxytetracycline identified in the gas phase. w = weak, m = medium, s = strong, vs = very strong, vvs = very very strong (relative to each other).

<i>m/z</i>	$\lambda = 3.3 \text{ eV}$	$\lambda = 4.0 \text{ eV}$	$\lambda = 4.8 \text{ eV}$	Potential fragment loss from <i>m/z</i> 461
461	✓(w)	✓(w)	✓(m)	N/A
444	✓(vs)	✓(vs)	✓(vs)	-OH
443	✓(vvs)			-H ₂ O
427		✓(m)	✓(s)	-H ₂ O, -OH
426		✓(vvs)	✓(vvs)	-H ₂ O, -OH
408		✓(m)	✓(s)	
398		✓(m)	✓(m)	
381	✓(s)			
365	✓(m)		✓(w)	
337	✓(s)		✓(m)	
226	✓(s)			
201	✓(m)		✓(s)	
154	✓(m)		✓(m)	

Comparing the gas-phase UV spectrum to the protonated solution-phase UV spectrum shows that the two spectra are similar, although there appears to be a blue shift of the entire spectrum by approximately 25 nm upon transition from the solution to the gas phase. This suggests that the species giving rise to the solution-phase UV spectrum is oxytetracycline $[M+H]^+$.

4.3.4 Energy Dependent Maps

The purpose of performing CID under higher energy collision regimes is to gain an understanding of the gas-phase collision induced dissociation fragmentation of the compounds for comparison with their gas-phase laser induced dissociation behaviour. This can also provide some insight into the most labile molecular bonds with respect to fragmentation. Plotting the energy dependence of fragment ion generation allows the differentiation of primary fragments (directly from the parent compound) and secondary fragments (from a primary fragment).

4.3.4.1 Metronidazole

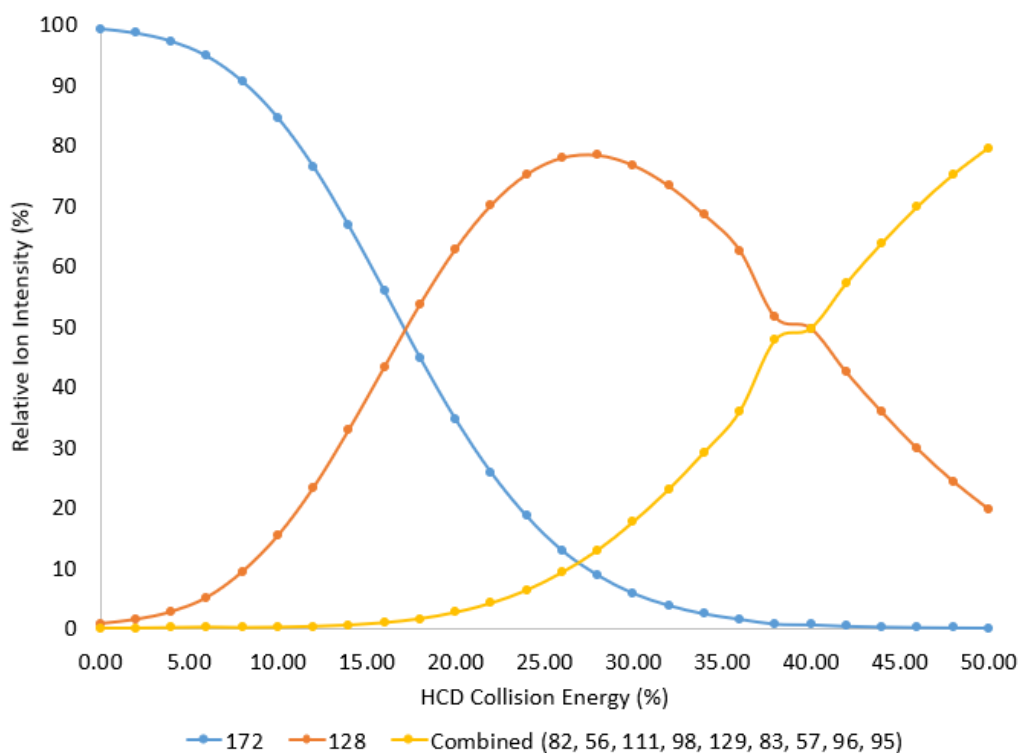


Figure 4.24: Parent ion dissociation curve of metronidazole $[M+H]^+$ (m/z 172), along with production curves for the primary and secondary fragments formed upon HCD between 0–50% energy.

With protonated metronidazole (Figure 4.24), only one primary fragment (m/z 128 – orange line) was formed, reaching its maximum relative intensity of 80% at around 25-30% HCD collision energy

setting, before decreasing. There were also nine secondary fragments (m/z 82, 56, 111, 98, 129, 83, 57, 96 and 95 - combined into one line, yellow), starting to be produced around 20% energy, and reaching their maximum relative intensity at an energy higher than 50% HCD collision energy. The fragments m/z 57, 82, 95, 98, 111 and 128 are also found in gas-phase photolysis.

4.3.4.2 Penicillin v

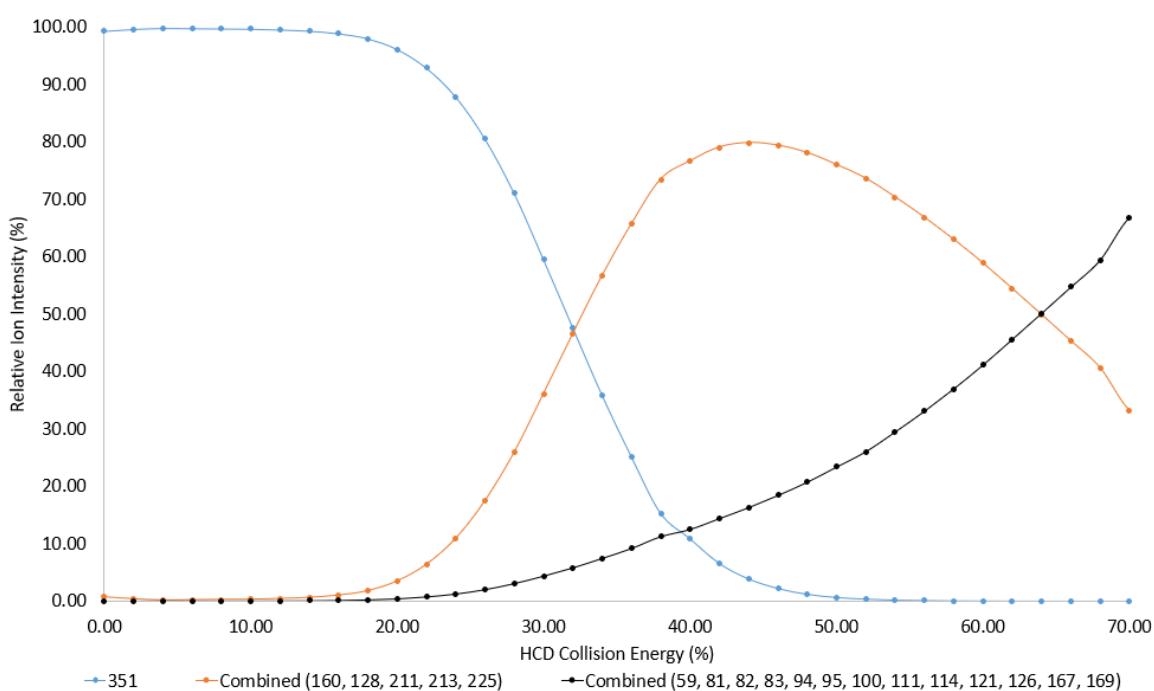


Figure 4.25: Parent ion dissociation curve of penicillin v $[M+H]^+$ (m/z 351), along with production curves for the primary and secondary fragments formed upon HCD between 0–90% energy setting.

There were a large number of HCD fragments produced for protonated penicillin v (Figure 4.25), with four primary fragments (m/z 160, 128, 211, 213 and 225 – combined into the orange line), reaching their combined maximum relative intensity at around 40% HCD collision energy. The intensity of these fragments then decreases again, although decreasing more slowly than it increased. There were also 13 secondary fragments (m/z 59, 81, 82, 83, 94, 95, 100, 111, 114, 121, 126, 167 and 169 – all combined into the black line), which start to be formed at a similar energy to

the primary fragments but increases in relative intensity much more slowly. The graph does not show the energy at which they would reach their maximum relative intensity as their curve has not plateaued at the highest collision energy setting of 70%. The CID fragments used for the LC-SRM quantification analysis were m/z 310 (not observed here) and m/z 160 (a primary fragment).

4.3.4.3 Oxytetracycline

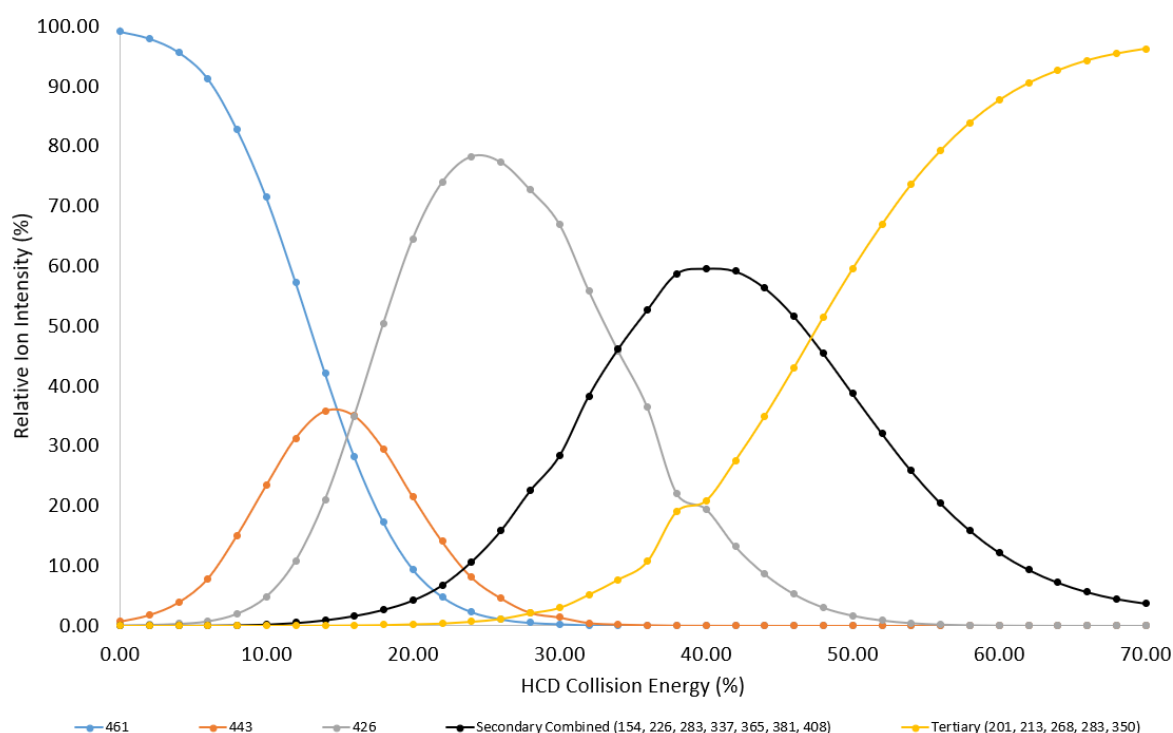


Figure 4.26: Parent ion dissociation curve of oxytetracycline $[M+H]^+$ (m/z 461), along with production curves for the primary, secondary and tertiary fragments formed upon HCD between 0–70% energy setting.

The HCD plot for protonated oxytetracycline (Figure 4.26) shows two primary fragments (m/z 443 and 426 – the same as the CID fragments used for quantitative analysis). m/z 443 (orange line), reaches its maximum relative intensity at around 15% HCD collision energy, and has completely decreased again by 35% HCD collision energy. m/z 426 (grey line), reaches the maximum relative intensity around 25% HCD collision energy. This fragment is no longer detectable (interpreted as

completely degraded) by 55% HCD collision energy. m/z 426 reaches a much higher relative ion intensity than m/z 443, reaching a relative ion intensity of around 80% compared to 35%. The secondary fragments (m/z 154, 226, 283, 337, 365, 381 and 408 – combined in the black line) all start to increase in intensity at around 15% HCD collision energy. The intensity of these secondary fragments reaches the maximum combined relative intensity of 60% at around 40% HCD collision energy and decreases again by 70% collision energy. The tertiary fragments (m/z 201, 213, 268, 283 and 350 – combined in the yellow line) all reach the maximum relative intensity of 100% at around 70% HCD collision energy.

4.3.5 Possible Degradation Pathways

Looking at the HCD plots, several pathways of degradation can be identified. These plots demonstrate clearly the difference between primary degradants and secondary and higher degradants. This gives information of the pathways by which the compound degrades, which could inform a further analysis of the photodegradants.

Working out how the compound degrades can also be assisted using density functional theory (DFT) geometry optimisation, which uses computational techniques to identify possible protonation sites.⁹³ This can in turn demonstrate the most likely bonds to break, and therefore the likely pathway(s) of degradation. This approach is time-consuming and beyond the scope of this one-year experimental research project.

However, a basic interpretation of the fragments was conducted and therefore likely degradation pathways can be identified.

4.3.5.1 Metronidazole

The structure of metronidazole is repeated here (Figure 4.27- originally found in Table 3.3), for ease of understanding the fragmentation patterns.

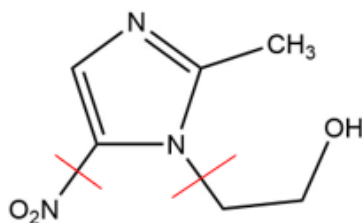


Figure 4.27: Structure of metronidazole. Red lines show suggested primary methods of fragmentation.

The CID fragments used for quantification and confirmation (Table 2.1) in the LC-SRM experiments were m/z 128 and 82, both of which were observed in the HCD experiment. These fragments can be attributed to the loss of the CH₂CH₂OH side chain (m/z 128 – a primary fragment), followed by the additional loss of NO₂ (m/z 82 – a secondary fragment).¹⁰⁴

m/z 111 (observed in the HCD experiment as a secondary fragment) can be attributed to the loss of CH₃ followed by NO₂.¹⁰⁴ This fragment had a much lower intensity than the CID fragments mentioned above when observed in the HCD experiment.

m/z 98 was observed in both the gas-phase photolysis experiment and the HCD experiment. This fragment can be attributed to fragmentation of m/z 128, *via* the loss of NO.

m/z 112 and 156 were two fragments that were only observed in gas-phase photolysis and did not derive from m/z 128. m/z 112 can be attributed to the loss of CH₂ and NO₂, and m/z 156 can be attributed to the loss of O.

These potential fragmentation patterns suggest that in solution metronidazole fragments to form m/z 128, which then further fragments into all other fragments.¹⁰⁴ This is seemingly different to

how metronidazole was observed to fragment in the gas phase, as although the fragment with m/z 128 is observed here, several fragments are produced that do not derive from it. The additional photofragments observed in the gas-phase may be reactive in solution and react with solvent (or other molecules of metronidazole) to form stable end products.

4.3.5.2 Penicillin v

The structure of penicillin v is repeated here (**Figure 4.28** - originally found in **Table 3.3**), for ease of understanding the fragmentation patterns.

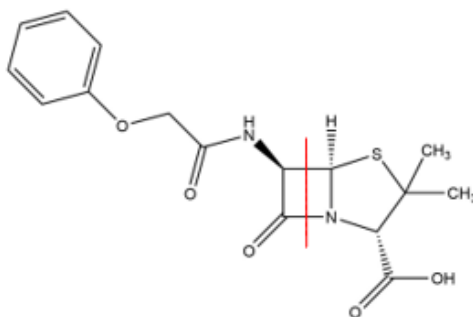


Figure 4.28: Structure of penicillin v. Red line shows the primary route of fragmentation.

The primary method of fragmentation for penicillin v appears to be *via* cleavage across the β -lactam ring (breaking the bonds between the (O=C) and N, and between (NH)C and C(H) – shown by the red line in **Figure 4.28**).¹⁰⁵ This produces several different fragments, due to the position of the charge-carrying proton. These fragments (m/z 192, 190 and 160) can be attributed to the loss of $C_6H_9NO_2S$, $C_6H_{11}NO_2S$ and $C_{10}H_9NO_3$ respectively. m/z 160 is only observed in the HCD experiment, m/z 190 is only observed in the photolysis and hydrolysis experiment, and m/z 192 is only observed in the gas-phase photolysis experiment.

Another fragment that was produced in both the HCD experiment and the gas-phase photolysis experiment had m/z 213. This can be attributed to the loss of both C_6H_5OH and CO_2 .

4.3.5.3 Oxytetracycline

The structure of oxytetracycline is repeated here (Figure 4.29 - originally found in Table 3.3), for ease of understanding the fragmentation patterns.

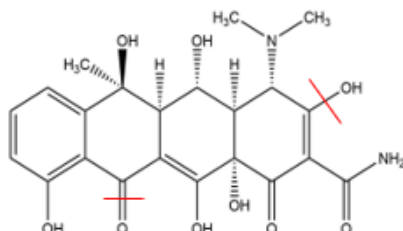


Figure 4.29: structure of oxytetracycline. Red lines show suggested primary routes of fragmentation.

The HCD fragmentation of protonated oxytetracycline in this experiment gave very similar results to another study conducted by Kamel et al in 2002.¹⁰⁶ This is good confirmation for many of the fragments spotted in this study. The CID fragments used for quantification and confirmation (Table 2.1) in the LC-SRM experiments were m/z 443 and 426, both of which were observed in the HCD experiment and the gas-phase photolysis experiment. These fragments can be attributed to the loss of H_2O (m/z 443), followed by OH (m/z 426).¹⁰⁶ Further fragments, such as m/z 408, 381, 365, 337, 226 and 154, can also be seen in the spectra reported by Kamel et al.¹⁰⁶

4.4 Conclusions

The main method of degradation for these three compounds appears to be photolysis, at least over a short time span of eight hours. Metronidazole appeared to be the compound least susceptible to photolysis, followed by penicillin v and then oxytetracycline (which is highly susceptible to photolysis). Oxytetracycline photofragmented into a very large number of detectable fragments (64), while metronidazole and penicillin v photofragmented into fewer (10 and 25, respectively) detectable fragments. However, a more in-depth analysis is required to fully gain an understanding of how these protonated compounds degrade in the gas phase.^{93,107}

It is worth noting that as no repeats were conducted for the solution-phase experiments (hydrolysis and photolysis; hydrolysis only) these promising results cannot be taken as final. Therefore, further experiments should be conducted to confirm these results.

Several degradants were identified for each of these compounds, including products of hydrolysis, solution phase photolysis and gas phase photolysis. Complete lists of fragments identified are not included as drawing up such complete lists needs much more time than was available, due to the unexpected and unprecedented complexity of the spectra.

Chapter 5 Conclusions and Further Work

5.1 Conclusions

The aims and objectives listed at the start of the thesis (section 1.1) are repeated here for convenience.

5.1.1 *Identify methods already used to detect antibiotics and to assess them regarding the 11 antibiotics targeted here (Chapter 2).*

From the literature, the primary technique used to analyse antibiotics in environmental samples was found to be LC-MS/MS (section 1.4.1). Commonly used mobile phases consisting of methanol, acetonitrile and water were examined to determine the most efficient chromatographic separations (section 2.3.3).

Assessing the antibiotics *via* the literature methods proved problematic, with many modifications being required. Ultimately, ten of the original 11 target antibiotics were able to be analysed (section 2.5), with colistin b being unable to be resolved in LC-MS. An alternative method, using MALDI as the source, was identified as a possible way to quantify colistin b in future studies (section 2.3.5).

5.1.2 *Develop and validate a LC-MS/MS method to detect and quantify the 11 antibiotics in two soil-derived samples: soil pore water and irrigation leachate (Chapter 2).*

Ten of the original 11 target antibiotics were able to be analysed. For these antibiotics, two different LC-MS/MS methods were used. These required two different columns, as well as two different mobile phases: the first, methanol with 0.1% formic acid and 0.1% aqueous formic acid with 0.1% ammonium formate using a C18 column, the second, acetonitrile with 0.1% formic acid and 0.1% aqueous formic acid using a T3 column (**Table 2.4**). The limits of detection were low enough that the antibiotics could be detected at the predicted no effect concentration (PNEC)

(section 2.4.2). This was significant as it allowed for the determination of a simple risk assessment to determine if concentrations exceeded those that would be required to select for antibiotic resistance in microbes.

5.1.3 Measure the levels of antibiotics in the pore water and soil leachates of barley rhizospheres, grown in a mesocosm, following irrigation with spiked wastewater (Chapter 3).

The LC-MS/MS methods identified as part of objective 2 were used to quantify the antibiotics in pore water and soil leachate samples (section 3.1.1). Only four of the ten antibiotics were detected in the soil pore water (metronidazole, trimethoprim, erythromycin and cefalexin – section 3.3.2) and five of the ten antibiotics were detected in the soil leachate samples (metronidazole, trimethoprim, erythromycin, clarithromycin and cefalexin – section 3.3.1). They were generally only detected in both the leachate and the pore water samples at the highest treatment levels (predicted concentrations, 10x and 100x). Carryover was an issue for trimethoprim, and so it is unknown how reliable the results for this antibiotic are (section 3.5). The concentrations in the leachate samples increased with increasing exposure, i.e. increased irrigation events (section 3.5.1.1). The opposite trend was observed in the pore water samples, excepting trimethoprim (section 3.5.1.2). The percentages of the antibiotics accounted for across the plant-soil system only accounted for a maximum of 12% of the administered antibiotic masses (**Table 3.7**). Therefore, a large proportion of the antibiotics have either degraded abiotically/biotically or have sorbed to the soil. A very small proportion might have been taken up into the plant.¹⁰⁸

5.1.4 Based on the results of objective 3, compounds susceptible to environmental degradation were examined further, using hydrolysis and photolysis experiments to identify degradants, with the use of non-targeted mass spectrometric analysis (Chapter 4).

The results from the hydrolysis and photolysis experiments (sections 4.2.1, 4.2.2 and 4.2.3) are summarised in **Table 5.1**.

Table 5.1: summary of the findings from the photolysis and hydrolysis experiments for each antibiotic studied.

Antibiotic	Hydrolysis in the dark	Hydrolysis with photolysis	Gas phase photolysis
Metronidazole	✘	✓	✓
Oxytetracycline	✘	✓	✓
Penicillin v	✘	✓	✓

This suggests that none of the compounds studied degrade extensively *via* hydrolysis within the time frame of the laboratory experiments (section 4.3.2). However, in the environment they would be exposed to water for a much longer period, and so these results cannot be used to deduce what would happen over a period of weeks/months in an aqueous environment.

However, all three compounds appeared to degrade *via* photolysis when in an aqueous environment (section 4.3.1), and so studying the degradants of these compounds and their effect on the environment should be a priority in future research.

Gas-phase photolysis resulted in very different results for each antibiotic (section 4.3.3).

Metronidazole photofragmented to produce 10 detectable fragments, penicillin v produced 25 detectable fragments and oxytetracycline produced 64 detectable fragments. However, other

small organic molecules produce far fewer photofragments than these antibiotics, and so further research is necessary to determine structure relationships that result in fragmentation.

5.2 *Future Work*

5.2.1 *Analysis and Quantification of the Soil Samples*

The soil samples in this project were not analysed to quantify the antibiotics. Given that there are is a large percentage of the applied antibiotics that have not yet been accounted for, the antibiotics that have sorbed to the soil will be vital to further understand how the antibiotics travel through the soil-plant system, and to complete the mass balance.

5.2.2 *Identification of Antimicrobial Degradants Using a Non-Targeted and Candidate Degradant Screening Approach*

Future work on this project will involve the analysis of the soil and pore water samples to see if any candidate degradants identified here are detectable. This will involve conducting untargeted scans of the samples, and candidate degradant screening to detect the degradants.

5.2.3 *Long Term Fate studies*

Another future study could involve examining at the long-term effects of photolysis and hydrolysis of these antibiotics. Some pharmaceuticals have degradants that are more toxic than the parent compounds.⁸⁹ It is currently unknown what affect the degradants of antibiotics will have on the environment, and so this would be very important to investigate further. These long-term fate studies could also include conducting DFT geometry optimisation of these antibiotics to help identify the degradant structures.

Appendix

Sample Names Breakdown:

T1/2/3: refers to sample collection time (T1 = after 1 irrigation; T2 = after 15 irrigations; T3 = after 28 irrigations)

M01-M30: refers to which mesocosm the sample was collected from

A/B/C/D/E: refers to which treatment (A = control; B = PEC×0.1; C = PEC; D = PEC×10; E = PEC×100)

Table A.1: pore water volumes extracted from the samples.

Sample	Soil (g)	Pore Water (g)
T1-M01B	18.64	1.34
T1-M02E	23.12	1.43
T1-M03A	22.88	1.66
T1-M04E	20.65	0.97
T1-M05B	21.69	1.78
T1-M06C	30.88	1.63
T1-M07D	25.5	2.25
T1-M08C	34.77	2.75
T1-M09B	17.94	1.4
T1-M10A	22	1.63
T1-M11E	13.45	1.14
T1-M12E	20.06	1.68
T1-M13A	23.05	2.37
T1-M14C	25.76	1.435

Sample	Soil (g)	Pore Water (g)
T1-M15C	11.23	1.7
T1-M16C	14.31	1.05
T1-M17D	24.63	2.16
T1-M18E	27.15	2.29
T1-M19D	24.9	1.72
T1-M20D	20.79	1.67
T1-M21B	23.75	2.45
T1-M22C	25.77	2.2
T1-M23E	27.07	2.07
T1-M24D	26.11	1.96
T1-M25B	25.05	2.06
T1-M26A	21.45	1.99
T1-M27A	26.42	0.78
T1-M28A	20.52	1.42
T1-M29B	13.76	1.11
T1-M30D	23.31	2.22
T2-M01B	21.17	1.1
T2-M02E	28.26	2.25
T2-M03A	30.86	1.92
T2-M04E	19.2	0.57
T2-M05B	22.55	1.24
T2-M06C	31.96	1.55
T2-M07D	24.67	1.39
T2-M08C	25.86	1.75

Sample	Soil (g)	Pore Water (g)
T2-M09B	24.95	1.55
T2-M10A	20.16	0.49
T2-M11E	21.13	0.42
T2-M12E	29.23	1.58
T2-M13A	26.45	1.85
T2-M14C	22.36	0.93
T2-M15C	28.43	1.51
T2-M16C	24.29	1.17
T2-M17D	24.56	1.44
T2-M18E	26.76	2.21
T2-M19D	21.23	0.7
T2-M20D	22.82	1.11
T2-M21B	26.3	1.31
T2-M22C	23.66	1.35
T2-M23E	19.64	0.69
T2-M24D	24.78	1.48
T2-M25B	25.14	1.48
T2-M26A	29.79	1.23
T2-M27A	26.87	1.31
T2-M28A	23.74	0.84
T2-M29B	23.34	1.56
T2-M30D	28.95	1.31
T3-M01B	30.14	1.51
T3-M02E	18.1	1.01

Sample	Soil (g)	Pore Water (g)
T3-M03A	26.31	1.2
T3-M04E	28.45	1.13
T3-M05B	20.74	0.82
T3-M06C	19.75	0.46
T3-M07D	23.55	0.87
T3-M08C	22.66	0.6
T3-M09B	22.82	1.05
T3-M10A	19.31	0.22
T3-M11E	22.08	0.9
T3-M12E	20.4	0.7
T3-M13A	26.9	1.11
T3-M14C	22.96	0.77
T3-M15C	17.64	0.52
T3-M16C	22.5	0.6
T3-M17D	22.44	1.08
T3-M18E	27.47	1.15
T3-M19D	25.45	1.14
T3-M20D	22.75	0.81
T3-M21B	20.51	0.74
T3-M22C	20.58	0.89
T3-M23E	16.86	0.48
T3-M24D	21.34	0.81
T3-M25B	25.31	0.97
T3-M26A	21.36	0.56

Sample	Soil (g)	Pore Water (g)
T3-M27A	25.07	0.77
T3-M28A	21.11	0.5
T3-M29B	28.58	1.57
T3-M30D	26.43	0.71

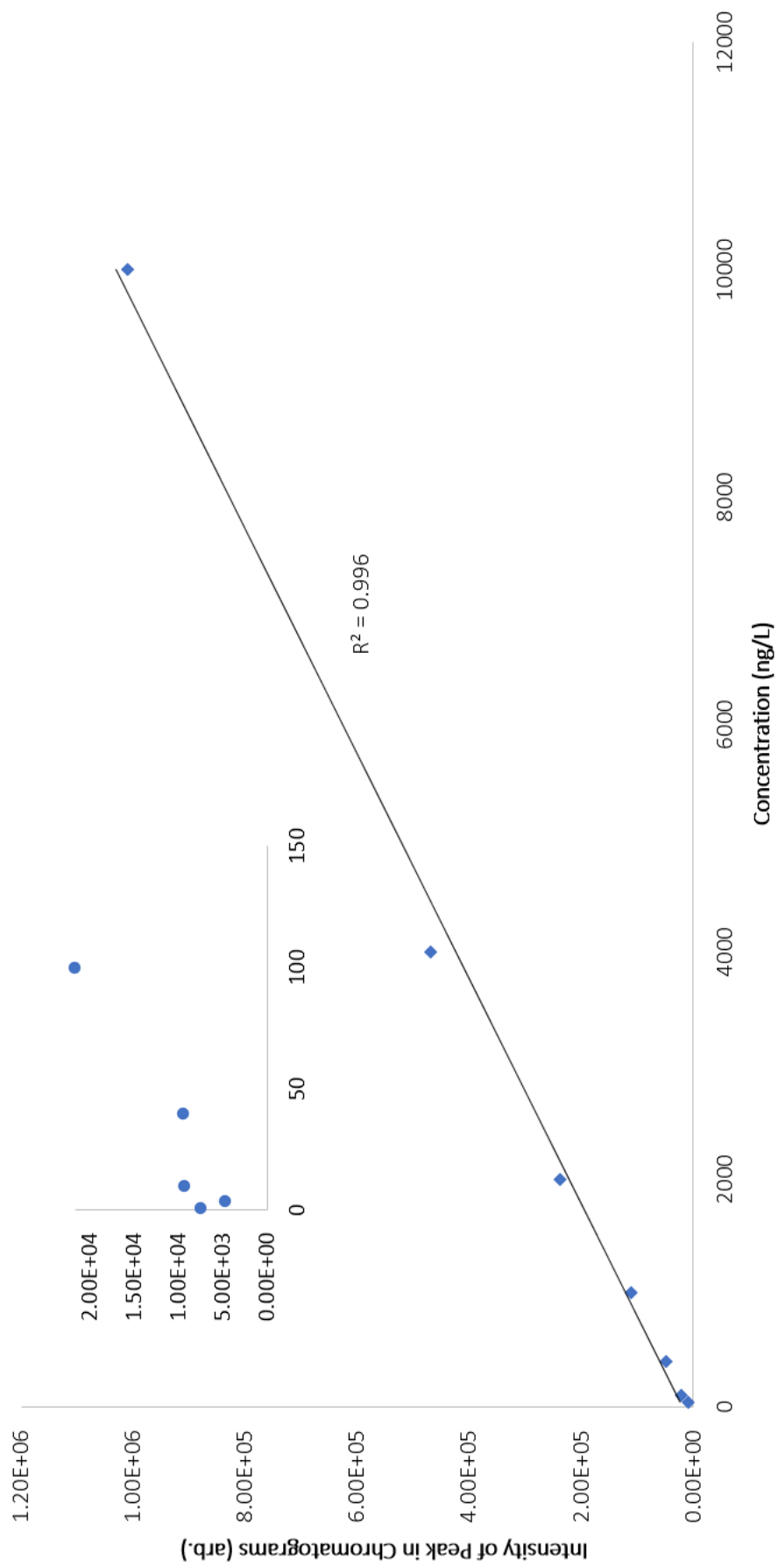


Figure A.1: calibration curve of trimethoprim. Zoomed in to show calibration points 1, 4, 10, 40 and 100.

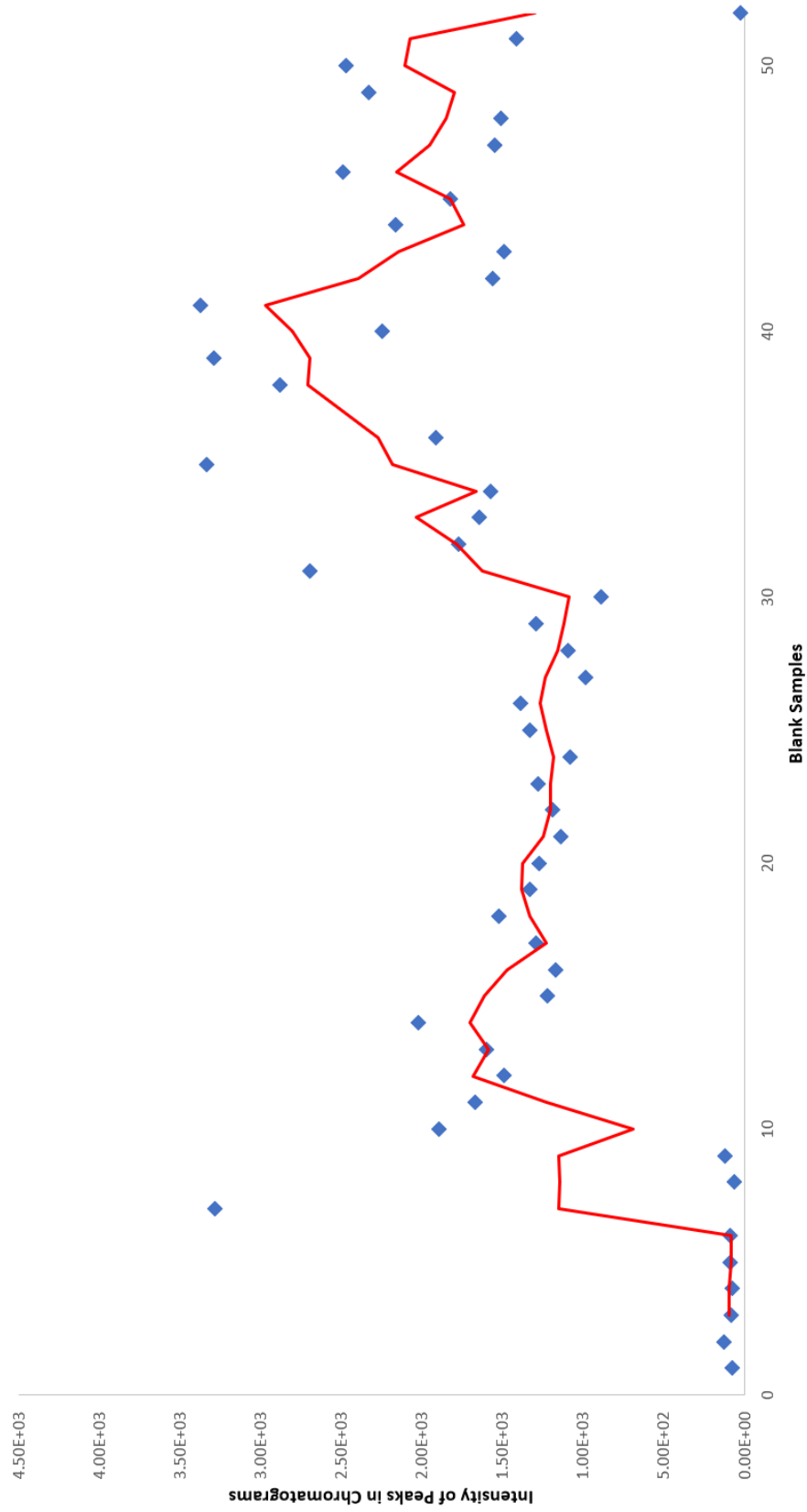


Figure A.2: the sample blanks numbered 1-52 throughout a sample analysis run on the LC-MS/MS. Demonstrating that the intensity of the trimethoprim peak in the blanks throughout the analysis run time did not exceed 4.00E3.

Table A.2: intensities of trimethoprim in the control samples. Demonstrating that the intensity does not exceed 4.50E+03.

Control Samples	Intensity (Arb.)
T1-M03A	2.98E+03
T1-M10A	2.02E+03
T1-M13A	2.31E+03
T1-M26A	2.77E+03
T1-M27A	2.20E+03
T1-M28A	2.52E+03
T2-M03A	1.93E+03
T2-M10A	2.53E+03
T2-M13A	2.31E+03
T2-M26A	2.35E+03
T2-M27A	3.52E+03
T2-M28A	4.02E+03
T3-M03A	2.29E+03
T3-M10A	1.87E+03
T3-M13A	2.84E+03
T3-M26A	1.47E+03
T3-M27A	8.87E+03
T3-M28A	2.89E+03

References

- 1 R. Laxminarayan, H. Goossens, E. Y. Klein, S. Gandra, S. Pant, S. A. Levin, E. M. Martinez and T. P. Van Boeckel, *Proc. Natl. Acad. Sci.*, 2018, **115**, E3463–E3470.
- 2 R. Hendricks and E. J. Pool, *J. Environ. Sci. Heal. - Part A Toxic/Hazardous Subst. Environ. Eng.*, 2012, **47**, 289–297.
- 3 T. Heberer, *Toxicol. Lett.*, 2002, **131**, 5–17.
- 4 M. Z. Alam, S. A. Muyibi and P. Jamal, *J. Environ. Sci. Heal. - Part A Toxic/Hazardous Subst. Environ. Eng.*, 2007, **42**, 1671–1679.
- 5 R. Hirsch, T. Ternes, K. Haberer and K. L. Kratz, *Sci. Total Environ.*, 1999, **225**, 109–118.
- 6 D. G. J. Larsson, *Ups. J. Med. Sci.*, 2014, 119, 108–112.
- 7 J. B. Sallach, S. L. Bartelt-Hunt, D. D. Snow, X. Li and L. Hodges, *Environ. Eng. Sci.*, 2018, **35**, 887–896.
- 8 R. L. Finley, P. Collignon, D. G. J. Larsson, S. A. Mcewen, X. Z. Li, W. H. Gaze, R. Reid-Smith, M. Timinouni, D. W. Graham and E. Topp, *Clin. Infect. Dis.*, 2013, 57, 704–710.
- 9 S. M. Prober, L. G. Barrett, M. Cardillo, N. Raisbeck-Brown, P. H. Thrall, R. Dinnage and A. K. Simonsen, *J. Ecol.*, 2018, 977–991.
- 10 P. Prashar, N. Kapoor and S. Sachdeva, *Rev. Environ. Sci. Biotechnol.*, 2014, **13**, 63–77.
- 11 K. Pollock, D. G. Barfield and R. Shields, *Plant Cell Rep.*, 1983, **2**, 36–39.
- 12 D. Shargil, Z. Gerstl, P. Fine, I. Nitsan and D. Kurtzman, *Sci. Total Environ.*, 2015, **505**, 357–366.
- 13 H. Li, J. B. Sallach, Y.-H. Chuang, C.-H. Liu, R. Hammerschmidt, W. Zhang and S. A. Boyd, *Environ. Int.*, 2019, **131**, 104976.

- 14 R. A. Brain, M. L. Hanson, K. R. Solomon and B. W. Brooks, *Rev. Environ. Contam. Toxicol.*, 2008, **192**, 67–115.
- 15 D. S. Aga, M. Lenczewski, D. Snow, J. Muurinen, J. B. Sallach and J. S. Wallace, *J. Environ. Qual.*, 2016, **45**, 407.
- 16 F. J. R. C. Coelho, A. L. Santos, J. Coimbra, A. Almeida, Â. Cunha, D. F. R. Cleary, R. Calado and N. C. M. Gomes, *Ecol. Evol.*, 2013, **3**, 1808–1818.
- 17 Flagyl (Metronidazole): Side Effects, Interactions, Warning, Dosage & Uses, <https://www.rxlist.com/flagyl-drug.htm#clinpharm>, (accessed 16 September 2019).
- 18 A. Jones and J. Janis, in *Essentials of Plastic Surgery*, 2015, pp. 101–102.
- 19 A. I. Hartstein, K. E. Patrick, S. R. Jones, M. J. Miller and R. E. Bryant, *Infection*, 2005, **8**, S588–S591.
- 20 P. Krzeminski, M. C. Tomei, P. Karaolia, A. Langenhoff, C. M. R. Almeida, E. Felis, F. Gritten, H. R. Andersen, T. Fernandes, C. M. Manaia, L. Rizzo and D. Fatta-Kassinou, *Sci. Total Environ.*, 2019, **648**, 1052–1081.
- 21 J. Li, R. W. Milne, R. L. Nation, J. D. Turnidge, T. C. Smeaton and K. Coulthard, *J. Antimicrob. Chemother.*, 2004, **53**, 837–840.
- 22 S. Wang and H. Wang, *Front. Environ. Sci. Eng.*, 2015, **9**, 565–574.
- 23 T. I. Technology, R. Council, C. S. Team and ITRC, *Appl. Note*, 2011, 272.
- 24 M. Topal and E. I. Arslan Topal, *Clean - Soil, Air, Water*, 2016, **44**, 444–450.
- 25 M. Gros, S. Rodríguez-Mozaz and D. Barceló, *J. Chromatogr. A*, 2013, **1292**, 173–188.
- 26 M. Pan and L. M. Chu, *Sci. Total Environ.*, 2016, **545–546**, 48–56.
- 27 J. B. Sallach, D. Snow, L. Hodges, X. Li and S. Bartelt-Hunt, *Environ. Toxicol. Chem.*, 2016, **35**,

- 889–897.
- 28 J. D. Cahill, E. T. Furlong, M. R. Burkhardt, D. Kolpin and L. G. Anderson, *J. Chromatogr. A*, 2004, **1041**, 171–180.
- 29 F. Blum, *Br. J. Hosp. Med.*, , DOI:10.12968/hmed.2014.75.Sup2.C18.
- 30 J. Betancourt and S. Gottlieb, Liquid Chromatography - Chemistry LibreTexts, [https://chem.libretexts.org/Bookshelves/Analytical_Chemistry/Supplemental_Modules_\(Analytical_Chemistry\)/Instrumental_Analysis/Chromatography/Liquid_Chromatography](https://chem.libretexts.org/Bookshelves/Analytical_Chemistry/Supplemental_Modules_(Analytical_Chemistry)/Instrumental_Analysis/Chromatography/Liquid_Chromatography), (accessed 7 December 2019).
- 31 2004, 173–193.
- 32 Chromatography - Efficiency and resolution | Britannica, <https://www.britannica.com/science/chromatography/Efficiency-and-resolution>, (accessed 14 April 2020).
- 33 F. Blum, *Br. J. Hosp. Med.*, , DOI:10.12968/hmed.2014.75.Sup2.C18.
- 34 Waters, UPLC - Ultra Performance Liquid Chromatography Beginner's Guide : Waters, https://www.waters.com/waters/en_GB/UPLC---Ultra-Performance-Liquid-Chromatography-Beginner%27s-Guide/nav.htm?cid=134803622&locale=en_GB, (accessed 14 April 2020).
- 35 L. Technical Publications, *TSQ Series II TSQ Endura and TSQ Quantiva Hardware Manual 80100-97014 Revision D*, 2017.
- 36 C. S. Ho, C. W. K. Lam, M. H. M. Chan, R. C. K. Cheung, L. K. Law, L. C. W. Lit, K. F. Ng, M. W. M. Suen and H. L. Tai, *Clin. Biochem. Rev.*, 2003, **24**, 3–12.
- 37 L. Technical Publications, *TSQ Series II TSQ Endura and TSQ Quantiva Getting Started Guide 80100-97228 Revision A*, 2017.

- 38 P. Kebarle and U. H. Verkcerk, *Mass Spectrom. Rev.*, 2009, **28**, 898–917.
- 39 V. R. Preedy and V. B. Patel, *General methods in biomarker research and their applications*, 2015, vol. 1–2.
- 40 J. Sreekumar, T. J. Hogan, S. Taylor, P. Turner and C. Knott, *J. Am. Soc. Mass Spectrom.*, 2010, **21**, 1364–1370.
- 41 A. Schreiber, *AB Sciex applikáció*, 2010, 6.
- 42 A. G. Marshall, C. L. Hendrickson and G. S. Jackson, *Mass Spectrom. Rev.*, 1998, **17**, 1–35.
- 43 Mass Spec Pro, Image Current Detection, <http://www.massspecpro.com/detectors/image-current-detection>, (accessed 4 December 2019).
- 44 Q. Hu, R. J. Noll, H. Li, A. Makarov, M. Hardman and R. G. Cooks, *J. Mass Spectrom.*, 2005, **40**, 430–443.
- 45 E. T. Furlong, C. J. Kanagy, L. K. Kanagy, L. J. Coffey and M. R. Burkhardt, *B. 5, Lab. Anal.*, 2014, 49.
- 46 Mobile phases, http://hplc.chem.shu.edu/NEW/HPLC_Book/Rev.-Phase/rp_mobph.html, (accessed 25 April 2020).
- 47 M. Summers, A. Kugler, W. Long and A. Mack, *Best Practices for Efficient Liquid Chromatography (LC) Operations Making the Most of Your LC System Making Good LC Methods Even Better Taking Advantage of LC Column Characteristics*, .
- 48 restek.com, *Pharm. Appl.*, 1–4.
- 49 S. E. Cheah, J. B. Bulitta, J. Li and R. L. Nation, *J. Pharm. Biomed. Anal.*, 2014, **92**, 177–182.
- 50 M. S. Díaz-Cruz and D. Barceló, *Anal. Bioanal. Chem.*, 2006, **386**, 973–985.
- 51 M. Zhao, X. J. Wu, Y. X. Fan, B. N. Guo and J. Zhang, *J. Pharm. Biomed. Anal.*, 2016, **124**,

- 303–308.
- 52 M. N. Uddin, S. Das, S. H. Khan, S. K. Shill, H. R. Bhuiyan and R. Karim, *J. Taibah Univ. Sci.*, 2016, **10**, 755–765.
- 53 Y. Dotsikas, C. K. Markopoulou, J. E. Koundourellis and Y. L. Loukas, *J. Sep. Sci.*, 2011, **34**, 37–45.
- 54 T3 Columns : Waters, https://www.waters.com/waters/en_US/T3-Columns/nav.htm?locale=en_US&cid=134914589, (accessed 24 September 2019).
- 55 Waters, 2015, 32.
- 56 J. Wilkinson, A. Boxall and D. Kolpin, *Appl. Sci.*, 2019, **9**, 1368.
- 57 linearity | The Chemical Statistician, <https://chemicalstatistician.wordpress.com/tag/linearity/>, (accessed 27 April 2020).
- 58 J. Bengtsson-Palme and D. G. G. J. Larsson, *Environ. Int.*, 2016, **86**, 140–149.
- 59 S. McCubbins, Accuracy vs. Precision in Chemistry: Definitions; Comparisons, <https://study.com/academy/lesson/accuracy-vs-precision-in-chemistry-definitions-comparisons.html>, (accessed 27 April 2020).
- 60 D. Hammond, in *Encyclopedia of Ocean Sciences: Second Edition*, Elsevier Inc., 2001, pp. 563–571.
- 61 M. Meredith-Williams, L. J. Carter, R. Fussell, D. Raffaelli, R. Ashauer and A. B. A. Boxall, in *Environmental Pollution*, Elsevier, 2012, vol. 165, pp. 250–258.
- 62 Mechanism of Action of Tetracyclines | Animations | PharmaXChange.info, <https://pharmaxchange.info/2011/05/mechanism-of-action-of-tetracyclines/>, (accessed 22 December 2019).

- 63 E. E. Burns, L. J. Carter, J. Snape, J. Thomas-Oates and A. B. A. Boxall, *J. Toxicol. Environ. Heal. - Part B Crit. Rev.*, 2018, 21, 115–141.
- 64 European Medicines Agency, *GUIDELINE ON THE ENVIRONMENTAL RISK ASSESSMENT OF MEDICINAL PRODUCTS FOR HUMAN USE DISCUSSION IN THE SAFETY WORKING PARTY*, 2006.
- 65 Amoxicillin - DrugBank, <https://www.drugbank.ca/drugs/DB01060>, (accessed 28 April 2020).
- 66 PubChem, Amoxicillin | C₁₆H₁₉N₃O₅S - PubChem, <https://pubchem.ncbi.nlm.nih.gov/compound/Amoxicillin#section=Optical-Rotation>, (accessed 28 April 2020).
- 67 Cefalexin hydrochloride - DrugBank, <https://www.drugbank.ca/salts/DBSALT001473>, (accessed 28 April 2020).
- 68 U. E. Osonwa, J. I. Ugochukwu, E. E. Ajaegbu, K. I. Chukwu, R. B. Azevedo and C. O. Esimone, *Bull. Fac. Pharmacy, Cairo Univ.*, 2017, 55, 233–237.
- 69 Clarithromycin - DrugBank, <https://www.drugbank.ca/drugs/DB01211>, (accessed 28 April 2020).
- 70 Erythromycin - DrugBank, <https://www.drugbank.ca/drugs/DB00199>, (accessed 28 April 2020).
- 71 Metronidazole - DrugBank, <https://www.drugbank.ca/drugs/DB00916>, (accessed 28 April 2020).
- 72 Oxytetracycline | C₂₂H₂₄N₂O₉ - PubChem, <https://pubchem.ncbi.nlm.nih.gov/compound/Oxytetracycline>, (accessed 28 April 2020).
- 73 Phenoxymethylpenicillin - DrugBank, <https://www.drugbank.ca/drugs/DB00417>, (accessed 28 April 2020).

- 74 Tetracycline - DrugBank, <https://www.drugbank.ca/drugs/DB00759>, (accessed 28 April 2020).
- 75 Trimethoprim - DrugBank, <https://www.drugbank.ca/drugs/DB00440>, (accessed 28 April 2020).
- 76 N. Genç, E. C. Dogan and M. Yurtsever, *Water Sci. Technol.*, 2013, **68**, 848–855.
- 77 W. Kong, C. Li, J. M. Dolhi, S. Li, J. He and M. Qiao, *Chemosphere*, 2012, **87**, 542–548.
- 78 L. Duan, L. Li, Z. Xu and W. Chen, *Environ. Sci. Process. Impacts*, 2014, **16**, 1462–1468.
- 79 F. J. Peng, G. G. Ying, Y. S. Liu, H. C. Su and L. Y. He, *Sci. Total Environ.*, 2015, 506–507, 58–65.
- 80 W. Zhou, S. Yang and P. G. Wang, *Bioanalysis*, 2017, 9, 1839–1844.
- 81 L. J. Carter, C. D. Garman, J. Ryan, A. Dowle, E. Bergström, J. Thomas-Oates and A. B. A. Boxall, *Environ. Sci. Technol.*, 2014, **48**, 5955–5963.
- 82 E. E. Burns, .
- 83 G. J. Palm, T. Lederer, P. Orth, W. Saenger, M. Takahashi, W. Hillen and W. Hinrichs, *J. Biol. Inorg. Chem.*, 2008, **13**, 1097–1110.
- 84 S. Jiao, S. Zheng, D. Yin, L. Wang and L. Chen, *Chemosphere*, 2008, **73**, 377–382.
- 85 D. G. Hillis, J. Fletcher, K. R. Solomon and P. K. Sibley, *Arch. Environ. Contam. Toxicol.*, 2011, **60**, 220–232.
- 86 W. Schmidt and C. H. Redshaw, *Ecotoxicol. Environ. Saf.*, 2015, **112**, 212–222.
- 87 M. Cycoń, A. Mrozik and Z. Piotrowska-Seget, *Front. Microbiol.*, , DOI:10.3389/fmicb.2019.00338.
- 88 J. C. Mitra, K. Kota and S. K. Sar, .

- 89 S. R. D. O. Melo, M. Homem-De-Mello, D. Silveira and L. A. Simeoni, *PDA J. Pharm. Sci. Technol.*, 2014, **68**, 221–238.
- 90 T. E. Doll and F. H. Frimmel, *Chemosphere*, 2003, **52**, 1757–1769.
- 91 UV Photolysis and UV AOP, <http://www.trusselltech.com/technologies/advanced-oxidation/uv-photolysis-and-uv-aop>, (accessed 8 December 2019).
- 92 Libretexts, What Causes Molecules to Absorb UV and Visible Light, [https://chem.libretexts.org/Bookshelves/Physical_and_Theoretical_Chemistry_Textbook_Maps/Supplemental_Modules_\(Physical_and_Theoretical_Chemistry\)/Spectroscopy/Electronic_Spectroscopy/Electronic_Spectroscopy_Basics/What_Causes_Molecules_to_Absorb_UV_and_V](https://chem.libretexts.org/Bookshelves/Physical_and_Theoretical_Chemistry_Textbook_Maps/Supplemental_Modules_(Physical_and_Theoretical_Chemistry)/Spectroscopy/Electronic_Spectroscopy/Electronic_Spectroscopy_Basics/What_Causes_Molecules_to_Absorb_UV_and_V), (accessed 8 December 2019).
- 93 N. G. K. Wong, J. A. Berenbeim, M. Hawkridge, E. Matthews and C. E. H. Dessent, *Phys. Chem. Chem. Phys.*, , DOI:10.1039/c8cp06794e.
- 94 S. Comber, M. Gardner, P. Sörme, D. Leverett and B. Ellor, *Sci. Total Environ.*, 2018, **613–614**, 538–547.
- 95 P. Sacha, P. Wieczorek, T. Hauschild, M. Zórawski, D. Olszańska and E. Tryniszewska, *Folia Histochem. Cytobiol.*, 2008, **46**, 137–142.
- 96 Elufisan T. O, *African J. Microbiol. Res.*, , DOI:10.5897/ajmr11.436.
- 97 L. L. Jessome and D. A. Volmer, *Ion Suppression: A Major Concern in Mass Spectrometry*, 2006, vol. 24.
- 98 True Variance – APA Dictionary of Psychology, <https://dictionary.apa.org/true-variance>, (accessed 20 April 2020).
- 99 A. Amaro-Ortiz, B. Yan and J. A. D’Orazio, *Molecules*, 2014, **19**, 6202–6219.
- 100 M. R. El-Ghobashy and N. F. Abo-Talib, *J. Adv. Res.*, 2010, **1**, 323–329.

- 101 C. I. Oprea, L. C. Petcu and M. A. Gîrțu, *2015 E-Health Bioeng. Conf. EHB 2015*, 2016, 1–4.
- 102 N. Marina, D. Elizabeta and S. Goran, .
- 103 J. D. S. F. Da Silva, D. L. Malo, G. A. Bataglion, M. N. Eberlin, C. M. Ronconi, S. Alves and G. F. De Sá, *PLoS One*, , DOI:10.1371/journal.pone.0128436.
- 104 L. Tong, S. Pérez, C. Gonçalves, F. Alpendurada, Y. Wang and D. Barceló, *Anal. Bioanal. Chem.*, 2011, **399**, 421–428.
- 105 S. Suwanrumpha, D. A. Flory, R. B. Freas and M. L. Vestal, *Biol. Mass Spectrom.*, 1988, **16**, 381–386.
- 106 A. M. Kamel, H. G. Fouda, P. R. Brown and B. Munson, *J. Am. Soc. Mass Spectrom.*, 2002, **13**, 543–557.
- 107 N. G. K. Wong, J. A. Berenbeim and C. E. H. Dessent, *ChemPhotoChem*, 2019, 1–8.
- 108 S. L. Bartelt-Hunt, D. D. Snow, J. B. Sallach, X. Li and L. Hodges, *Environ. Eng. Sci.*, 2018, **35**, 887–896.